POLITECNICO
MILANO 1863

School of Industrial and Information Engineering
Department of Aerospace Science and Technology
Master of Science in Space Engineering

Numerically efficient methods for impulsive and low-thrust collision avoidance manoeuvre design

Candidate:
Maria Francesca PALERMO
ID: 920959

Supervisor:
Prof. Pierluigi DI LIZIA

Co-Advisors:
Prof. Roberto ARMELLIN
PhD Candidate Andrea DE VITTORI

Academic Year 2019 – 2020

To my father,
Nico

Abstract

Critical conjunctions in space are occurring at increasing frequency due to the fast-growing and intensive use of space. Evidently, mitigating the consequent risk of collisions is of utmost importance for a sustainable use of space. Prospectively, this scenario is not expected to settle down in the near future, due to the recent plans of large constellations deployment and to the trend of satellites miniaturisation. For the above reasons, Collision Avoidance Manoeuvre (CAM) planning and optimisation are becoming routine tasks of fundamental importance for a mission's success. The number of CAMs to be executed is expected to scale up in the future. Consequently, it is paramount to promote the development of numerically efficient methods for CAM design, possibly reaching on-board implementability. A further challenge is posed in the field by the recent technological advances in space propulsion. An increasing number of satellites are equipped with electric thrusters to control their orbit through continuous low-thrust manoeuvres.

Within this framework, this thesis investigates the problems of designing both impulsive and low-thrust optimal collision avoidance manoeuvres, with the aim of developing robust and numerically efficient algorithms. To this purpose, the conjunction dynamics is presented in Cartesian reference frame and then projected onto the B-plane, centred at the secondary object. The optimal manoeuvres are constrained in terms of Probability of Collision (PoC), Squared Mahalanobis

Distance (SMD) and Miss Distance (MD) at the time of closest approach. Fully analytical methods have been developed in the perspective of finding fast, reliable, and iteration-free approaches to manoeuvre design.
In order to match operational requirements, starting from the analytical solution of the unbounded control problem for low-thrust CAMs, a bang-bang structure is achieved by applying a smoothing approach. Moreover, the investigation of purely tangential manoeuvres is included.
The influence of environmental perturbations is also addressed and statistical analyses using a large dataset of collisions are performed. Overall, the main assumptions of the proposed methods are constant and uncorrelated covariances, short-term encounters and spherical object approximation. The different approaches are compared in terms of efficiency and robustness in a simulated scenario accounting for orbital perturbations, which are shown to be negligible.

Sommario

Le congiunzioni critiche tra satelliti in orbita si verificano con frequenza sempre maggiore, a causa della rapida crescita e dell'intensività dell'uso dello spazio. Mitigare il conseguente rischio di collisioni assume chiaramente la massima importanza per un uso sostenibile dello spazio. Guardando al prossimo futuro, non ci si aspetta che questo scenario si stabilizzi, a causa dei recenti progetti di grandi costellazioni e della tendenza alla miniaturizzazione dei satelliti. Per queste ragioni, la pianificazione e l'ottimizzazione delle manovre per evitare le collisioni (CAM) sta diventando un compito di routine di fondamentale importanza per il successo di una missione. Si prevede che il numero di CAM da eseguire aumenterà in futuro. Di conseguenza, è fondamentale promuovere lo sviluppo di metodi numericamente efficienti per la progettazione delle manovre, possibilmente raggiungendo l'implementabilità a bordo. Un'ulteriore sfida nel campo è posta dai recenti progressi tecnologici nella propulsione spaziale. Un numero crescente di satelliti sono dotati di motori elettrici che permettono di controllare la loro orbita attraverso manovre continue a bassa spinta.

Nel contesto presentato, questa tesi indaga il problema della progettazione di manovre ottime sia impulsive sia a spinta continua, con l'obiettivo di sviluppare algoritmi robusti e numericamente efficienti. A questo scopo, la dinamica di congiunzione dei due oggetti è presentata in un sistema di riferimento Cartesiano e poi

proiettata sul B-plane, centrato sull'oggetto secondario. La manovre ottime sono vincolate in termini di probabilità di collisione (PoC), di distanza di Mahalanobis al quadrato (SMD) o di distanza Cartesiana (MD) al momento dell'incontro più vicino tra i due oggetti. Sono stati sviluppati metodi completamente analitici nella prospettiva di trovare approcci veloci, affidabili e privi di iterazioni per la progettazione delle manovre.
Al fine di soddisfare i requisiti operativi, partendo dalla soluzione analitica del problema di controllo senza restrizioni per manovre a spinta continua, è stato inoltre ottenuto un profilo di accelerazione con struttura bang-bang applicando un approccio di smoothing. In aggiunta sono state studiate soluzioni ottime per manovre puramente tangenziali.
L'influenza delle perturbazioni orbitali è stata considerata e sono state effettuate analisi statistiche utilizzando un ampio dataset di collisioni. Nel complesso, le principali ipotesi dei metodi proposti sono: covarianze costanti e non correlate, incontri di breve durata tra i corpi orbitanti e approssimazione sferica degli oggetti. I diversi approcci sono stati confrontati in termini di efficienza e robustezza in uno scenario simulato considerando le perturbazioni ambientali, verificandone quindi la trascurabilità.

Acknowledgements

I wish to express my deepest gratitude to my supervisor Professor Pierluigi Di Lizia for the constant support, encouragement and also enthusiasm for the work I carried out. Thanks to my co-advisors Professor Roberto Armellin and Andrea De Vittori for their precious help, trust and interest. I would also like to thank my friend Marco Felice Montaruli, PhD candidate: I am glad I got a chance, albeit a short one, during my thesis to work with you and learn a lot from you.

I am extremely grateful to my lovely brothers Anna Fiore and Federico, and my mother Pina: notwithstanding the challenges of daily life you have been the best company I could have wished for, even during lockdown periods. I would particularly thank my father Nico, to whom this thesis is dedicated, for teaching me a million things, but especially for his "Whenever you get in crisis with your thesis, remember I love you". Thanks to my grandparents, auntie Mary, uncle Peppe, my cousins Teo, Eli, Luci and little Delia, for the gift of the greatest joy that can exist, even in these pandemic times. Special thanks to my friend Max for being a hard study partner in these 5 years, for his unconditional help and friendship. Thanks Mitch, for a lot of things, but of all of them for letting me discover a whole new way to live university. Thank you Cate, the brightest star in Bovisa. Thanks to the *Space Team*: my amazing friends Bak, Jack, Gio, Simo,

Chiappo. Thanks Fede and Mati: we grew up together and we are still doing it. Thanks to my *Carbonara Family*, the best people I could ever meet during my Erasmus. Thanks to all my friends, in particular Civa, Marco, Tommi, Guaglio, Marta, Luca, Michi, Giulia, Teo. Thank you Maggio, don Michele and don Sergio for being guides, as well as friends, over these years. Special mention to the *Group of 2003*: our journey together has been one of the most significant experiences of these years. Thank you Cinzia, Andrea, Giancarlo and Edoardo, for your love and the ever-present enthusiasm for every little goal I achieve.
Thanks to the person who most of all every day believes in me and my dreams, even more than I do: Riccardo.

Table of Contents

List of Figures

List of Tables

List of Acronyms

BC Boundary Condition 48, 63, 72, 73

BP B-plane XXVI, 9, 45, 46, 52, 55, 66, 68, 73, 99, 103

CA Closest Approach 16, 57, 58, 84

CAM Collision Avoidance Manoeuvre V, VII, XVI, XIX, 1, 6–9, 17, 21, 22, 34, 45, 46, 82, 98, 103, 106, 107

CCSDS Consultative Committee for Space Data Systems 6

CDM Conjunction Data Message XXVII, 6, 8, 9, 36, 46, 89

CSM Conjunction Summary Message 6

CT Computational Time 102

ECI Earth-Centered Inertial XXVI, 9, 37, 45, 46, 52, 62, 68, 103

EOP Energy-Optimal control Problem 8, 9, 28, 48, 54, 62, 63, 67, 68, 73, 74, 99, 103, 106

ESA European Space Agency 6, 7

FOP Fuel-Optimal control Problem 8

GEO Geostationary Earth Orbit 2

HST Hubble Space Telescope XV, 4

IC Initial Condition 22, 28, 47–49, 62, 64

IVP Initial Value Problem 48, 49, 54, 55, 64, 66, 68

JSpOC Joint Space Operations Center 6

LEO Low Earth Orbit 2, 7, 26, 89, 99, 106

LVLH Local Vertical Local Horizontal 17, 30, 34, 38, 57, 77, 82, 84, 90

MD Miss Distance VI, VIII, XVI, XIX, 6, 9, 29, 30, 33, 34, 36, 41–43, 46, 47, 54, 62, 67, 102, 103, 105

NEO Near-Earth Object 6

OCP Optimal Control Problem 26, 103

PDF Probability density function 23

PoC Probability of Collision V, VIII, XVI, XIX, XXVII, 6, 8, 9, 23, 24, 29, 30, 34, 36, 40–43, 46, 47, 54, 57, 62, 67, 83, 86, 102, 103, 105–107

r.f. reference frame XV–XVIII, 12, 13, 17, 34, 38, 40, 43, 46, 55–57, 61, 62, 65, 66, 68–70, 82–84, 86, 90, 99, 100

SDO Space Debris Office 7

SMD Squared Mahalanobis Distance V, VI, VIII, 9, 24, 29, 30, 32, 34, 36, 40, 46, 47, 54, 62, 63, 67, 83, 102, 105

SSA Space Situation Awareness 6

SST Space Surveillance and Tracking 6

STM State Transition Matrix 28, 49, 54, 64, 67, 81–83

TCA Time of Closest Approach XVI, XVII, 6, 14, 17, 21, 22, 39, 41, 46, 52, 55, 56, 58, 61, 68, 73, 77, 83, 84, 86, 94

TLE Two-Line Element set 6

TPBVP Two-Point Boundary Value Problem 8, 27, 48, 63, 64, 73, 75, 77

USSTRATCOM US Strategic Command 6

Nomenclature

Mathematical legend

$\mathbf{A}$	Matrix
$\mathbf{a}$	Vector
a	Scalar

Physical quantities

$\boldsymbol{\lambda}$	Costate vector	[–]
$\Delta\mathbf{v}$	Impulse vector	[m/s]
μ	Earth's gravitational constant	[km^3/s^2]
θ	True anomaly	[deg]
$\mathbf{\Phi}$	State Transition Matrix	[–]
$\mathbf{a}_c$	Control acceleration vector	[m/s^2]

$\mathbf{b}$	Position vector in BP coordinates	[km]
$\mathbf{C}$	Combined covariance matrix	[km^2]
$\mathbf{r}$	Position vector in ECI coordinates	[km]
$\mathbf{R}_b$	Rotation matrix between ECI frame and B-plane	[−]
$\mathbf{v}$	Velocity vector	[km/s]
d	Miss distance	[km]
g_0	Earth's standard gravity acceleration	[km/s^2]
I_{sp}	Specific impulse	[s]
m	Mass	[kg]
t	Time	[s]
PoC	Probability of collision	[−]
SMD	Squared Mahalanobis distance	[km^2]

Subscripts/superscripts

0	Initial manoeuvring point
f	Final manoeuvring point
p	Primary object
s	Secondary object

Built-in functions

control_propagator$([\mathbf{x}_0, \boldsymbol{\lambda}_0], tspan)$ It gives the final state of a satellite, propagating the initial state $\mathbf{x}_0$ and costate $\boldsymbol{\lambda}_0$ for the time interval $tspan$ with optimal controlled dynamics.

keplerian_propagator($\mathbf{x}_0, tspan$) It gives the final state of a satellite, propagating the initial state $\mathbf{x}_0$ for the time interval *tspan* with Keplerian dynamics.

min($\mathbf{A}$) It gives the minimum value in a matrix $\mathbf{A}$. It works with input arrays too.

percentile($\mathbf{A}, val$) It gives the value associated with the percentile *val* of a matrix $\mathbf{A}$.

poc2smd(PoC, CDM) It gives the Squared Mahalanobis distance between two objects given their PoC and the CDM.

poc_chan($\Delta\mathbf{r}$, CDM) It computes the collision probability between two objects with relative distance $\Delta\mathbf{r}$, given the CDM, using Chan's method.

size($\mathbf{A}, dim$) It gives as an output the size of the matrix $\mathbf{A}$ over the dimension *dim*. It works also with input 1D arrays and in this case *dim* is not mandatory.

squared_mahalanobis_distance($\Delta\mathbf{r}$, CDM) It computes the squared Mahalanobis distance between two objects with relative distance $\Delta\mathbf{r}$, given the CDM.

CHAPTER 1

Introduction

The motivation and the purpose of this dissertation are stated in this first introductory chapter, starting from the presentation of the problems and the limitations of the field of interest. Then, a brief description of the state of the art of collision avoidance manoeuvres is provided. Finally, an outline of the thesis is presented.

1.1 Space debris and collision avoidance manoeuvres

The ultimate purpose of providing efficient methods for CAM, which is the problem tackled in this dissertation, is twofold: on the one hand to avoid damage to satellites, and on the other to prevent the formation of space debris.
Space debris are all artificial objects orbiting the Earth, including fragments resulting from previous collisions or parts of multistage launchers, other than a

space vehicle that is active or liable to be used in another way, being in orbit. Half of them is represented by entire objects (e.g. inactive satellites or launchers upper stages), while the other half is composed by fragments of various shape and size (resulting from explosions or collisions) or from objects lost during previous missions (coverage, strap, etc.) [Mon19].

Figure 1.1: Distribution of space debris greater than 1 mm in orbit around Earth. Source: [ESAc].

Figure 1.1 is a computer-generated image representing space debris as could be seen from high Earth orbit. The two main debris fields are the ring of objects in Geostationary Earth Orbit (GEO), at 36000 km of altitude, and the cloud of objects in Low Earth Orbit (LEO), between 400 and 2000 km of altitude.
The number of debris objects estimated by statistical models to be in orbit is reported:

- 34,000 objects greater than 10 cm;
- 900,000 objects from greater than 1 cm to 10 cm;
- 128 million objects from greater than 1 mm to 1 cm.

The total mass of all space objects in Earth orbit is more than 9,200 tonnes and artificial pollution is now greater than the natural one due to meteorites. These numbers are even more alarming considering that the total number of rocket launches since the start of the space age in 1957 is just 6020 and given the large

number of launches planned for the next period ([ESAc], information last updated on January 8, 2021).

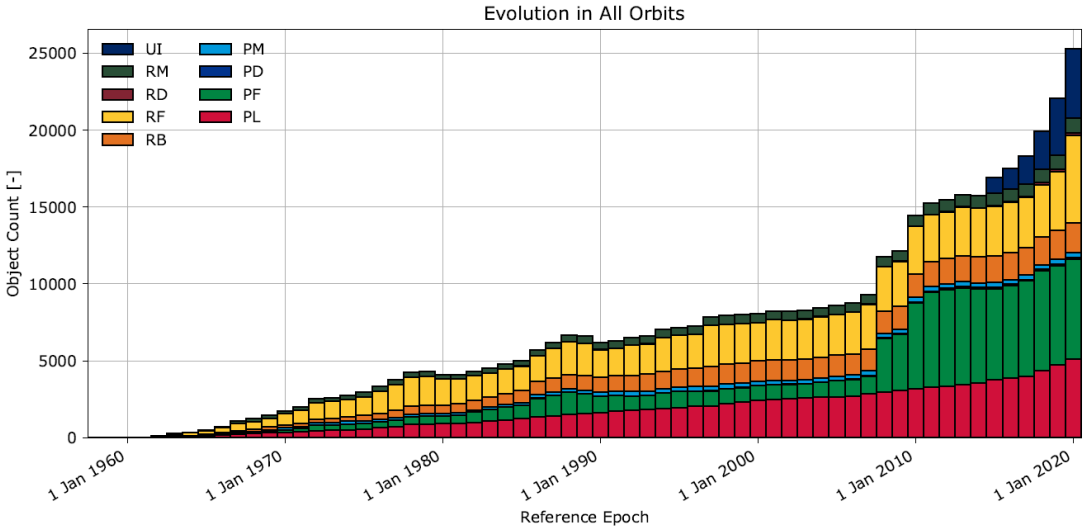

Figure 1.2: Evolution of number of objects in geocentric orbit by object class. Source: [ESA20].

Table 1.1: Object Classifications.

Type	Description
PL	Payload
PF	Payload Fragmentation Debris
PD	Payload Debris
PM	Payload Mission related Object
RB	Rocket Body
RF	Rocket Fragmentation Debris
RD	Rocket Debris
RM	Rocket Mission Related Object
UI	Unidentified

As it can be seen from Figure 1.2 (legend in Table 1.1), the number of debris objects has been steadily increasing since the beginning of the space age. This is further fuelled by a large number of in-orbit break-ups of spacecraft and rocket stages. The total area that space debris takes up is important as it is directly

related to how many collisions we expect in the future. As things stand, collisions between debris and working satellites are predicted to overtake explosions as the dominant source of space junk.
Debris-creating events have become more common: on average over the last two decades, 12 accidental fragmentations have occurred in space every year, and this trend is unfortunately increasing. Fragmentation events are responsible for this major issue and are created due to collisions, explosions, electrical problems and even just the detachment of objects due to the harsh conditions in space.
The increasing number of resident space objects in orbit naturally leads to a collision risk among satellites and/or debris. In addition to creating an enormous amount of new fragments and incrementing the orbital pollution, such an impact would damage the satellite, considering that space debris can reach speeds of 25,000 km/h, almost seven times faster than a bullet [NAS]. Figure 1.3 illustrates the damage to the solar panels of the Hubble Space Telescope (HST).

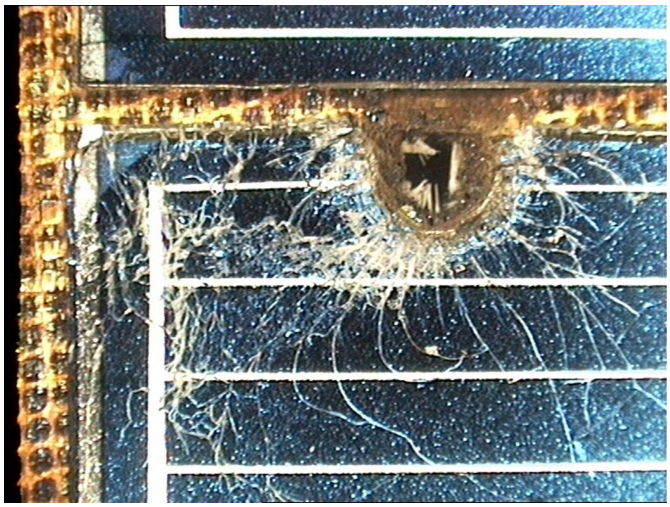

Figure 1.3: Front view of penetration of HST solar array. Source: [ESAa].

The estimated total number of break-ups, explosions, collisions, or anomalous events resulting in fragmentation tracked by Space Surveillance Networks since the launch of the first Sputnik in 1957 is more than 560 [ESAc]. Figure 1.4 reveals the causes of fragmentations events: although collisions are not the primary cause, when they occur they do cause a huge amount of debris. Figure 1.5 depicts that a large amount of junk was produced between 2005 and 2010; during this period a serious collision happened between the Iridium 33 communications satellite and

the derelict Russian Kosmos 2251 spacecraft, which resulted in the destruction of both satellites.

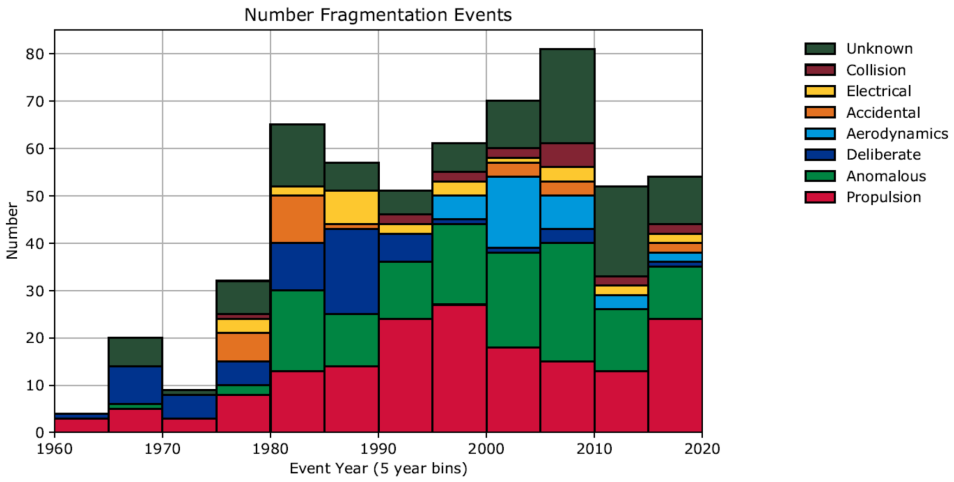

Figure 1.4: Historical trend of fragmentation events per event cause. Source: [ESA20].

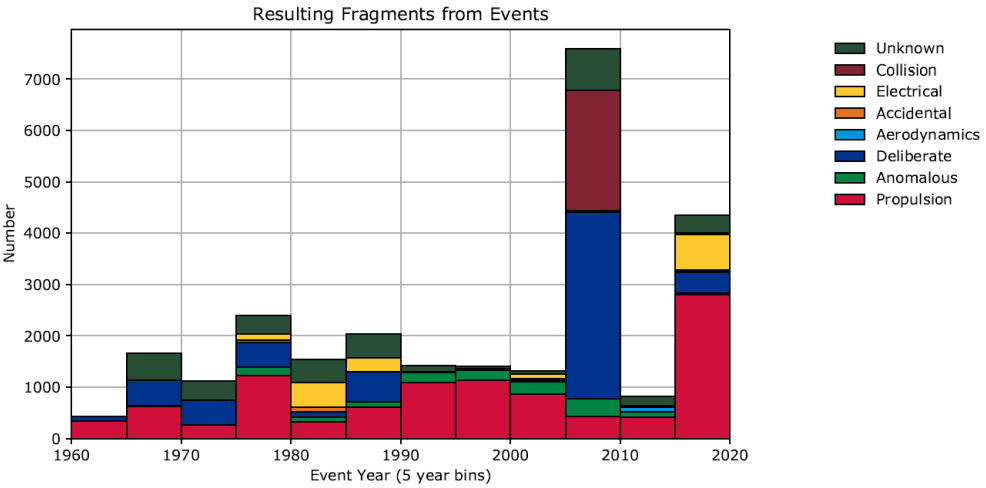

Figure 1.5: Historical trend of numbers of fragments produced by fragmentation events. Source: [ESA20].

Existing international guidelines and standards clarify how a sustainable use of space can be achieved:

- Design rockets and spacecraft to minimise the amount of shedding, material becoming detached during launch and operation, due to the harsh conditions of space.

- Prevent explosions by releasing stored energy, "passivating" spacecraft once at the end of their lives.
- Design end-of-life disposal of satellites, moving them out of the way of working satellites.
- Prevent in-space impacts through careful choice of orbits and by performing Collision Avoidance Manoeuvres.

This thesis focuses on the last measure, i.e., collision avoidance manoeuvre design.

1.2 State of the art

A collision avoidance manoeuvre is performed when, at the Time of Closest Approach (TCA), a threshold on the miss distance (MD), or on the collision probability (PoC), is exceeded.
Since 2009, Conjunction Messages have been sent by Joint Space Operations Center (JSpOC) to all spacecraft owners and operators, concerning approximately 15000 objects listed in the Two-Line Element set (TLE) provided by US Strategic Command (USSTRATCOM).
The information provided by the JSpOC consisted of a Conjunction Assessment Report that contains information about a conjunction between a primary satellite and another satellite or space object; it includes also the TCA, the miss distance, relative position and velocity, observation statistics, the satellite covariance matrices and the time of last acceptable observation. The standard format Conjunction Summary Message (CSM)/Conjunction Data Message (CDM) is used for messages being prepared by the Consultative Committee for Space Data Systems (CCSDS). Detailed information about CDM can be found in [Spa13].

ESA has implemented the Space Situation Awareness (SSA) programme, which aims to give Europe the necessary independence to acquire knowledge about the situation in space. Indeed, Europe is currently dependent on non-European information sources for its ability to monitor satellite sources of danger such as natural phenomena, Near-Earth Object (NEO) and space debris. Providing independent data and information, the SSA programme also enhances the reliability and availability of space. The SSA programme focuses on Space Weather, NEOs, and Space Surveillance and Tracking (SST). An overview of the programme can be found in [Flo17]. SST refers to the capacity to detect, catalogue and predict the movements of space objects orbiting the Earth. The European Union established

in 2014 the Space Surveillance and Tracking Support Framework, also known as the EU SST, with the Decision 541/2014/EU of the European Parliament and the Council (SST Decision) [Pel20].

For a typical satellite in LEO, hundreds of alerts are issued every week. For most, the risk of collision decreases as the week goes by and more orbital information is gathered, but for some it is deemed high enough that further action is required. As more satellites are launched into orbit, current "manual" methods for avoiding in-space collisions, and the creation of debris, will not be enough.
Nowadays, CAMs are planned on-ground, with the support of specific tools. If the pre-defined threshold on the probability or the miss distance is exceeded, a manoeuvre is designed by mission planners. The Space Debris Office (SDO) is the department of the European Space Agency (ESA) in charge of all the activities concerning space debris; a complete description of the SDO current collision avoidance service can be found in [Mer17].

From a rigorous standpoint, a collision avoidance manoeuvre is said to be optimal when it reduces the collision probability of a satellite with one, or more, space objects to a prescribed threshold while minimising a cost quantity.
Most research deals with optimising impulsive manoeuvres. In order to provide a fast and efficient numerical scheme to plan last-minute and out of plane manoeuvres, Bombardelli et al. in [Bom15], [Bom14a] and [Bom14b] studied closed-form analytic expressions and presented an efficient numerical scheme to solve the optimisation problem in its most general form. In [Bom14a] and [Bom14b], a formulation of the relative dynamics model, valid for a generic collision geometry and arbitrary eccentricity, is employed as a base for collision miss distance maximisation between two colliding objects for a given magnitude of available Δv. Then, in [Bom15], the minimisation of collision probability is also presented in the case of direct and non-direct impact.

The existing literature about continuous-thrust CAM optimisation is considerably less extensive than for the impulsive case. A fuel-optimal manoeuvre is found through the implementation of a genetic algorithm by Rasotto et al. in [Ras16]. Multi-objective particle swarm optimisers are employed by Morselli et al. [Mor14] to design optimal CAMs. Research on low-thrust optimisation methods includes the semi-analytical method developed by Reiter et al. [Rei18] for rapid collision avoidance, based on the hypothesis that the optimal thrust is always radial.

Salemme in [Sal20] employed an indirect formulation in Cartesian coordinates for Fuel-Optimal control Problem (FOP) and Energy-Optimal control Problem (EOP) solutions reaching a desired collision probability. The resulting six-dimensional optimal control problem is not easy to deal with numerically, which motivated the authors of the same paper to explore semi-analytical solutions. The dissertation of Schiavo [Sch20] is the direct continuation of the previous study and proposes computationally efficient methods (analytical and semi-analytical) for energy optimal manoeuvres with PoC as final constraint. More semi-analytical methods were proposed in [Gon19]; this approach is based on average dynamics and maximising the miss distance with the assumption of continuous tangential thrust.

The very recent work by Bombardelli and Hernando-Ayuso [Her21] investigates the problem of optimum low-thrust collision avoidance between two objects in circular orbits; the thrust vector of the manoeuvred satellite, applied continuously for a given time span, is held constant in magnitude the optimal control is written in B-plane coordinates. The B-plane formulation allows to reduce significantly the dimension of the resulting Two-Point Boundary Value Problem (TPBVP) to only two and leads to a constant costate vector.

Another recent work by Martinez Chamarro et al. [Mar21] presents two approaches to compute low-thrust CAM; the first is based on the EOP continuous solution, and a bang-bang structure is achieved by applying a smoothing approach, in the second method, the manoeuvre design is formulated as a convex optimisation problem.

A further way of automating the collision avoidance process is to use Artificial Intelligence. ESA is preparing to use machine learning to develop an automated collision avoidance system capable to assess the risk and likelihood of collisions. More than for the actual manoeuvre design phase, this method is currently very interesting for improving decision making process on whether or not a manoeuvre is needed [ESAb]. In an attempt to study this opportunity, the European Space Agency released, in October 2019, a large curated dataset containing information about close approach events, in the form of CDM, collected from 2015 to 2019. This dataset was used in the Spacecraft Collision Avoidance Challenge [Uri20], a machine learning competition where participants had to build models to predict the final collision risk between orbiting objects.

1.3 Dissertation overview

The purpose of this thesis is to provide robust and numerically efficient algorithms for different types of manoeuvres ultimately aiming at on-board autonomous implementability. For impulsive manoeuvres, the proposed analytical solutions have been extended to several operational cases. Then the dissertation focuses on low-thrust manoeuvres which have gained interest due to the recent progress on electric propulsion technology. Starting from the semi-analytical solution for the EOP proposed by Schiavo in [Sch20], a fully analytical formula is obtained; given the collision conditions and quantities in CDM format, the solution allows to design the optimal manoeuvre by substituting them directly into an analytical equation. Moreover, the case with a path constraint on the maximum control acceleration provided by the thrusters is analysed.

The thesis is divided into six chapters.

In Chapter 2, which follows here below, the underlying mathematical preliminaries that are necessary to understand the methods proposed in this work are introduced. In particular, the fundamentals of conjunction dynamics and the formulation in B-plane coordinates are first of all reported. The definition of collision probability, with a particular focus on the hypothesis of short-term encounter, is reported right after. The foundations of optimal control theory, relative to the dynamical model used to describe the motion of the satellites are then stated.

In Chapter 3 the analytical method for impulsive manoeuvres is described in detail, considering the final constraint of the PoC/SMD or MD; a separate section is dedicated to the purely tangential manoeuvre case.

Chapter 4 covers the derivation of the methods for low-thrust CAMs, both exploiting the dynamics formulation in Earth-Centered Inertial (ECI) reference frame and in B-plane (BP) coordinates. In order to match operational requirements, starting from the continuous solution of an unbounded control problem, a bang-bang structure is retrieved by applying a smoothing approach and purely tangential manoeuvres are also studied.

In Chapter 5 the performance achieved by the methods presented in Chapter 3 and Chapter 4 are analysed and compared. The algorithms are validated on a database of 2,170 collisions extracted from the ESA Collision Avoidance Competition data [ESAd]. In addition, a validation of the method in a high-fidelity dynamical

simulator including environmental perturbation (aerodynamic and gravitational effects) is provided, and comparisons in terms of computation time are shown at the end of the chapter.

In Chapter 6, the results of the present work are summarised and some recommendations for future research in this field are drawn.

CHAPTER 2

Mathematical formulation

This chapter introduces the underlying mathematical preliminaries that are necessary to understand the methods proposed in this work. In particular, the fundamentals of conjunction dynamics and the formulation in B-plane coordinates are first of all reported. The definition of collision probability, with a particular focus on the hypothesis of short-term encounter, is reported right after. The foundations of optimal control theory, relative to the dynamical model used to describe the motion of the satellites are then stated.

2.1 Conjunction analysis

Let us consider two objects experiencing a conjunction event with an expected closest approach relative position $\mathbf{r}_e$. The manoeuvrable object is called "primary", using the symbol O_p, while the debris or uncooperative object is the "secondary"

object, O_s. The state vectors (position and velocity) of the centre of mass of the primary and secondary objects respectively, expressed in a generic (inertial or a local) r.f. $\hat{\Re}$, are defined as $\mathbf{x}_p = (\mathbf{r}_p, \mathbf{v}_p)$ and $\mathbf{x}_s = (\mathbf{r}_s, \mathbf{v}_s)$. At a generic time t, the two bodies are subjected to their own dynamics, defined respectively by the vector fields $\mathbf{f}_p$ and $\mathbf{f}_s$, thus the equations of motion are written as:

$$\begin{aligned} \frac{d\,\mathbf{v}_p(t)}{dt} &= \mathbf{f}_p(t, \mathbf{x}_p), \\ \frac{d\,\mathbf{v}_s(t)}{dt} &= \mathbf{f}_s(t, \mathbf{x}_s). \end{aligned} \tag{2.1}$$

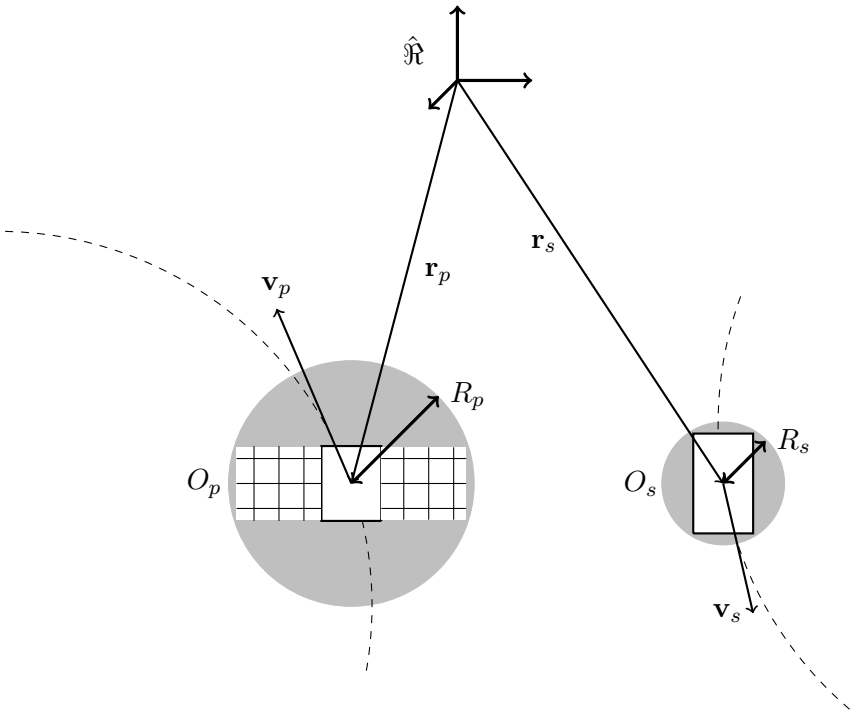

Figure 2.1: Encounter between two objects.

For any deterministic model adopted, let us suppose that, for certain initial conditions, the solutions to Cauchy problems of Eq. 2.1 are unique.
In order to define the collision domain between objects, it is necessary to characterise the related geometry, which is usually done by the Spherical geometry hypothesis: O_p and O_s are modelled as spheres of radii R_p and R_s respectively, centred in their centre of mass.
Figure 2.1 represents the space configuration of an encounter between two objects

modelled in such a way. The hypothesis over the geometry allows to neglect any information related to the orientation of the involved objects; furthermore, it remedies the lack of information related to secondary geometry and attitude and on the possible constraints over O_p. It leads to a simpler problem and to a more conservative model.

2.2 B-plane definition

Let $\{x, y, z\}$ represent an inertial reference frame (r.f.) centred at $O_p - O_s$ impact point and with axes directions defined as:

$$\mathbf{u}_x = \frac{\mathbf{v}_p}{\|\mathbf{v}_p\|}, \qquad \mathbf{u}_z = \frac{\mathbf{v}_p \times \mathbf{v}_s}{\|\mathbf{v}_p \times \mathbf{v}_s\|}, \qquad \mathbf{u}_y = \mathbf{u}_z \times \mathbf{u}_x. \tag{2.2}$$

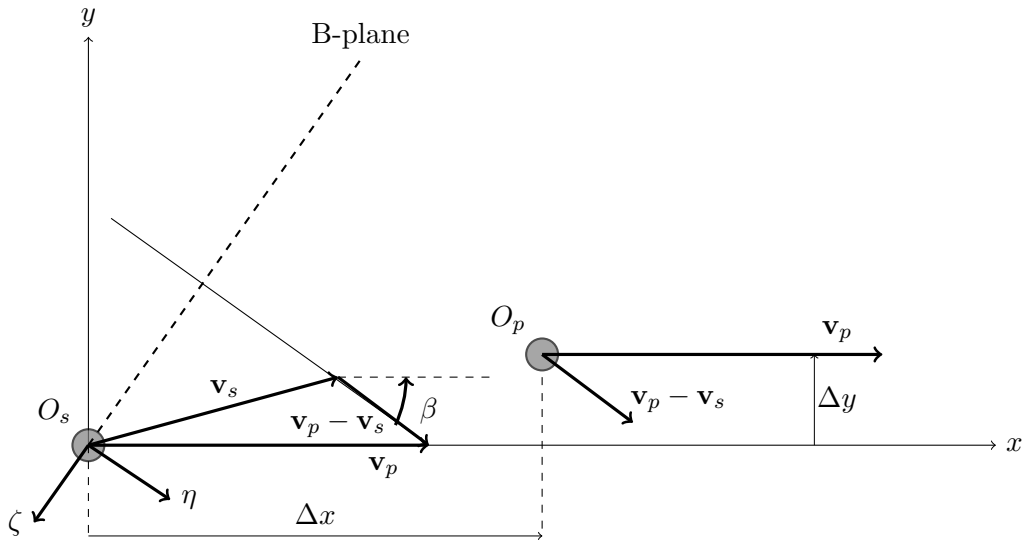

Figure 2.2: Encounter frame and B-plane: snapshot of $O_p - O_s$ encounter geometry ($x - y$ plane) after the manoeuvre.

Within a small interval of time $\Delta t \ll 1$ around the impact event, one can consider the motion of both objects as uniform rectilinear with good approximation (hypothesis of short-term encounter, Section 2.6).

In order to describe the collision avoidance dynamics using the B-plane, the formulation of [Val03], centred at O_s, is adopted. The B-plane, represented in Figure 2.2, is the encounter plane of the two colliding objects; it is perpendicular to their relative velocity $\mathbf{v}_p - \mathbf{v}_s$, and contains both of them at the moment of closest approach. The position vector $\mathbf{b}_{3D} = [\xi, \eta, \zeta]^\top$ is introduced, expressed in B-plane coordinates, defined as follows:

- $\mathbf{u}_\xi = \dfrac{\mathbf{v}_s \times \mathbf{v}_p}{\|\mathbf{v}_s \times \mathbf{v}_p\|}$ direction of the minimum orbit intersection distance (MOID) orthogonal to the geocentric velocity vectors $\mathbf{v}_p$ and $\mathbf{v}_s$;
- $\mathbf{u}_\eta = \dfrac{\mathbf{v}_p - \mathbf{v}_s}{\|\mathbf{v}_p - \mathbf{v}_s\|}$ direction of the velocity of O_p relative to O_s;
- $\mathbf{u}_\zeta = \mathbf{u}_\xi \times \mathbf{u}_\eta$ direction opposite to the projection of the B-plane of the velocity of O_s.

The unit vectors define the rotation matrix from the inertial reference frame to the B-plane

$$\mathbf{R}_{b,3\mathrm{D}} = [\mathbf{u}_\xi,\ \mathbf{u}_\eta,\ \mathbf{u}_\zeta]^\top, \tag{2.3}$$

while the projection in the η-axis is achieved by

$$\mathbf{R}_{b,2\mathrm{D}} = [\mathbf{u}_\xi,\ \mathbf{u}_\zeta]^\top. \tag{2.4}$$

At TCA, the orbital elements of O_p are defined as: a_0 semi-major axis, e_0 eccentricity, R_c radial orbital distance, θ_c true anomaly.

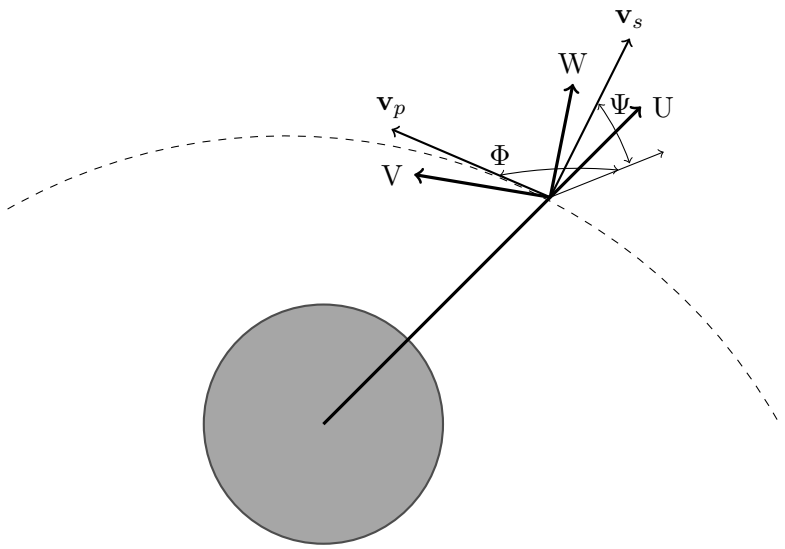

Figure 2.3: Transformation from $\mathbf{v}_p$ to $\mathbf{v}_s$.

Figure 2.3 shows the angles that describe how the velocity vector $\mathbf{v}_s$ is related to $\mathbf{v}_p$ [Bom15]:

- in-plane rotation, opposite to the orbit angular momentum direction of an angle $-\pi < \phi < \pi$ around $\mathbf{u}_{h1}$ (normal of the O_p orbital plane);

$$\phi = \text{atan2}[(\mathbf{v}_p \times \mathbf{v}_s) \cdot \mathbf{u}_{h1}, \mathbf{v}_p \cdot \mathbf{v}_s] \tag{2.5}$$

- out-of-plane rotation of an angle $-\frac{\pi}{2} < \phi < \frac{\pi}{2}$ in the direction approaching $\mathbf{u}_{h1}$;

$$\psi = \tan^{-1}\left[\frac{(\mathbf{v}_s \cdot \mathbf{u}_{h1})\,\|\mathbf{v}_s \times \mathbf{u}_{h1}\|}{v_s^2 - (\mathbf{v}_s \cdot \mathbf{u}_{h1})^2}\right] \tag{2.6}$$

- magnitude ratio $\chi = \dfrac{v_s}{v_p}$.

Additionally, for the ease of notation, the 2D position vector in the B-plane is defined as $\mathbf{b} = [\xi, \zeta]^\top$, constructed from the first and third components of the $\mathbf{b}_{3D}$ vector.

2.3 Collision avoidance kinematics

In this section [Bom14a] and [Bom15] are considered as main references. As a result of a collision avoidance manoeuvre, the position of O_p at the impact event will have shifted from the origin of $\mathbf{r} = [x, y, z]^\top$ to the point $\delta\mathbf{r} = [\delta x, \delta y, \delta z]^\top$. With reference to Figure 2.2 the image on the B-plane of $\delta\mathbf{r}$ obeys:

$$\begin{cases} \xi = -\delta z \\ \zeta = -\delta x \sin\beta - \delta y \cos\beta \end{cases} \tag{2.7}$$

where $0 < \beta \leq \pi$ is the angle between the inertial velocity O_p and the velocity of O_p relative to O_s.
$\mathbf{R}$ is the 2D rotation matrix such that:

$$\mathbf{b} = \mathbf{R}\delta\mathbf{r}, \tag{2.8}$$

$$\mathbf{R} = \begin{bmatrix} 0 & 0 & -1 \\ -\sin\beta & -\cos\beta & 0 \end{bmatrix} \tag{2.9}$$

where the angle β can be expressed as:

$$\cos\beta = \frac{(\mathbf{v}_p - \mathbf{v}_s)\cdot\mathbf{v}_p}{\|\mathbf{v}_p\|\,\|\mathbf{v}_p - \mathbf{v}_s\|} = \frac{1-\chi\cos\psi\cos\phi}{\sqrt{1-2\chi\cos\psi\cos\phi+\chi^2}} \tag{2.10}$$

$$\sin\beta = \sqrt{1-\cos^2\beta}. \tag{2.11}$$

For the singular case corresponding to $\cos\psi\cos\phi = \pm 1$ the formulation can be found in [Bom14a].

One now needs to relate $\delta x, \delta y$ and δz to the characteristics of the perturbed orbital motion of O_p, deriving the kinematics matrix $\mathbf{K}$ that verifies the linear relation:

$$\delta\mathbf{r} = \mathbf{K}\delta\mathbf{x} \quad \rightarrow \quad \mathbf{b} = \mathbf{R}\mathbf{K}\delta\mathbf{x} \tag{2.12}$$

where $\delta\mathbf{x} = [\delta t, \delta r, \delta w]^\top$ is the manoeuvre-induced time-position shift, whose components are, respectively, the accumulated time delay, radial and out-of-plane shift of the manoeuvred spacecraft at the collision true anomaly compared to its "unmanoeuvred" trajectory.

δx can be found by summing up two separate contributions $\delta x' + \delta x''$, where the $\delta x'$ refers to the time delay and the $\delta y'$ to the radial shift. Following the uniform rectilinear motion approximation, the accumulated time delay δt will give rise to a position shift along the velocity vector and its contribution can be written as:

$$\delta x' = -v_p\sqrt{\frac{R_c}{\mu}}\delta t \tag{2.13}$$

where $v_p\sqrt{\frac{R_c}{\mu}}$ is the non-dimensional velocity of the object at CA when its distance from the centre of the Earth is R_c, μ is the Earth gravitational parameter.

On the other hand, the variations δr and δw affect in general all three components of the position shift as:

$$\delta x'' = \delta r(\mathbf{u}_r\cdot\mathbf{u}_x) + \delta w(\mathbf{u}_w\cdot\mathbf{u}_x) \tag{2.14}$$

$$\delta y = \delta r(\mathbf{u}_r\cdot\mathbf{u}_y) + \delta w(\mathbf{u}_w\cdot\mathbf{u}_y) \tag{2.15}$$

$$\delta z = \delta r(\mathbf{u}_r\cdot\mathbf{u}_z) + \delta w(\mathbf{u}_w\cdot\mathbf{u}_z) \tag{2.16}$$

where:

$$\mathbf{u}_r = [\cos\theta_c, \sin\theta_c, 0]^\top \tag{2.17}$$

$$\mathbf{u}_w = [0, 0, 1]^\top. \tag{2.18}$$

By employing Eq. 2.2 and after some algebraic simplifications Eq. 2.14 yields:

$$\delta x'' = \sin\alpha_c \delta r \tag{2.19}$$

$$\delta x = -v_1\sqrt{\frac{R_c}{\mu}}\delta t + \sin\alpha_c \delta r. \tag{2.20}$$

In a similar way one can derive δy and δz.

$$\delta y = -\frac{\cos\alpha_c \sin\phi\cos\psi}{\sqrt{1-\cos^2\psi\cos^2\phi}}\delta r + \frac{\sin\psi}{\sqrt{1-\cos^2\psi\cos^2\phi}}\delta w \tag{2.21}$$

$$\delta z = \frac{\cos\alpha_c \sin\psi}{\sqrt{1-\cos^2\psi\cos^2\phi}}\delta r + \frac{\sin\phi\cos\psi}{\sqrt{1-\cos^2\psi\cos^2\phi}}\delta w \tag{2.22}$$

where α_c is the flight path angle of O_p at TCA which obeys:

$$\sin\alpha_c = \frac{e_0\sin\theta_c}{\sqrt{e_0^2+2e_0\cos\theta_c+1}}, \tag{2.23}$$

$$\cos\alpha_c = \frac{1+e_0\cos\theta_c}{\sqrt{e_0^2+2e_0\cos\theta_c+1}}. \tag{2.24}$$

Grouping Eqs. 2.20, 2.21 and 2.22 together, one obtains the matrix $\mathbf{K}$:

$$\mathbf{K} = \begin{bmatrix} -v_1\sqrt{\frac{R_c}{\mu}} & \sin\alpha_c & 0 \\ 0 & -\frac{\cos\alpha_c\sin\phi\cos\psi}{\sqrt{1-\cos^2\psi\cos^2\phi}} & \frac{\sin\psi}{\sqrt{1-\cos^2\psi\cos^2\phi}} \\ 0 & \frac{\cos\alpha_c\sin\psi}{\sqrt{1-\cos^2\psi\cos^2\phi}} & \frac{\sin\phi\cos\psi}{\sqrt{1-\cos^2\psi\cos^2\phi}} \end{bmatrix}. \tag{2.25}$$

2.4 Collision avoidance dynamics

In order to generalise the formulation for continuous-thrust manoeuvre, assume an impulsive CAM is carried out at each instant of time t, corresponding to the orbital position (r, θ), with radial, transverse and out-of-plane (LVLH r.f.) impulsive velocity variations $\Delta\mathbf{v} = [\Delta v_r, \Delta v_\theta, \Delta v_h]^\top$, respectively. Consider that in low-thrust problem: $\Delta\mathbf{v} = \mathbf{a}_c\Delta t$, where the thrust acceleration vector is $\mathbf{a}_c = [a_{c,r}, a_{c,\theta}, a_{c,h}]^\top$.
In order to have:

$$\delta\mathbf{x} = \mathbf{D}(t)\Delta\mathbf{v}, \tag{2.26}$$

the dynamics matrix $\mathbf{D}$ reads:

$$\mathbf{D} = \sqrt{\frac{R_c^3}{\mu}} \begin{bmatrix} d_{tr} & d_{t\theta} & 0 \\ d_{rr} & d_{r\theta} & 0 \\ 0 & 0 & d_{wh} \end{bmatrix} \tag{2.27}$$

where $d_{tr}, d_{t\theta}, d_{rr}, d_{r\theta}$ and d_{wh} are non-dimensional functions of time that can be derived using the generalised Pelaez' orbital elements (see [Pel07]) of the initial O_p orbit:

$$q_{10} = \frac{e_0}{\sqrt{1 + e_0 \cos\theta_c}}, \tag{2.28}$$

$$q_{30} = \frac{1}{\sqrt{1 + e_0 \cos\theta_c}}. \tag{2.29}$$

One can then express the resulting post-manoeuvre Pelaez' orbital elements as:

$$q_1 \sim q_{10} + Q_{1r}\Delta v_r + Q_{1\theta}\Delta v_\theta, \tag{2.30}$$

$$q_2 \sim Q_{2r}\Delta v_r + Q_{2\theta}\Delta v_\theta, \tag{2.31}$$

$$q_3 \sim q_{30} + Q_{3\theta}\Delta v_\theta. \tag{2.32}$$

The functions Q_i can be obtained following from the variational equations of the transverse (s) and radial (u) orbital velocity:

$$s = s_0 + \Delta v_\theta = q_{30} + q_{10}\cos\theta + \Delta v_\theta, \tag{2.33}$$

$$u = u_0 + \Delta v_r = q_{10}\sin\theta + \Delta v_r, \tag{2.34}$$

recalling that θ is the true anomaly of the manoeuvring point, and from the relations between the orbital velocity components and Pelaez' orbital elements (see [Pel07]):

$$q_3 = 1/rs, \tag{2.35}$$

$$q_1 = (s - q_3)\cos\theta + u\sin\theta, \tag{2.36}$$

$$q_2 = (s - q_3)\sin\theta - u\cos\theta, \tag{2.37}$$

with:

$$r = 1/[q_{30}(q_{30} + q_{10}\cos\theta)]. \tag{2.38}$$

By substituting Eqs. 2.35- 2.37 into Eqs. 2.30- 2.32, expanding in Taylor series until first order and solving for Q_i one finally obtains:

$$\begin{aligned}
Q_{1\theta}(\theta) &= \frac{(2q_{30} + q_{10}\cos\theta)\cos\theta}{q_{30} + q_{10}\cos\theta}, \\
Q_{1r}(\theta) &= \sin\theta, \\
Q_{2\theta}(\theta) &= \frac{(2q_{30} + q_{10}\cos\theta)\sin\theta}{q_{30} + q_{10}\cos\theta}, \\
Q_{2r}(\theta) &= -\cos\theta, \\
Q_{3\theta}(\theta) &= -\frac{q_{30}}{q_{30} + q_{10}\cos\theta}.
\end{aligned}$$

2.4.1 In-plane dynamics: radial shift

The orbit radius variation of O_p at θ_c following the collision avoidance manoeuvre obeys:

$$\delta r = \frac{1}{q_3(q_3 + q_1\cos\theta_c + q_2\sin\theta_c)} - \frac{1}{q_{30}(q_{30} + q_{10}\cos\theta_c)}. \tag{2.39}$$

By substituting the first-order expressions of q_i derived above and expanding in Taylor series until the first order one obtains:

$$\delta r = d_{rr}\Delta v_r + d_{r\theta}\Delta v_\theta, \tag{2.40}$$

where the functions $d_{ri}(\theta)$ read:

$$d_{rr} = \frac{\sin(\theta_c - \theta)}{q_{30}(q_{30} + q_{10}\cos\theta_c)^2}, \tag{2.41}$$

$$d_{r\theta} = \frac{2q_{30}(1 - \cos((\theta_c - \theta))) - q_{10}\sin\theta\sin(\theta_c - \theta)}{q_{30}(q_{30} + q_{10}\cos\theta)(q_{30} + q_{10}\cos\theta_c)^2}. \tag{2.42}$$

2.4.2 In-plane dynamics: phasing

The time elapsed along the arc $[\theta;\ \theta_c]$ can be obtained by integrating the Sundman transformation [Pel07]:

$$\Delta t = \int_\theta^{\theta_c} \frac{d\theta}{q_3 s^2} \tag{2.43}$$

where:

$$s = q_3 + q_1\cos\theta + q_2\sin\theta. \tag{2.44}$$

Eq. 2.43 can be integrated and written in the form:

$$\Delta t = \Delta t_0 + \delta t, \tag{2.45}$$

where Δt_0 is the elapsed time along the initial Keplerian orbit and Δt is the time delay caused by the impulsive Δv manoeuvre.
The term Δt_0 follows Kepler's equation and can be written in terms of the Pelaez' element set as:

$$\Delta t_0 = \frac{q_{30}(E_c - E) - q_{10}(\sin E_c) - \sin E)}{(q_{30}^2 - q_{10}^2)^{3/2}}, \tag{2.46}$$

where E_c and E are the eccentric anomalies corresponding to θ_c and θ respectively, and accounting for multiple revolutions.
After making use of the Expressions 2.30- 2.32, transforming true anomalies (θ_c, θ) into eccentric anomalies (E_c, E), and expanding in Taylor series for small $(\Delta v_r, \Delta v_\theta)$ the time delay δt follows:

$$\delta t = d_{tr}\Delta v_r + d_{t\theta}\Delta v_\theta, \tag{2.47}$$

with:

$$d_{tr} = \frac{1}{q_{30}(q_{30}^2 - q_{10}^2)^2(q_{30} - q_{10}\cos E)}[e_{r1}(E_c - E) + e_{r2}(\sin E_c - \sin E) + \\ + e_{r3}(\sin 2E_c - \sin 2E) + e_{r4}(\cos E_c - \cos E) + e_{r5}(\cos 2E_c - \cos 2E)], \tag{2.48}$$

$$d_{t\theta} = \frac{1}{q_{30}(q_{30}^2 - q_{10}^2)^{5/2}(q_{30} - q_{10}\cos E)}[e_{\theta 1}(E_c - E) + e_{\theta 2}(\sin E_c - \sin E) + \\ + e_{\theta 3}(\sin 2E_c - \sin 2E) + e_{\theta 4}(\cos E_c - \cos E) + e_{\theta 5}(\cos 2E_c - \cos 2E)], \tag{2.49}$$

where:

$$e_{\theta 1} = 3q_{30}(q_{30}^2 - q_{10}^2), \tag{2.50}$$
$$e_{\theta 2} = \frac{1}{2}[3q_{10}^3 - (2q_{30}^2 - q_{10}^2)(4q_{30}\cos E - q_{10}\cos 2E)], \tag{2.51}$$
$$e_{\theta 3} = \frac{q_{10}q_{30}}{4}[4q_{30}\cos E - q_{10}(3 + \cos 2E)], \tag{2.52}$$
$$e_{\theta 4} = q_{30}[(4q_{30}^2 - 2q_{10}^2)\sin E - q_{10}q_{30}\sin 2E], \tag{2.53}$$
$$e_{\theta 5} = -\frac{q_{10}}{4}[(4q_{30}^2 - 2q_{10}^2)\sin E - q_{10}q_{30}\sin 2E], \tag{2.54}$$
$$e_{r1} = 3q_{10}q_{30}\sin E, \tag{2.55}$$

$$e_{r2} = -2(q_{30}^2 + q_{10}^2)\sin E, \tag{2.56}$$
$$e_{r3} = \frac{q_{10}q_{30}}{2}\sin E, \tag{2.57}$$
$$e_{r4} = -2q_{30}(q_{30}\cos E - q_{10}), \tag{2.58}$$
$$e_{r5} = \frac{q_{10}}{2}(q_{30}\cos E - q_{10}). \tag{2.59}$$

2.4.3 Out-of-plane dynamics

The out of plane motion is decoupled from the planar one and can be described with sufficient accuracy by linearising the gravitational acceleration (Lawden's Equations)

$$\delta w = d_{wh} u_h \delta t. \tag{2.60}$$

A closed-form analytical solution of the out-of-plane Lawden's equation can be found by using the true anomaly as an independent variable as done in [Yam02]. From that reference, and indicating with p_0 the initial orbital parameter, the dimensional out-of-plane displacement can be written as:

$$\delta Z = \sqrt{\frac{p_0^3}{\mu}} \frac{\sin(\theta_c - \theta)}{(1 + e_0\cos\theta_c)(1 + e_0\cos\theta)} u_h \delta t. \tag{2.61}$$

After re-scaling the different quantities according to the present non-dimensionalisation one obtains:

$$d_{wh} = \frac{\sqrt{q_{30}^2 + q_{10}q_{30}\cos\theta_c}}{q_{30} + q_{10}\cos\theta}\sin(\theta_c - \theta). \tag{2.62}$$

2.5 CAM dynamics in B-plane coordinates

This section summarises the dynamics in B-plane coordinates after the derivations reported in the previous sections, and specifies the equations of motion for both the cases of impulsive manoeuvre and continuous-thrust CAM.

Impulsive manoeuvre

In case of direct impact, i.e., the position of the primary and secondary objects at TCA coincides, combining Eqs. 2.8, 2.12 and 2.26 yeilds:

$$\mathbf{b} = \mathbf{RKD}\Delta\mathbf{v} = \mathbf{M}\Delta\mathbf{v}, \tag{2.63}$$

where $\mathbf{R}, \mathbf{K}, \mathbf{D}$ are matrices derived in the previous sections, hence $\mathbf{M}$ is function of: $\phi, \psi, \chi, e_0, a_0, \theta_c, \mu$ and θ.
Considering the general case of a non-direct impact (i.e., a conjunction whose expected miss distance is not zero) where $\mathbf{b}_e$ is the relative position of the two objects at TCA in B-plane r.f:

$$\mathbf{b}_e = \mathbf{R}_{b,2\mathrm{D}}\mathbf{r}_e = \mathbf{R}_{b,2\mathrm{D}}(\mathbf{r}_p - \mathbf{r}_s). \tag{2.64}$$

Hence the position $\mathbf{b}$ at a generic time after the impulsive manoeuvre can be written as:

$$\mathbf{b} = \mathbf{b}_e + \mathbf{M}\Delta\mathbf{v}. \tag{2.65}$$

Low-thrust manoeuvre

When the manoeuvrable spacecraft O_p is equipped with a low-thrust propulsion system, a realistic CAM scheme is to apply optimally oriented thrust acceleration continuously over a thrust arc. In an infinitesimal time δt, the acceleration produces the velocity variation

$$\delta\mathbf{v} = \mathbf{a}_c\delta t. \tag{2.66}$$

This leads to a B-plane displacement $\delta\mathbf{b} = [\delta\xi, \delta\zeta]^\top$ (see Section 2.4) :

$$\delta\mathbf{b} = \mathbf{RKD}\mathbf{a}_c\delta t = \mathbf{M}\mathbf{a}_c\delta t. \tag{2.67}$$

Approximating to the first order Eq. 2.67, it is obtained:

$$\frac{d\mathbf{b}}{dt} = \mathbf{M}\mathbf{a}_c \tag{2.68}$$

and the dynamics of the system can be written as:

$$\begin{cases} \dot{\mathbf{b}} = \mathbf{M}\mathbf{a}_c \\ \mathrm{IC}: \quad \mathbf{b}(t_0) = \mathbf{b}_e = [\xi_e, \zeta_e]^\top. \end{cases} \tag{2.69}$$

2.6 Collision probability and squared Mahalanobis distance

Assuming a spherical geometry, a collision is assumed to occur in a time interval I if and only if a date $\bar{t}\ \epsilon\ I$ exists such that:

$$\left\|\mathbf{r}(\bar{t})\right\| = \left\|\mathbf{r}_p(\bar{t}) - \mathbf{r}_s(\bar{t})\right\| \leq R_p + R_s. \tag{2.70}$$

Under a relative position point of view, the collision assembly at an instant $\bar{t}$ can be replaced by a fictitious combined sphere of radius $s_A = R_p + R_s$: it is the hard body radius, shown in Figure 2.4.

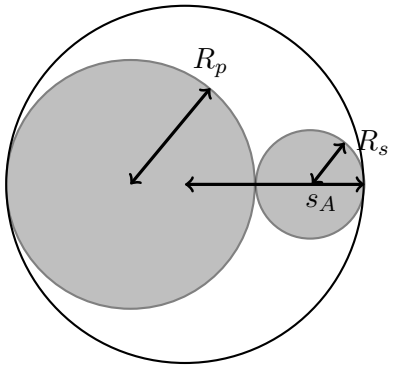

Figure 2.4: Combined body representation.

The Probability of Collision (PoC) can be written, in general terms, as the triple integral of the probability distribution function $f_r(\mathbf{r})$ of the relative position of primary object with respect to the second over the volume V swept by a sphere of radius s_A centred at secondary body:

$$\text{PoC} = \int_V f_r(\mathbf{r}) \mathrm{d}\mathbf{r}. \tag{2.71}$$

When the Gaussian PDF of this relative position $f_r(\mathbf{r})$ is given by:

$$f_r(\mathbf{r}) = \frac{1}{\sqrt{2\pi^3 \det \mathbf{C}_r}} \exp\left[-\frac{1}{2}(\mathbf{r}-\mathbf{r}_e)^\top \mathbf{C}_r^{-1}(\mathbf{r}-\mathbf{r}_e)\right], \tag{2.72}$$

where $\mathbf{C}_r$ is the covariance matrix of $\mathbf{r}$, which corresponds to the sum of the individual covariance matrices of the two bodies, expressed in the same orthonormal base, when the two (Gaussian) quantities are statistically independent.
Considering the short-term encounter hypothesis, described in a dedicated paragraph 2.6, one can consider the motion of the two objects as uniform rectilinear with deterministically known velocities, and compute the collision probability as a two-dimensional integral on the collision B-plane.
With such an approximation, the integration volume is reduced over a disk centred in the origin (see [Mon19] for a detailed derivation), and Eq. 2.71 can be rewritten

as a 2D integral:

$$\mathrm{PoC} = \int_A \frac{1}{2\pi\sigma_\xi\sigma_\zeta\sqrt{1-\rho_{\xi\zeta}^2}} \exp\Bigg\{ -\frac{1}{2(1-\rho_{\xi\zeta}^2)}\Bigg[\left(\frac{\xi-\xi_e}{\sigma_\xi}\right)^2 + \left(\frac{\zeta-\zeta_e}{\sigma_\zeta}\right)^2 + \\ - 2\rho_{\xi\zeta}\left(\frac{\xi-\xi_e}{\sigma_\xi}\right)\left(\frac{\zeta-\zeta_e}{\sigma_\zeta}\right)\Bigg]\Bigg\} \mathrm{d}\xi\mathrm{d}\zeta, \quad (2.73)$$

where $r_e = [\xi_e, 0, \zeta_e]^\top$ is the expected closest approach relative position in the B-plane; A is a circular domain of radius s_A; σ_ξ, σ_ζ, and $\rho_{\xi\zeta}$ can be extracted from the relative position covariance matrix in B-plane axes whose $\{\xi, \zeta\}$ submatrix reads:

$$\mathbf{C}_{\xi\zeta} = \begin{bmatrix} \sigma_\xi^2 & \rho_{\xi\zeta}\sigma_\xi\sigma_\zeta \\ \rho_{\xi\zeta}\sigma_\xi\sigma_\zeta & \sigma_\zeta^2 \end{bmatrix}. \quad (2.74)$$

There are several methods for calculating the 2D collision probability, many of which are collected and compared in [Mon19]. In this thesis, it has been chosen to follow PoC definition by Chan in [Cha08] truncated at $m = 3$. The computation of Eq. 2.73 can be made equivalent to integrating a properly scaled isotropic Gaussian distribution function over an elliptical cross section. If the latter is approximated as a circular cross section of equal area, the final computation of the collision probability reduces to a Rician integral that can be computed with the convergent series:

$$\mathrm{PoC}(u, v) = e^{-\frac{v}{2}} \sum_{m=0}^{\infty} \frac{v^m}{2^m m!} \left[1 - e^{-\frac{u}{2}} \sum_{k=0}^{m} \frac{u^k}{2^k k!}\right], \quad (2.75)$$

where u is the ratio of the impact cross-sectional area to the area of the 1σ covariance ellipse in the B-plane:

$$u = \frac{s_A^2}{\sigma_\xi\sigma_\zeta\sqrt{1-\rho_{\xi\zeta}^2}}, \quad (2.76)$$

and v is the squared Mahalanobis distance (SMD):

$$v = \mathrm{SMD} = \left[\left(\frac{\xi_e}{\sigma_\xi}\right)^2 + \left(\frac{\zeta_e}{\sigma_\zeta}\right)^2 - 2\rho_{\xi\zeta}^2\frac{\xi_e\zeta_e}{\sigma_\xi\sigma_\zeta}\right]/(1-\rho_{\xi\zeta}^2), \quad (2.77)$$

$$= (\mathbf{r}_f - \mathbf{r}_s)^\top \mathbf{R}_{b,2\mathrm{D}}^\top \mathbf{C}^{-1} \mathbf{R}_{b,2\mathrm{D}} (\mathbf{r}_f - \mathbf{r}_s), \quad (2.78)$$

$$= \mathbf{b}_f^\top \mathbf{C}^{-1} \mathbf{b}_f. \quad (2.79)$$

Two functions for the computation of PoC and SMD, following Eqs. 2.75 and 2.78 are implemented: *poc_chan*($\Delta\mathbf{r}$, CDM), *squared_mahalanobis_distance*($\Delta\mathbf{r}$, CDM) and the function *poc2smd*(PoC, CDM) allows to calculate the SMD corresponding to a given value of PoC.

Isotropic approximation and miss distance

Retaining only the first term of the series ($m = 0$), the collision probability can be expressed as:

$$\mathrm{PoC}_{\mathrm{iso}} = e^{-\frac{v}{2}}(1 - e^{-\frac{u}{2}}). \tag{2.80}$$

According to [Rei18], Eq. 2.80 can be written as:

$$\mathrm{PoC}_{\mathrm{iso}} = \exp\left\{ \ln\left(1 - e^{-\frac{s_A^2}{2\sigma^2}}\right) - \frac{1}{2}\frac{d^2}{\sigma^{*2}} \right\}, \tag{2.81}$$

where $\sigma = \sqrt{\sigma_\xi \sigma_\zeta}$, $\sigma^* = \max\{\sigma_\xi, \sigma_\zeta\}$ and d is the miss distance:

$$d = \sqrt{\xi_e^2 + \zeta_e^2} = \|\mathbf{b}_f\| = \|\mathbf{R}_{b,2\mathrm{D}}(\mathbf{r}_f - \mathbf{r}_s)\|\,. \tag{2.82}$$

Short-term encounter approximation

In some encounters the temporal extent of the conjunction is small compared with the orbit period of the objects; this configuration leads to pose additional hypotheses, in order to define the so-called short-term encounter model. The fundamental hypothesis is the rectilinear motion, based on the small curvature of the trajectory in the closest approach. In such a frame, collision probability admits a simplified expression, in the form of a 2D integral. A close encounter can be regarded as short-term depending not only on the relative encounter velocity but also on the size of the covariance ellipsoid.
Setting a reference conjunction duration t_c required by the primary object to cross the 1σ relative position uncertainty ellipsoid in the η direction:

$$t_c = \frac{2\sigma_\eta}{\|\mathbf{v}_p - \mathbf{v}_s\|}, \tag{2.83}$$

a short-term encounter is characterised by a time t_c much smaller with respect to its orbital period T_p:

$$\epsilon = \frac{t_c}{T_p} \ll 1. \tag{2.84}$$

Based on numerical analyses conducted by other authors, one can consider $\epsilon < 1 \cdot 10^{-3}$ as a safe reasonable limit for the short-term encounter hypothesis [Cha08]. Cases in which this condition is not verified are extremely unusual in LEO.

2.7 Optimal control theory

In the following section the general formulation of an Optimal Control Problem (OCP) is introduced, considering [Bry75] as the main reference. OCP consists in finding the function $\mathbf{u}(t)$ that minimise (or maximise) a performance index J. The resolutive methods can be divided into two classes: indirect methods, exploiting the analytical optimality conditions arising from the calculus of variations, and direct methods, converting the continuous optimal control problem into a parameter optimisation problem. This dissertation deals extensively with the indirect optimisation problem, where the objective function is expressed in the Bolza form. Given the generic dynamic system:

$$\begin{cases} \dot{\mathbf{x}} = \mathbf{f}(\mathbf{x}(t), \mathbf{u}(t), t) \\ \mathbf{x}(t_0) = \mathbf{x}_0, \end{cases} \tag{2.85}$$

the cost function J is expressed in the Bolza form:

$$J = \Phi(\mathbf{x}(t_f), t_f) + \int_{t_0}^{t_f} L(\mathbf{x}(t), \mathbf{u}(t), t)\, \mathrm{d}t, \tag{2.86}$$

where L is the performance index. Considering the Lagrange multiplier vector $\boldsymbol{\lambda}(t)$, the Hamiltonian function H is defined as:

$$H = L + \boldsymbol{\lambda}^\top \mathbf{f}. \tag{2.87}$$

Adjoining the system of equations $\mathbf{f}(\mathbf{x}(t), \mathbf{u}(t), t) = \dot{\mathbf{x}}$ to J with multipliers, one obtains:

$$J = \Phi(\mathbf{x}(t_f), t_f) + \int_{t_0}^{t_f} \{H(\mathbf{x}(t), \mathbf{u}(t), t) - \boldsymbol{\lambda}^\top(t)\dot{\mathbf{x}}(t)\}\, \mathrm{d}t, \tag{2.88}$$

$$J = \Phi(\mathbf{x}(t_f), t_f) + \int_{t_0}^{t_f} \{L(\mathbf{x}(t), \mathbf{u}(t), t) + \boldsymbol{\lambda}^\top(t)\, [\mathbf{f}(\mathbf{x}(t), \mathbf{u}(t), t) - \dot{\mathbf{x}}(t)]\}\, \mathrm{d}t. \tag{2.89}$$

In some problems, as in this thesis, it is of interest to constrain functions of the terminal state to have prescribed values; that is:

$$\Psi(\mathbf{x}(t_f), t_f) = 0. \tag{2.90}$$

Hence:

$$\Phi(\mathbf{x}(t_f), t_f) = \phi(\mathbf{x}(t_f), t_f) + \boldsymbol{\nu}^\top \Psi(\mathbf{x}(t_f), t_f) \tag{2.91}$$

adjoined to J by a multiplier vector $\boldsymbol{\nu}$, and the augmented performance index is:

$$\overline{J} = \phi(\mathbf{x}(t_f), t_f) + \boldsymbol{\nu}^\top \Psi(\mathbf{x}(t_f), t_f) + \int_{t_0}^{t_f} \{L(\mathbf{x}(t), \mathbf{u}(t), t) + \\ + \boldsymbol{\lambda}^\top(t) \left[\mathbf{f}(\mathbf{x}(t), \mathbf{u}(t), t) - \dot{\mathbf{x}}(t)\right]\} \, \mathrm{d}t. \tag{2.92}$$

Using the Pontryagin's Maximum Principle, the so-called Hamiltonian system associated with the optimal control problem can be written:

$$\begin{cases} \dot{\mathbf{x}} = \mathbf{f}(\mathbf{x}(t), \mathbf{u}(t), t) \\ \dot{\boldsymbol{\lambda}} = -\left(\dfrac{\partial H}{\partial \mathbf{x}}\right)^\top \\ \mathbf{x}(t_0) = \mathbf{x}_0 \\ \boldsymbol{\lambda}(t_f) = \left(\dfrac{\partial \Phi}{\partial \mathbf{x}_f}\right)^\top \\ \mathbf{u} = \arg\min_{\mathbf{u}} H \quad \rightarrow \frac{\partial H}{\partial \mathbf{u}} = 0. \end{cases} \tag{2.93}$$

The Hamiltonian system can be then formulated as a Two-Point Boundary Value Problem (TPBVP).

2.7.1 Restricted two-body problem

The motion of a massless particle (a particle with a mass infinitesimally small with respect to the other bodies, for example a satellite) is studied through the *restricted* n-body problem.
For $n = 2$ the problem is completely solved and even though for Earth satellites it is not as representative of the actual dynamics as a three-body model, it is often used for preliminary mission design stages. The equation of motion is:

$$\ddot{\mathbf{r}} = -\frac{\mu}{r^3}\mathbf{r}. \tag{2.94}$$

When also the control acceleration $\mathbf{a}_c$ of the spacecraft is taken into account, the set of first-order differential equations that describe the controlled dynamics,

accounting for mass variation is:

$$\begin{cases} \dot{\mathbf{r}} = \mathbf{v} \\ \dot{\mathbf{v}} = -\dfrac{\mu}{r^3}\mathbf{r} + \mathbf{a}_c \\ \dot{m} = -\dfrac{1}{c_e}\left\|\mathbf{a}_c\right\| m \end{cases} \qquad \text{ICs} : \begin{cases} \mathbf{r}(t_0) = \mathbf{r}_0 \\ \mathbf{v}(t_0) = \mathbf{v}_0 \\ m(t_0) = m_0 \end{cases} \tag{2.95}$$

where c_e is the effective exhaust velocity $c_e = I_{sp}\, g_0$.

State Transition Matrix

The State Transition Matrix (STM) maps the variation of the state $\delta\mathbf{x}$ at an arbitrary final time t with respect to $\delta\mathbf{x}_0$ at an arbitrary time t_0. Considering:

$$\mathbf{x}(\mathbf{x}_0 + \delta\mathbf{x}_0, t) = \mathbf{x}(\mathbf{x}_0, t) + \delta\mathbf{x}(t) \simeq \mathbf{x}(\mathbf{x}_0, t) + \frac{\partial \mathbf{x}}{\partial \mathbf{x}_0}\delta\mathbf{x}_0, \tag{2.96}$$

STM is defined as the matrix $\mathbf{\Phi}(t, t_0)$ such that:

$$\mathbf{\Phi}(t, t_0) = \frac{\delta\mathbf{x}}{\delta\mathbf{x}_0}. \tag{2.97}$$

For time-varying systems, STM is found by integrating

$$\dot{\mathbf{\Phi}}(t, t_0) = \mathbf{A}(t)\mathbf{\Phi}(t_0, t_0), \qquad \mathbf{\Phi}(t_0, t_0) = \mathbb{I}_{n\times n}, \tag{2.98}$$

where $\mathbf{A}(t)$ is the state matrix of the linear system

$$\dot{\mathbf{x}}(t) = \mathbf{A}(t)\mathbf{x}(t). \tag{2.99}$$

In the non-linear problems of Chapter 4, the goal is to linearise the equations of motion $\mathbf{f}(\mathbf{x}, t)$ of the Energy-Optimal control Problem (EOP) around the nominal trajectory represented by the state $\mathbf{x}_n$, hence:

$$\mathbf{A}(t) = \left.\frac{\partial \mathbf{f}(\mathbf{x}, t)}{\partial \mathbf{x}}\right|_{\mathbf{x_n}}. \tag{2.100}$$

CHAPTER 3

Impulsive collision avoidance manoeuvres

The analytical methods proposed for impulsive manoeuvres are described in detail in this chapter, considering the final constraint on the PoC/SMD or MD. The formulation proposed by Bombardelli and Hernando-Ayuso in [Bom15] has been adopted. In literature, solutions for impulsive manoeuvres have been proposed in order to optimise the probability of collision or the miss distance by imposing a constraint on the maximum magnitude of the impulse Δv. In this chapter the problem is formulated with the aim of minimising the total cost of a manoeuvre that does not exceed an enforced threshold of PoC, SMD or MD, and it is resolved with a fully analytical solution. A separate section is dedicated to the analysis of the problem with the further constraint of a purely tangential manoeuvre.

3.1 Optimal impulsive manoeuvre with final constraint

The optimisation problem for the impulsive manoeuvre case is presented with two types of final constraint: Squared Mahalanobis Distance and Miss Distance. The first formulation subjected to a threshold in terms of SMD also includes the possibility of setting a collision probability value, since one can translate the PoC limit to the corresponding SMD.

Squared Mahalanobis distance constraint

The impulsive manoeuvre implemented in this section minimises the impulse magnitude Δv by prescribing the final PoC (corresponding to a SMD value).
The goal of the problem is to minimise the cost function defined as:

$$J = \int_{t_0}^{t_f} L \mathrm{d}t, \quad L = \Delta\mathbf{v}^\top \Delta\mathbf{v}, \tag{3.1}$$

subjected to $f(\Delta\mathbf{v}) = 0$:

$$f(\Delta\mathbf{v}) = \mathrm{SMD}(\mathbf{b}_f) - \overline{\mathrm{SMD}} \quad \longrightarrow \quad \mathbf{b}_f^\top \mathbf{C}^{-1} \mathbf{b}_f - \overline{\mathrm{SMD}} = 0, \tag{3.2}$$

where the impulse vector $\Delta\mathbf{v}$ is expressed in LVLH coordinates (radial, transverse, out-of-plane) and $\overline{\mathrm{SMD}}$ is the enforced value of the Squared Mahalanobis Distance linked to the final position in B-plane coordinates $\mathbf{b}_f = \mathbf{b}(t_f)$.
Using Eq. 2.65:

$$\mathbf{b}_f = \mathbf{b}_e + \mathbf{M}\Delta\mathbf{v}. \tag{3.3}$$

Plugging Eq. 3.3 into Eq. 3.2:

$$f(\Delta\mathbf{v}) = (\mathbf{b}_e + \mathbf{M}\Delta\mathbf{v})^\top \mathbf{C}^{-1} (\mathbf{b}_e + \mathbf{M}\Delta\mathbf{v}) - \overline{\mathrm{SMD}}, \tag{3.4}$$

$$f(\Delta\mathbf{v}) = \mathbf{b}_e^\top \mathbf{C}^{-1} \mathbf{b}_e + \Delta\mathbf{v}^\top \mathbf{A} \Delta\mathbf{v} + 2\mathbf{b}_e^\top \mathbf{C}^{-1} \mathbf{M} \Delta\mathbf{v} - \overline{\mathrm{SMD}}. \tag{3.5}$$

where the matrix $\mathbf{A}$ is defined as:

$$\mathbf{A} = \mathbf{M}^\top \mathbf{C}^{-1} \mathbf{M}. \tag{3.6}$$

The Hamiltonian reads:

$$H(\Delta\mathbf{v}, \lambda) = L - \lambda f(\Delta\mathbf{v}), \tag{3.7}$$

$$H = \Delta\mathbf{v}^\top\Delta\mathbf{v} - \lambda(\mathbf{b}_e^\top\mathbf{C}^{-1}\mathbf{b}_e + \Delta\mathbf{v}^\top\mathbf{A}\Delta\mathbf{v} + 2\mathbf{b}_e^\top\mathbf{C}^{-1}\mathbf{M}\Delta\mathbf{v} - \overline{\mathrm{SMD}}). \tag{3.8}$$

The optimal impulsive manoeuvre can be obtained by solving the system:

$$\begin{cases} \dfrac{\partial H}{\partial \Delta\mathbf{v}} = 0 \\ \\ \dfrac{\partial H}{\partial \lambda} = 0 \end{cases} \quad \begin{cases} 2\Delta\mathbf{v} - \lambda(2\mathbf{A}\Delta\mathbf{v} + (2\mathbf{b}_e^\top\mathbf{C}^{-1}\mathbf{M})^\top) = 0 \\ \\ \mathbf{b}_e^\top\mathbf{C}^{-1}\mathbf{b}_e + \Delta\mathbf{v}^\top\mathbf{A}\Delta\mathbf{v} + 2\mathbf{b}_e^\top\mathbf{C}^{-1}\mathbf{M}\Delta\mathbf{v} - \overline{\mathrm{SMD}} = 0. \end{cases} \tag{3.9}$$

Through the following steps the solution is obtained in terms of $\Delta\mathbf{v}$ and λ.
The first row of Eq. 3.9 can be written as:

$$\Delta\mathbf{v} = \lambda(\mathbb{I}_{3\times3} - \lambda\mathbf{A})^{-1}(\mathbf{b}_e^\top\mathbf{C}^{-1}\mathbf{M})^\top. \tag{3.10}$$

Let us define $\mathbf{c} = (\mathbf{b}_e^\top\mathbf{C}^{-1}\mathbf{M})^\top$, then the system in Eq. 3.9 becomes:

$$\begin{cases} \Delta\mathbf{v} = \lambda(\mathbb{I} - \lambda\mathbf{A})^{-1}\mathbf{c} \\ \\ \mathbf{b}_e^\top\mathbf{C}^{-1}\mathbf{b}_e + \lambda^2[(\mathbb{I} - \lambda\mathbf{A})^{-1}\mathbf{c}]^\top\mathbf{A}(\mathbb{I} - \lambda\mathbf{A})^{-1}\mathbf{c} + \\ \quad +2\lambda\mathbf{c}^\top(\mathbb{I} - \lambda\mathbf{A})^{-1}\mathbf{c} - \overline{\mathrm{SMD}} = 0. \end{cases} \tag{3.11}$$

Since:

$$(\mathbb{I} - \lambda\mathbf{A})^{-1} = \frac{1}{\det(\mathbb{I} - \lambda\mathbf{A})}[\mathbb{I} - \lambda\det\mathbf{A}\cdot\mathbf{A}^{-1}], \tag{3.12}$$

and defining also $\widetilde{\mathbf{A}} = \det\mathbf{A}\cdot\mathbf{A}^{-1}$:

$$(\mathbb{I} - \lambda\mathbf{A})^{-1} = \frac{1}{\det(\mathbb{I} - \lambda\mathbf{A})}(\mathbb{I} - \lambda\widetilde{\mathbf{A}}), \tag{3.13}$$

the second row of Eq. 3.11 reads:

$$\begin{aligned} \det^2(\mathbb{I} - \lambda\mathbf{A})\mathbf{b}_e^\top\mathbf{C}^{-1}\mathbf{b}_e + \lambda^2[(\mathbb{I} - \lambda\widetilde{\mathbf{A}})\mathbf{c}]^\top\mathbf{A}(\mathbb{I} - \lambda\widetilde{\mathbf{A}})\mathbf{c} + \\ + 2\lambda\det(\mathbb{I} - \mathbf{A})\mathbf{c}^\top(\mathbb{I} - \lambda\widetilde{\mathbf{A}})\mathbf{c} - \det^2(\mathbb{I} - \lambda\mathbf{A})\overline{\mathrm{SMD}} = 0. \end{aligned} \tag{3.14}$$

After some simple algebraic steps:

$$\begin{aligned} \det^2(\mathbb{I} - \lambda\mathbf{A})\mathbf{b}_e^\top\mathbf{C}^{-1}\mathbf{b}_e + \lambda^2[\mathbf{c}^\top - \lambda(\widetilde{\mathbf{A}}\mathbf{c})^\top]\mathbf{A}(\mathbf{c} - \lambda\widetilde{\mathbf{A}}\mathbf{c}) + \\ + 2\lambda\det(\mathbb{I} - \lambda\mathbf{A})\mathbf{c}^\top(\mathbf{c} - \lambda\widetilde{\mathbf{A}}\mathbf{c}) - \det^2(\mathbb{I} - \lambda\mathbf{A})\overline{\mathrm{SMD}} = 0 \end{aligned} \tag{3.15}$$

$$\det^2(\mathbb{I}-\lambda\mathbf{A})\mathbf{b}_e^\top\mathbf{C}^{-1}\mathbf{b}_e+\lambda^2\mathbf{c}^\top\mathbf{A}\mathbf{c}-2\lambda^3\mathbf{c}^\top\mathbf{A}\widetilde{\mathbf{A}}\mathbf{c}+\lambda^4\mathbf{c}^\top\widetilde{\mathbf{A}}^\top\mathbf{A}\widetilde{\mathbf{A}}\mathbf{c}+$$
$$+2\lambda\det(\mathbb{I}-\lambda\mathbf{A})\mathbf{c}^\top\mathbf{c}-2\lambda^2\det(\mathbb{I}-\lambda\mathbf{A})\mathbf{c}^\top\widetilde{\mathbf{A}}\mathbf{c}-\det^2(\mathbb{I}-\lambda\mathbf{A})\overline{\mathrm{SMD}}=0. \quad (3.16)$$

The problem is solved in a completely analytical way and the $\Delta\mathbf{v}$ can be computed by solving Eq. 3.16 in a closed-form for λ, and then plugging this value into Eq. 3.10.
Equation 3.16 has six solutions, since the term with the quadratic determinant contains λ at the sixth degree. Two of them are complex; the other four corresponds to the two local minima and two local maxima in terms of Δv.
The whole method is summarised in Algorithm 1, and all the mentioned functions are explained in Nomenclature.

Algorithm 1 Optimal impulsive CAM

Input: CDM, $\overline{\mathrm{SMD}}$, $\Delta\theta$_range
Output: $\mathbf{r}_f$, epoch_opt, $\Delta\theta$_opt, SMD, PoC,$\Delta\mathbf{v}$_opt
for i = 1 : *size*($\Delta\theta$_range) **do**
    $\Delta\theta = \Delta\theta$_range($i$)
    $\theta_m = \theta_{\mathrm{TCA}} - \Delta\theta$
    T interval of time corresponding to $\Delta\theta$
    tspan_backward = [T 0]
    tspan_forward = [0 T]
    $[\mathbf{r}_0, \mathbf{v}_0]$ = *keplerian_propagator*($[\mathbf{r}_{\mathrm{TCA}}, \mathbf{v}_{\mathrm{TCA}}]$, tspan_backward)
    compute B-plane kinematics and dynamics $(\mathbf{R}, \mathbf{K}, \mathbf{D} \rightarrow \mathbf{M})$
    compute $\Delta\mathbf{v}(i)$ by means of Eq. 3.16
end for
$\Delta\theta$_opt = true anomaly corresponding to $min(\|\Delta\mathbf{v}\|)$
epoch_opt= epoch corresponding to $\Delta\theta$_opt
$\Delta\mathbf{v}$_opt = $\Delta\mathbf{v}(\Delta\theta$_opt)
$[\mathbf{r}_f, \mathbf{v}_f]$ = *keplerian_propagator*($[\mathbf{r}_0, \mathbf{v}_0]$, tspan_forward) $\rightarrow \mathbf{r}_f$
$\Delta\mathbf{r} = \mathbf{r}_f - \mathbf{r}_s$
SMD = *squared_mahalanobis_distance*($\Delta\mathbf{r}$, CDM)
PoC = *poc_chan*($\Delta\mathbf{r}$, CDM)

Miss distance constraint

An approach similar to the one explained for constrained SMD can be used to design a manoeuvre with a threshold on the final miss distance. The constraint

functions $f(\Delta\mathbf{v}) = 0$ becomes:

$$f(\Delta\mathbf{v}) = \mathbf{b}_f^\top \mathbf{b}_f - \overline{d}^2, \tag{3.17}$$

where $\overline{d}$ is the imposed value of MD. By means of Eq. 3.3:

$$f(\Delta\mathbf{v}) = (\mathbf{b}_e + \mathbf{M}\Delta\mathbf{v})^\top(\mathbf{b}_e + \mathbf{M}\Delta\mathbf{v}) - \overline{d}^2, \tag{3.18}$$

$$f(\Delta\mathbf{v}) = \mathbf{b}_e^\top \mathbf{b}_e + \Delta\mathbf{v}^\top \mathbf{M}^\top \mathbf{M}\Delta\mathbf{v} + 2\mathbf{b}_e^\top \mathbf{M}\Delta\mathbf{v} - \overline{d}^2. \tag{3.19}$$

The Hamiltonian is:

$$H = \Delta\mathbf{v}^\top\Delta\mathbf{v} - \lambda(\mathbf{b}_e^\top \mathbf{b}_e + \Delta\mathbf{v}^\top \mathbf{M}^\top \mathbf{M}\Delta\mathbf{v} + 2\mathbf{b}_e^\top \mathbf{M}\Delta\mathbf{v} - \overline{d}^2), \tag{3.20}$$

and one can obtain the system:

$$\begin{cases} \Delta\mathbf{v} - \lambda(\mathbf{M}^\top\mathbf{M}\Delta\mathbf{v} + (\mathbf{b}_e^\top\mathbf{M})^\top) = 0 \\ \mathbf{b}_e^\top \mathbf{b}_e + \Delta\mathbf{v}^\top \mathbf{M}^\top \mathbf{M}\Delta\mathbf{v} + 2\mathbf{b}_e^\top \mathbf{M}\Delta\mathbf{v} - \overline{d}^2 = 0. \end{cases} \tag{3.21}$$

The first row of Eq. 3.21 can be written as:

$$\Delta\mathbf{v} = \lambda(\mathbb{I}_{3\times3} - \lambda\mathbf{M}^\top\mathbf{M})^{-1}(\mathbf{b}_e^\top\mathbf{M})^\top. \tag{3.22}$$

Let us define

$$\mathbf{d} = (\mathbf{b}_e^\top\mathbf{M})^\top \text{ and } \mathbf{D} = \mathbf{M}^\top\mathbf{M}, \tag{3.23}$$

the system in Eq. 3.21 reads:

$$\begin{cases} \Delta\mathbf{v} = \lambda(\mathbb{I} - \lambda\mathbf{D})^{-1}\mathbf{d} \\ \mathbf{b}_e^\top \mathbf{b}_e + \lambda^2[(\mathbb{I} - \lambda\mathbf{D})^{-1}\mathbf{d}]^\top\mathbf{D}(\mathbb{I} - \lambda\mathbf{D})^{-1}\mathbf{d} + 2\lambda\mathbf{d}^\top(\mathbb{I} - \lambda\mathbf{D})^{-1}\mathbf{d} - \overline{d}^2 = 0. \end{cases} \tag{3.24}$$

The second row of Eq. 3.24 becomes:

$$\begin{aligned} \det^2(\mathbb{I} - \lambda\mathbf{D})\mathbf{b}_e^\top \mathbf{b}_e + \lambda^2[(\mathbb{I} - \lambda\widetilde{\mathbf{D}})\mathbf{d}]^\top\mathbf{D}(\mathbb{I} - \lambda\widetilde{\mathbf{D}})\mathbf{d} + \\ + 2\lambda\det(\mathbb{I} - \mathbf{D})\mathbf{d}^\top(\mathbb{I} - \lambda\widetilde{\mathbf{D}})\mathbf{d} - \det^2(\mathbb{I} - \lambda\mathbf{D})\overline{d}^2 = 0 \end{aligned} \tag{3.25}$$

and through simple algebraic steps:

$$\det^2(\mathbb{I}-\lambda\mathbf{D})\mathbf{b}_e^\top\mathbf{b}_e+\lambda^2[\mathbf{d}^\top-\lambda(\widetilde{\mathbf{D}}\mathbf{d})^\top]\mathbf{D}(\mathbf{d}-\lambda\widetilde{\mathbf{D}}\mathbf{d})+ \\ +2\lambda\det(\mathbb{I}-\lambda\mathbf{D})\mathbf{d}^\top(\mathbf{d}-\lambda\widetilde{\mathbf{D}}\mathbf{d})-\det^2(\mathbb{I}-\lambda\mathbf{D})\overline{d}^2=0 \quad (3.26)$$

$$\det^2(\mathbb{I}-\lambda\mathbf{D})\mathbf{b}_e^\top\mathbf{b}_e+\lambda^2\mathbf{d}^\top\mathbf{D}\mathbf{d}-2\lambda^3\mathbf{d}^\top\mathbf{D}\widetilde{\mathbf{D}}\mathbf{d}+\lambda^4\mathbf{d}^\top\widetilde{\mathbf{D}}^\top\mathbf{D}\widetilde{\mathbf{D}}\mathbf{d}+ \\ +2\lambda\det(\mathbb{I}-\lambda\mathbf{D})\mathbf{d}^\top\mathbf{d}-2\lambda^2\det(\mathbb{I}-\lambda\mathbf{D})\mathbf{d}^\top\widetilde{\mathbf{D}}\mathbf{d}-\det^2(\mathbb{I}-\lambda\mathbf{D})\overline{d}^2=0. \quad (3.27)$$

Similarly to the previous section, Eq. 3.27 can be solved in closed-form for the multiplier λ and the optimal impulse is easily computed by means of Eq. 3.22 using the resulting value of λ.

3.2 Optimal tangential impulsive manoeuvre

As it will be confirmed from the results presented in the following section, the optimum CAM orientation throughout the thrust arc is often not too far from tangential. This suggests deriving the analytical solution of a (sub-optimal) fully tangential manoeuvre, which can be preferred in some operational scenarios.
The problem is solved first for a SMD constraint, including the possibility of setting a PoC threshold, and then for MD enforced value.

Squared Mahalanobis distance constraint

This section describes the tangential optimal impulsive manoeuvre to reach an enforced final PoC (corresponding to a SMD value). The impulse vector, expressed in LVLH r.f., is written as:

$$\Delta\mathbf{v}=\|\Delta\mathbf{v}\|\,\mathbf{t}=\Delta v\mathbf{t}, \quad (3.28)$$

where $\mathbf{t}=[0,1,0]^\top$ is the unit vector in the tangential direction. The performance index of the optimal control problem is:

$$L=\Delta\mathbf{v}^\top\Delta\mathbf{v}=\Delta v^2, \quad (3.29)$$

and the problem is subjected to $f(\Delta v)=0$:

$$f(\Delta v)=\mathbf{b}_f^\top\mathbf{C}^{-1}\mathbf{b}_f-\overline{\mathrm{SMD}}. \quad (3.30)$$

Given $\mathbf{b}_f = \mathbf{b}_e + \mathbf{M}\Delta v\mathbf{t}$:

$$f(\Delta v) = \mathbf{b}_e^\top \mathbf{C}^{-1}\mathbf{b}_e + \Delta v^2 \mathbf{t}^\top \mathbf{A}\mathbf{t} + 2\Delta v \mathbf{b}_e^\top \mathbf{C}^{-1}\mathbf{M}\mathbf{t} - \overline{\mathrm{SMD}}, \tag{3.31}$$

where $\mathbf{A}$ is defined in Eq. 3.6.
The Hamiltonian is:

$$H = L - \lambda f(\Delta v), \tag{3.32}$$

$$H = \Delta v^2 - \lambda(\mathbf{b}_e^\top \mathbf{C}^{-1}\mathbf{b}_e + \Delta v^2 \mathbf{t}^\top \mathbf{A}\mathbf{t} + 2\Delta v \mathbf{b}_e^\top \mathbf{C}^{-1}\mathbf{M}\mathbf{t} - \overline{\mathrm{SMD}}). \tag{3.33}$$

Solving the system:

$$\begin{cases} \dfrac{\partial H}{\partial \Delta v} = 0 \\ \\ \dfrac{\partial H}{\partial \lambda} = 0 \end{cases} \quad \begin{cases} \cancel{2}\Delta v - \lambda(\cancel{2}\Delta v \mathbf{t}^\top \mathbf{A}\mathbf{t} + \cancel{2}\mathbf{b}_e^\top \mathbf{C}^{-1}\mathbf{M}\mathbf{t}) = 0 \\ \\ \mathbf{b}_e^\top \mathbf{C}^{-1}\mathbf{b}_e + \Delta v^2 \mathbf{t}^\top \mathbf{A}\mathbf{t} + 2\Delta v \mathbf{b}_e^\top \mathbf{C}^{-1}\mathbf{M}\mathbf{t} - \overline{\mathrm{SMD}} = 0, \end{cases} \tag{3.34}$$

one can obtain the solution in terms of Δv and λ. The second row of Eq. 3.34 is a quadratic equation in Δv that can be easily solved analytically:

$$\Delta v^2 \mathbf{t}^\top \mathbf{A}\mathbf{t} + 2\Delta v \mathbf{b}_e^\top \mathbf{C}^{-1}\mathbf{M}\mathbf{t} + \mathbf{b}_e^\top \mathbf{C}^{-1}\mathbf{b}_e - \overline{\mathrm{SMD}} = 0 \tag{3.35}$$

$$\Delta v = \frac{-\mathbf{b}_e^\top \mathbf{C}^{-1}\mathbf{M}\mathbf{t} \pm \sqrt{(\mathbf{b}_e^\top \mathbf{C}^{-1}\mathbf{M}\mathbf{t})^2 - \mathbf{t}^\top \mathbf{A}\mathbf{t}(\mathbf{b}_e^\top \mathbf{C}^{-1}\mathbf{b}_e - \overline{\mathrm{SMD}})}}{\mathbf{t}^\top \mathbf{A}\mathbf{t}} \tag{3.36}$$

$$\lambda = (\Delta v \mathbf{t}^\top \mathbf{A}\mathbf{t} + \mathbf{b}_e^\top \mathbf{C}^{-1}\mathbf{M}\mathbf{t})^{-1}\Delta v. \tag{3.37}$$

The impulse vector of the optimal manoeuvre is computed by means of the solution of Eq. 3.36 and Eq. 3.28. The algorithm is analogous to Algorithm 1, substituting Eq. 3.16 with Eqs. 3.36 and 3.28.

Miss distance constraint

Similarly to the manoeuvre without directional constraints, also for the tangential case the formulation can be written starting from a condition on the final miss distance. Given the constraint function $f(\Delta v) = 0$:

$$f(\Delta v) = \mathbf{b}_f^\top \mathbf{b}_f - \overline{d}^2, \tag{3.38}$$

$$f(\Delta v) = \mathbf{b}_e^\top \mathbf{b}_e + \Delta v^2 \mathbf{t}^\top \mathbf{D}\mathbf{t} + 2\Delta v \mathbf{b}_e^\top \mathbf{M}\mathbf{t} - \overline{d}^2, \tag{3.39}$$

where $\mathbf{D}$ is defined in Eq. 3.23, the Hamiltonian reads:

$$H = \Delta v^2 - \lambda(\mathbf{b}_e^\top \mathbf{b}_e + \Delta v^2 \mathbf{t}^\top \mathbf{D}\mathbf{t} + 2\Delta v \mathbf{b}_e^\top \mathbf{M}\mathbf{t} - \overline{d}^2). \tag{3.40}$$

The values of Δv and λ are obtained by solving the system:

$$\begin{cases} \dfrac{\partial H}{\partial \Delta v} = 0 \\ \\ \dfrac{\partial H}{\partial \lambda} = 0 \end{cases} \quad \begin{cases} \Delta v - \lambda(\Delta v \mathbf{t}^\top \mathbf{D}\mathbf{t} + \mathbf{b}_e^\top \mathbf{M}\mathbf{t}) = 0 \\ \\ \mathbf{b}_e^\top \mathbf{b}_e + \Delta v^2 \mathbf{t}^\top \mathbf{D}\mathbf{t} + 2\Delta v \mathbf{b}_e^\top \mathbf{M}\mathbf{t} - \overline{d}^2 = 0 \end{cases} \tag{3.41}$$

where the second row of Eq. 3.41 is a quadratic equation in Δv that is solved analytically:

$$\Delta v^2 \mathbf{t}^\top \mathbf{D}\mathbf{t} + 2\Delta v \mathbf{b}_e^\top \mathbf{M}\mathbf{t} + \mathbf{b}_e^\top \mathbf{b}_e - \overline{d}^2 = 0, \tag{3.42}$$

$$\Delta v = \frac{-\mathbf{b}_e^\top \mathbf{M}\mathbf{t} \pm \sqrt{(\mathbf{b}_e^\top \mathbf{M}\mathbf{t})^2 - \mathbf{t}^\top \mathbf{D}\mathbf{t}(\mathbf{b}_e^\top \mathbf{b}_e - \overline{d}^2)}}{\mathbf{t}^\top \mathbf{D}\mathbf{t}}, \tag{3.43}$$

$$\lambda = (\Delta v \mathbf{t}^\top \mathbf{D}\mathbf{t} + \mathbf{b}_e^\top \mathbf{M}\mathbf{t})^{-1} \Delta v. \tag{3.44}$$

The Δv of the optimal manoeuvre is computed from Eq. 3.43 and Eq. 3.28.

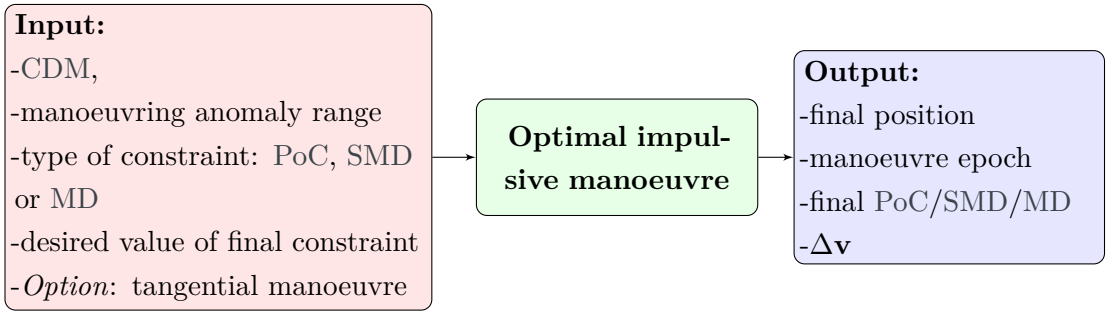

Figure 3.1: Architecture of optimal impulsive CAM tool.

The solutions of all the methods proposed have been used to create a tool sketched in Figure 3.1. Given a possible impact, the function provides the user with the optimal impulsive collision avoidance manoeuvre, in terms of final position, manoeuvre epoch and total cost. The inputs are the Conjunction Data Message (CDM) of the expected collision, the range of true anomaly of the manoeuvring point and the desired final constraint value. The user can choose whether to set the final constraint in terms of collision probability, squared Mahalanobis distance

or miss distance, and optionally the manoeuvre can be optimised enforcing the impulse to thrust only in the tangential direction.

3.3 Test case

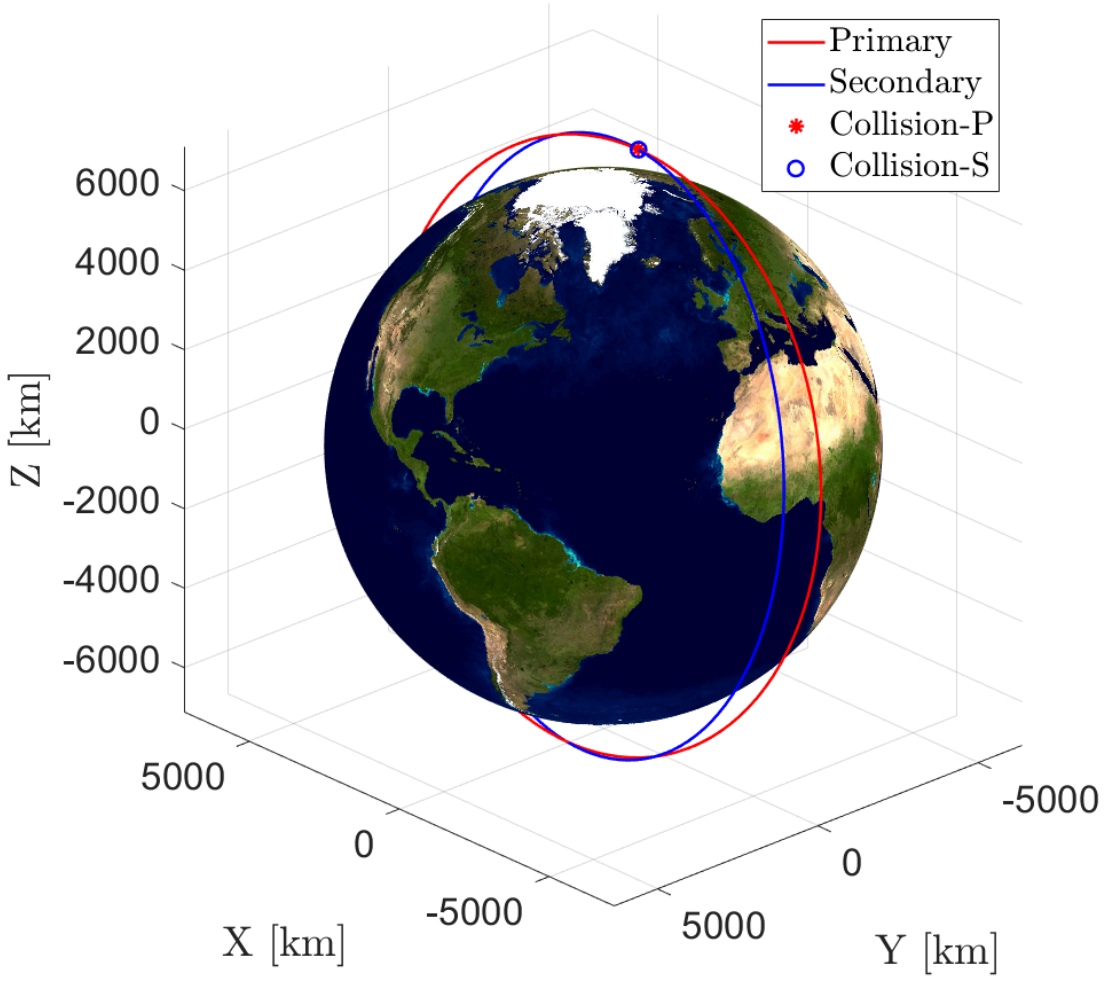

Figure 3.2: Test case collision representation.

The methods presented so far are applied to a test case extracted from [Arm], in which a database of 2,170 conjunction cases are taken from the ESA Collision Avoidance Challenge [Uri20]. A representation of the collision can be found in Figure 3.2. Table 3.1 reports the position and velocity vectors of the primary and secondary spacecraft at conjunction in ECI frame, the collision probability PoC, the squared Mahalanobis distance SMD and the miss distance d. The combined cross-sectional radius of the spacecraft is $s_A = 29.7$ m. The Keplerian elements of

the two orbits are computed and displayed in Table 3.2.

Table 3.1: Test case conjunction data.

$\mathbf{r}_p$[km]	[2.3305, -1103.7, 7105.9]$^\top$
$\mathbf{r}_s$[km]	[2.3335, -1103.7, 7105.9]$^\top$
$\mathbf{v}_p$ [km/s]	[-7.4429, -6.1373e-04, 3.9514e-03]$^\top$
$\mathbf{v}_s$ [km/s]	[7.3537, -1.1428, -0.19825]$^\top$
PoC	1.3604e-01
SMD [km^2]	0.87166
d [km]	0.0432

Table 3.2: Test case orbital elements, in order: semi-major axis, eccentricity, inclination, Right Ascension of the Ascending Node (RAAN), argument of the periapsis, true anomaly.

	a	e	i	Ω	ω	θ
O_p	7186.7 km	0.00064	98.83 °	0 °	289.38 °	160.60 °
O_s	7190.2 km	0.0024	81.28 °	170.93 °	184.41 °	266.99 °

The position covariance matrices of the two satellites, expressed in their respective LVLH r.f., are:

$$\mathbf{C}_p = \begin{bmatrix} 0.9317 & -2.6234 & 0.2360 \\ -2.6234 & 1778.0 & -0.9331 \\ 0.2360 & -0.9331 & 0.1917 \end{bmatrix} \cdot 10^{-4} \text{ km}^2 \tag{3.45}$$

$$\mathbf{C}_s = \begin{bmatrix} 6.3466 & -19.6229 & 0.7077 \\ -19.6229 & 0.0820 & 11.3982 \\ 0.7077 & 11.3982 & 2.5103 \end{bmatrix} \cdot 10^{-4} \text{ km}^2 \tag{3.46}$$

The corresponding combined covariance matrix in B-plane coordinates is:

$$\mathbf{C} = \begin{bmatrix} 7.21756 & -0.7580 \\ -0.7580 & 51.9201 \end{bmatrix} \cdot 10^{-4} \text{ km}^2 \tag{3.47}$$

In the following section, the methods are compared using a dynamical model which only considers Keplerian motion, as expressed in Eq. 2.95.

All the simulations presented in this dissertation are run on a Dell Inspiron 5593 with a processor 1.50 GHz Intel Core i7, 10th generation and 16 Gb Ram Memory.

3.4 Results

The optimal manoeuvre is computed for each manoeuvring point in a range of 100 equally spaced values of true anomaly starting from 2 orbits before the Time of Closest Approach until the expected impact. The definition of true anomaly is represented in Figure 3.3.

$$\Delta\theta \in [0,\ 2 \cdot 2\pi] \tag{3.48}$$

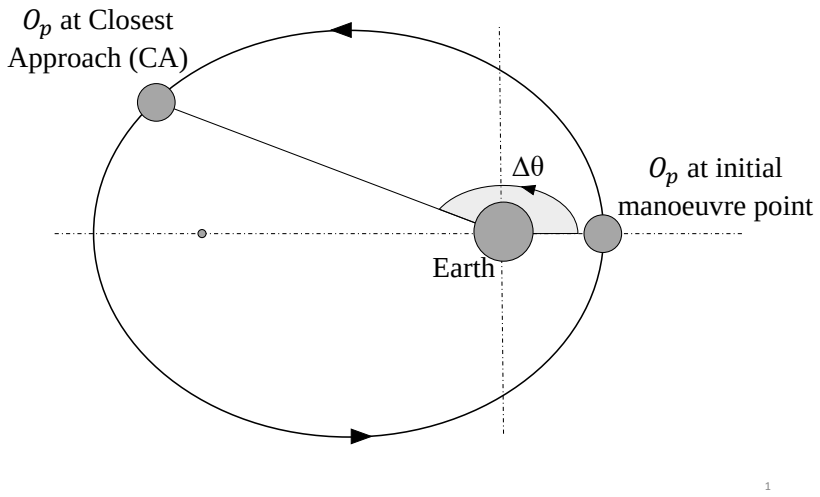

Figure 3.3: True anomaly interval $\Delta\theta$ between the initial manoeuvre point and the closest approach.

Among the manoeuvres starting at each different point, the one with minimum Δv is selected as the optimal, forward propagated until the TCA and the final position in B-plane coordinates is shown in Figure 3.4.
Considering the different kind of constraints, the four categories of manoeuvre are represented with stars of different shapes and colours:

- Optimal manoeuvre with squared Mahalanobis distance final constraint translated into the corresponding Probability of Collision value (Optimal-PoC)

- Tangential manoeuvre with squared Mahalanobis distance/Probability of Collision constraint (Tangential-PoC)
- Optimal manoeuvre with constrained miss distance (Optimal-MD)
- Tangential manoeuvre with constrained miss distance (Tangential-MD)

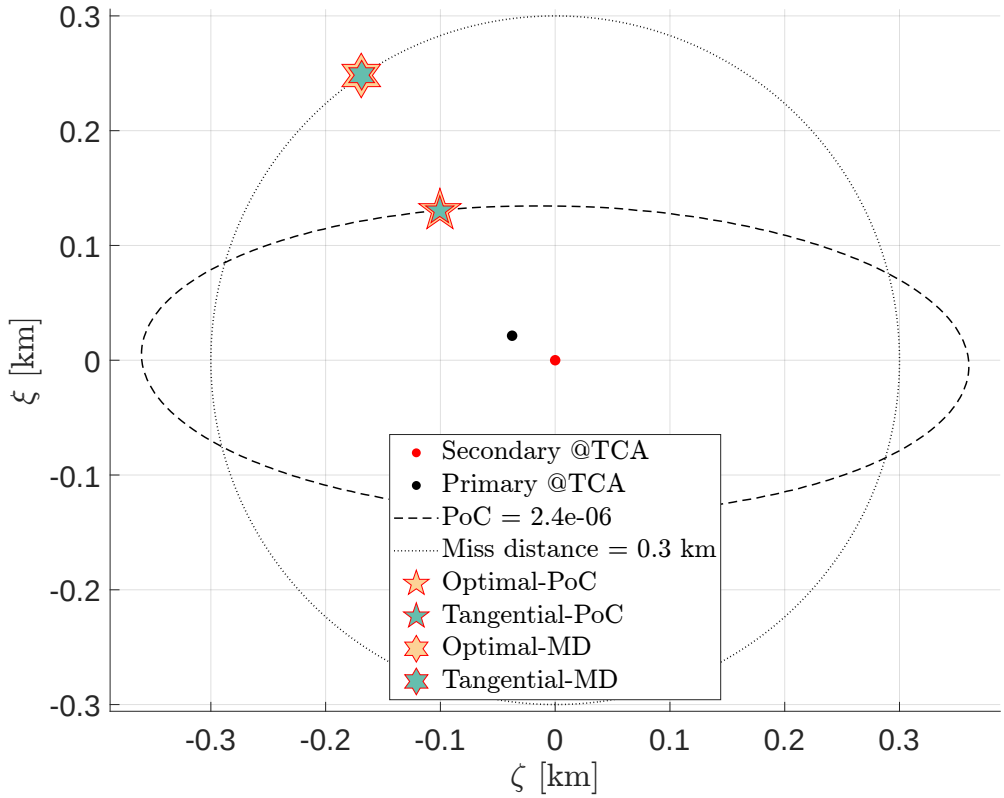

Figure 3.4: Final position in B-plane r.f. reached after impulsive optimal CAMs for different types of constraint.

The enforced value of SMD is translated into the corresponding PoC value by means of Eq. 2.75 and the following thresholds are set:

$$\overline{\text{SMD}} = 25\,\text{km}^2 \quad \rightarrow \quad \overline{\text{PoC}} = 2.4036 \cdot 10^{-6}, \tag{3.49}$$

and

$$\overline{d} = 0.3\,\text{km}. \tag{3.50}$$

The four solutions are shown in B-plane coordinates in Figure 3.4 and in detail in Figure 3.5. The ellipse and the circle are respectively the loci of points with collision probability/miss distance equal to the enforced value, and the stars represent

the final position reached after the manoeuvre at the time of the expected impact. The profile of PoC and MD depending on the manoeuvring point (true anomaly $\Delta\theta$ before TCA) can be found in Figure 3.6 and Figure 3.7.

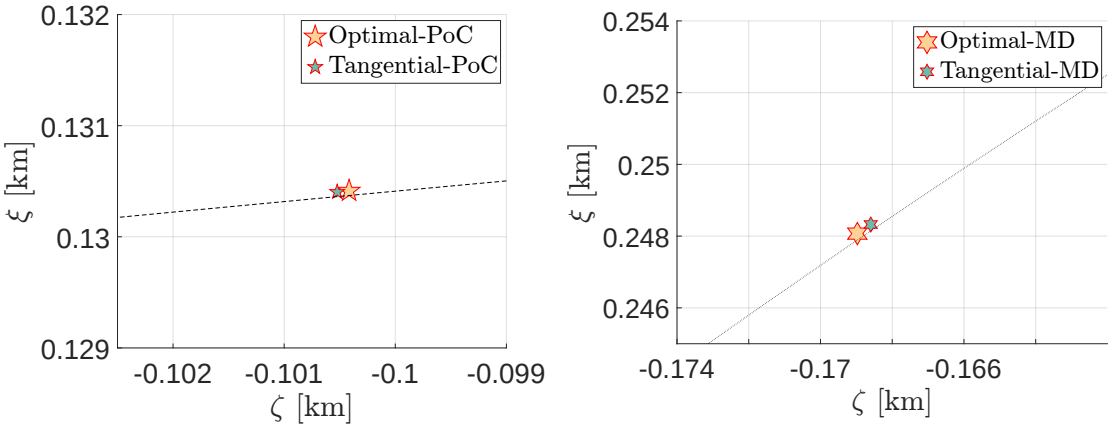

(a) Solutions with constrained PoC.

(b) Solutions with constrained MD.

Figure 3.5: Details of Figure 3.4: enlarged areas of B-plane with final positions reached after optimal impulsive manoeuvres.

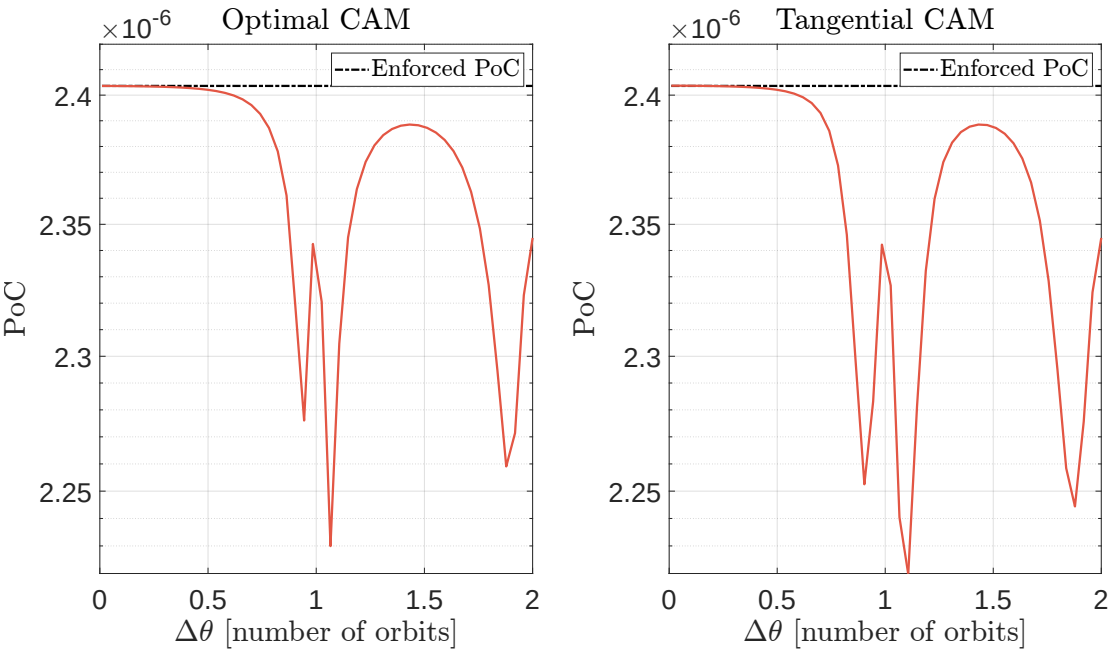

Figure 3.6: Profile of collision probability reached after the optimal impulsive CAM with constrained PoC.

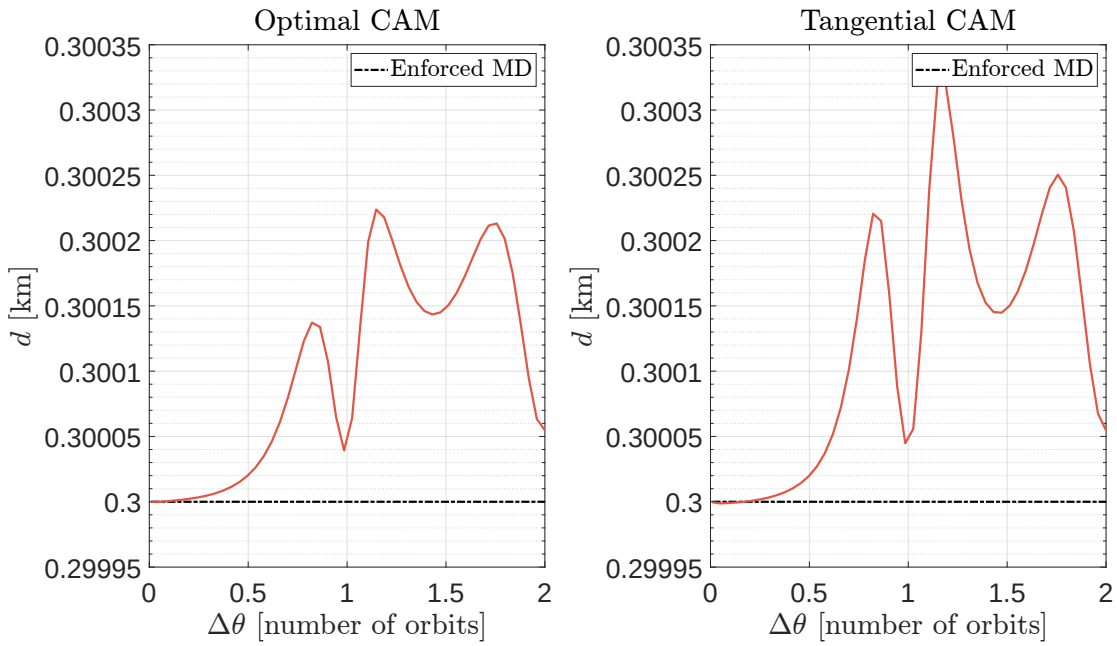

Figure 3.7: Profile of miss distance reached after the optimal impulsive CAM with constrained MD.

The maximum deviations from the enforced value for the four cases are reported in Table 3.3: the orders of magnitude of the errors are much smaller than the enforced values.

Table 3.3: Maximum deviation of PoC/MD from the enforced value.

Optimal PoC	**Tangential PoC**
1.7368e-07	1.8385e-07
Optimal MD	**Tangential MD**
2.2375e-04 km	3.2147e-04 km

All the outputs of the optimal impulsive manoeuvres, with both types of final constraint and considering both the "generic" optimal manoeuvre without directional limits and the purely tangential manoeuvre are summarised in Table 3.4 and Table 3.5. It can be noticed that the optimum $\Delta\mathbf{v}$, even in the case without directional constraints, has a much larger transverse component than the radial and out-of-plane components.

Table 3.4: Impulsive CAM results, constrained PoC.

	Optimal PoC	**Tangential PoC**
$\|\Delta\mathbf{v}\|$ [m/s]	2.83e-02	2.83e-02
$\Delta\mathbf{v}$ [m/s] LVLH r.f.	$\begin{bmatrix} 3.3890e-04 \\ -2.8267e-02 \\ -4.2089e-05 \end{bmatrix}$	$\begin{bmatrix} 0 \\ -2.83e-02 \\ 0 \end{bmatrix}$
$\Delta\theta$ [deg]	544.56	544.56
epoch	2019 JAN 05 20:06:00.053635	2019 JAN 05 20:06:00.053635
$\mathbf{r}_f$ [km] ECI r.f.	$\begin{bmatrix} 1.55 \\ -1.10e+03 \\ 7.11e+03 \end{bmatrix}$	$\begin{bmatrix} 1.54 \\ -1.10e+03 \\ 7.11e+03 \end{bmatrix}$

Table 3.5: Impulsive CAM results, constrained MD.

	Optimal MD	**Tangential MD**
$\|\Delta\mathbf{v}\|$ [m/s]	5.88e-02	5.88e-02
$\Delta\mathbf{v}$ [m/s] LVLH r.f.	$\begin{bmatrix} -1.39e-03 \\ -5.88e-02 \\ -5.58e-04 \end{bmatrix}$	$\begin{bmatrix} 0 \\ -5.88e-02 \\ 0 \end{bmatrix}$
$\Delta\theta$ [deg]	544.5551	544.5551
epoch	2019 JAN 05 20:06:00.053635	2019 JAN 05 20:06:00.053635
$\mathbf{r}_f$ [km] ECI r.f.	$\begin{bmatrix} 6.90e-01 \\ -1.10e+03 \\ 7.11e+03 \end{bmatrix}$	$\begin{bmatrix} 6.945e-01 \\ -1.10e+03 \\ 7.11e+03 \end{bmatrix}$

CHAPTER 4

Low-thrust collision avoidance manoeuvres

This chapter covers the derivation of the methods for low-thrust CAMs, both exploiting the dynamics formulation in Earth-Centered Inertial (ECI) reference frame and in B-plane (BP) coordinates. Compared to the results obtained in literature, this dissertation solves the optimal control problem in a fully analytical way: a significant step towards on-board implementability of low-thrust collision avoidance manoeuvre algorithms. In order to match operational requirements, starting from the analytical solution of the unbounded control problem, a bang-bang structure is achieved by applying a smoothing approach. Moreover, the investigation of the optimal purely tangential manoeuvres is included.

Similarly to the impulsive manoeuvres case, a tool that solves the different types of optimal low-thrust manoeuvres proposed within this chapter has been created, and the architecture is outlined in Figure 4.1. The outputs are the final position

reached after the manoeuvre at the time of the expected impact, the epoch of the initial manoeuvring point, the control acceleration profile, the total cost and the mass variation. The inputs are the CDM of the conjunction, the range of true anomaly for the initial manoeuvring point with respect to the TCA and the desired final constraint value. The optimal control problem can be solved both in ECI coordinates or in BP coordinates. The user can choose whether to set the final constraint in terms of Probability of Collision, Squared Mahalanobis Distance (SMD) distance or Miss Distance (MD). Optionally the manoeuvre can be optimised enforcing the control to thrust only towards the tangential direction, and it is also possible to force the control into a bang-bang structure.

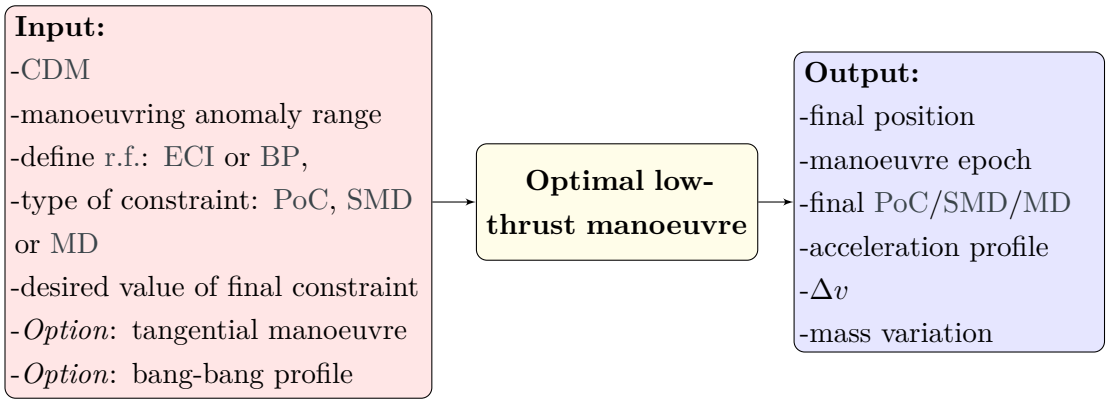

Figure 4.1: Architecture of optimal low-thrust CAM tool.

4.1 Energy-optimal control problem in ECI coordinates

Let us consider the controlled motion of the primary object around Earth, assuming a restricted two-body problem as described in Section 2.7.1.
The state vector concatenates the position and the velocity of the satellite in ECI coordinates $\{x,\ y,\ z\}$:

$$\begin{bmatrix} \mathbf{r} \\ \mathbf{v} \end{bmatrix} = \begin{bmatrix} r_x \\ r_y \\ r_z \\ v_x \\ v_y \\ v_z \end{bmatrix}. \tag{4.1}$$

The control parameter is the acceleration vector:

$$\mathbf{a}_c = \begin{bmatrix} a_{c,x} \\ a_{c,y} \\ a_{c,z} \end{bmatrix}. \tag{4.2}$$

In this formulation, the mass is not included in the state variables as it was presented in Eq. 2.95, since its equation is decoupled from the other. Thus, in order to simplify the equations, it is treated separately:

$$\begin{cases} \dot{\mathbf{r}} = \mathbf{v} \\ \dot{\mathbf{v}} = -\dfrac{\mu}{r^3}\mathbf{r} + \mathbf{a}_c \end{cases} \qquad \text{ICs} : \begin{cases} \mathbf{r}(t_0) = \mathbf{r}_0 \\ \mathbf{v}(t_0) = \mathbf{v}_0 \end{cases} \tag{4.3}$$

$$\dot{m} = -\frac{1}{c_e} \|\mathbf{a}_c\| \, m \qquad \text{IC} : m(t_0) = m_0 \tag{4.4}$$

In minimum-energy formulation, the cost function is defined as:

$$J = \int_{t_0}^{t_f} L \mathrm{d}t, \quad L = \frac{1}{2}\mathbf{a}_c^\top \mathbf{a}_c \tag{4.5}$$

and the terminal function can be written in terms of Squared Mahalanobis Distance (which includes also the Probability of Collision case, using Eq. 2.75) or Miss Distance. These two cases are discussed separately in the following subsections.

Squared Mahalanobis distance constraint

The terminal function is written such that the SMD value corresponding to the final position $\mathbf{r}_f = \mathbf{r}(t_f)$ matches with an enforced value $\overline{\text{SMD}}$:

$$\Psi(\mathbf{x}(t_f), t_f) = \text{SMD}\left(\mathbf{r}_f\right) - \overline{\text{SMD}}. \tag{4.6}$$

By means of Eq. 2.78, and using notation $\mathbf{R}_{2\text{D}} = \mathbf{R}_{b,2\text{D}}$ for simplicity, the SMD is written as function of the position at final time of the manoeuvre $\mathbf{r}_f$:

$$\text{SMD}\left(\mathbf{r}_f\right) = (\mathbf{r}_f - \mathbf{r}_s)^\top \mathbf{R}_{2\text{D}}^\top \mathbf{C}^{-1} \mathbf{R}_{2\text{D}} (\mathbf{r}_f - \mathbf{r}_s). \tag{4.7}$$

The Hamiltonian is:

$$H = \frac{1}{2}\mathbf{a}_c^\top \mathbf{a}_c + \boldsymbol{\lambda}_r^\top \mathbf{v} + \boldsymbol{\lambda}_v^\top \left(-\frac{\mu}{r^3}\mathbf{r} + \mathbf{a}_c\right) \tag{4.8}$$

and the augmented performance index $\overline{J}$ reads:

$$\overline{J} = \nu \left[\mathrm{SMD}\left(\mathbf{r}_f\right) - \overline{\mathrm{SMD}} \right] + \int_{t_0}^{t_f} \left\{ \frac{1}{2} \mathbf{a}_c^\top(t) \mathbf{a}_c(t) + \boldsymbol{\lambda}^\top(t) \left[\dot{\mathbf{x}}(t) - \dot{\mathbf{x}}(t) \right] \right\} \mathrm{d}t. \quad (4.9)$$

The equations of motion for the costate are derived using Eq. 2.93 and the Hamiltonian system associated to the Energy-Optimal control Problem is:

$$\begin{cases} \dot{\mathbf{r}} = \mathbf{v} \\ \dot{\mathbf{v}} = -\dfrac{\mu}{r^3}\mathbf{r} + \mathbf{a}_c \\ \dot{\boldsymbol{\lambda}}_r = \dfrac{\mu}{r^3}\boldsymbol{\lambda}_v - \dfrac{3\mu \mathbf{r} \cdot \boldsymbol{\lambda}_v}{r^5}\mathbf{r} \\ \dot{\boldsymbol{\lambda}}_v = -\boldsymbol{\lambda}_r \end{cases} \quad \begin{cases} \mathbf{r}(t_0) = \mathbf{r}_0 \\ \mathbf{v}(t_0) = \mathbf{v}_0 \\ \boldsymbol{\lambda}_r(t_f) = \nu \dfrac{\partial \mathrm{SMD}(\mathbf{r}_f)}{\partial \mathbf{r}_f} \\ \boldsymbol{\lambda}_v(t_f) = \nu \dfrac{\partial \mathrm{SMD}(\mathbf{v}_f)}{\partial \mathbf{v}_f} \end{cases} \quad (4.10)$$

with the control acceleration law deriving from the Pontryagin's minimum principle which states that the optimal control is the one that minimises the Hamiltonian:

$$\mathbf{a}_c = -\boldsymbol{\lambda}_v. \quad (4.11)$$

The problem can be formulated as a Two-Point Boundary Value Problem (TPBVP), known as Euler-Lagrange equations:

$$\begin{cases} \dot{\mathbf{r}} = \mathbf{v} \\ \dot{\mathbf{v}} = -\dfrac{\mu}{r^3}\mathbf{r} - \boldsymbol{\lambda}_v \\ \dot{\boldsymbol{\lambda}}_r = \dfrac{\mu}{r^3}\boldsymbol{\lambda}_v - \dfrac{3\mu \mathbf{r} \cdot \boldsymbol{\lambda}_v}{r^5}\mathbf{r} \\ \dot{\boldsymbol{\lambda}}_v = -\boldsymbol{\lambda}_v \end{cases} \quad \text{BCs} : \begin{cases} \mathbf{r}(t_0) = \mathbf{r}_0 \\ \mathbf{v}(t_0) = \mathbf{v}_0 \\ \boldsymbol{\lambda}_r(t_f) = \nu 2 \mathbf{R}_{2\mathrm{D}}^\top \mathbf{C}^{-1} \mathbf{R}_{2\mathrm{D}} (\mathbf{r}_f - \mathbf{r}_s) \\ \boldsymbol{\lambda}_v(t_f) = \mathbf{0} \end{cases} \quad (4.12)$$

with a constraint on the final squared Mahalanobis distance:

$$\mathrm{SMD}(\mathbf{r}_f) - \overline{\mathrm{SMD}} = 0. \quad (4.13)$$

Several numerical techniques exist for solving TPBVPs; among them, the most famous is probably the shooting method: the problem is translated in an Initial Value Problem (IVP), where the Initial Conditions (ICs) are found by "shooting" the trajectory until the tolerances on the Boundary Conditions (BCs) are respected. Other methods are finite-difference methods and collocation methods, where the latter are the selected algorithms by MATLAB® to solve TPBVPs.

In this thesis the problem is solved in a completely analytical way avoiding numerical methods, and the procedures is described in detail in the following subsections. The final costates $\boldsymbol{\lambda}_{r0}$, $\boldsymbol{\lambda}_{v0}$ are found exploiting the State Transition Matrix (STM) and the equation of the final constraint, hence the problem becomes an Initial Value Problem (IVP).

$$\begin{cases} \dot{\mathbf{r}} = \mathbf{v} \\ \dot{\mathbf{v}} = -\dfrac{\mu}{r^3}\mathbf{r} - \boldsymbol{\lambda}_v \\ \dot{\boldsymbol{\lambda}}_r = \dfrac{\mu}{r^3}\boldsymbol{\lambda}_v - \dfrac{3\mu \mathbf{r}\cdot\boldsymbol{\lambda}_v}{r^5}\mathbf{r} \\ \dot{\boldsymbol{\lambda}}_v = -\boldsymbol{\lambda}_v \end{cases} \qquad \text{ICs} : \begin{cases} \mathbf{r}(t_0) = \mathbf{r}_0 \\ \mathbf{v}(t_0) = \mathbf{v}_0 \\ \boldsymbol{\lambda}_r(t_0) = \boldsymbol{\lambda}_{r0} \\ \boldsymbol{\lambda}_v(t_0) = \boldsymbol{\lambda}_{v0}. \end{cases} \tag{4.14}$$

Once the IVP has been obtained, it can be solved for the state variables $[\mathbf{r}, \mathbf{v}]$ and the costates $[\boldsymbol{\lambda}_r, \boldsymbol{\lambda}_v]$. The control acceleration profile of the optimal manoeuvre can be simply found by substituting the velocity costate into the control low in Eq. 4.11.

4.1.1 State Transition Matrix

In order to find the initial costates for the IVP formulation, it is necessary to linearise the deviations of the spacecraft from the nominal trajectory using the STM. The nominal ballistic trajectory consists in the natural motion of the satellite around the Earth (see Section 2.7.1).

$$\begin{cases} \dot{\mathbf{r}}_n = \mathbf{v}_n \\ \dot{\mathbf{v}}_n = -\dfrac{\mu}{r^3}\mathbf{r} \\ \dot{\boldsymbol{\lambda}}_{rn} = \mathbf{0} \\ \dot{\boldsymbol{\lambda}}_{vn} = \mathbf{0}. \end{cases} \tag{4.15}$$

Therefore, the state matrix $\mathbf{A}$

$$\mathbf{A}(t) = \left.\frac{\partial \mathbf{f}(\mathbf{x}, t)}{\partial \mathbf{x}}\right|_{\mathbf{x_n}}, \tag{4.16}$$

results to be:

$$\mathbf{A} = \begin{bmatrix} \mathbf{0}_{3\times3} & \mathbb{I}_{3\times3} & \mathbf{0}_{3\times3} & \mathbf{0}_{3\times3} \\ -\mathbf{A}_{34} & \mathbf{0}_{3\times3} & \mathbf{0}_{3\times3} & -\mathbb{I}_{3\times3} \\ \mathbf{0}_{3\times3} & \mathbf{0}_{3\times3} & \mathbf{0}_{3\times3} & \mathbf{A}_{34} \\ \mathbf{0}_{3\times3} & \mathbf{0}_{3\times3} & -\mathbb{I}_{3\times3} & \mathbf{0}_{3\times3} \end{bmatrix}. \tag{4.17}$$

In particular

$$\mathbf{A}_{34} = \frac{\mu}{r_n^3}\mathbb{I}_{3\times3} - 3\frac{\mu}{r_n^5}\begin{bmatrix} \mathbf{r}_n(1)^2 & \mathbf{r}_n(2)\mathbf{r}_n(1) & \mathbf{r}_n(3)\mathbf{r}_n(1) \\ \mathbf{r}_n(1)\mathbf{r}_n(2) & \mathbf{r}_n(2)^2 & \mathbf{r}_n(3)\mathbf{r}_n(2) \\ \mathbf{r}_n(1)\mathbf{r}_n(3) & \mathbf{r}_n(2)\mathbf{r}_n(3) & \mathbf{r}_n(3)^2 \end{bmatrix}, \tag{4.18}$$

where $\mathbf{r}_n(1)$, $\mathbf{r}_n(2)$ and $\mathbf{r}_n(3)$ are the components of the position vector $\mathbf{r}_n$ on the nominal orbit, expressed in ECI r.f.
The State Transition Matrix $\mathbf{\Phi}$ is thus computed by integrating Eq. 2.98:

$$\dot{\mathbf{\Phi}}(t, t_0) = \mathbf{A}(t)\mathbf{\Phi}(t_0, t_0), \qquad \mathbf{\Phi}(t_0, t_0) = \mathbb{I}_{12\times12}, \tag{4.19}$$

and the variations of the initial state are mapped into variations of the final state:

$$\begin{bmatrix} \delta\mathbf{r}_f \\ \delta\mathbf{v}_f \\ \delta\boldsymbol{\lambda}_{rf} \\ \delta\boldsymbol{\lambda}_{vf} \end{bmatrix} = \begin{bmatrix} \mathbf{\Phi}_{11} & \mathbf{\Phi}_{12} & \mathbf{\Phi}_{13} & \mathbf{\Phi}_{14} \\ \mathbf{\Phi}_{21} & \mathbf{\Phi}_{22} & \mathbf{\Phi}_{23} & \mathbf{\Phi}_{24} \\ \mathbf{\Phi}_{31} & \mathbf{\Phi}_{32} & \mathbf{\Phi}_{33} & \mathbf{\Phi}_{34} \\ \mathbf{\Phi}_{41} & \mathbf{\Phi}_{42} & \mathbf{\Phi}_{43} & \mathbf{\Phi}_{44} \end{bmatrix} \begin{bmatrix} \delta\mathbf{r}_0 \\ \delta\mathbf{v}_0 \\ \delta\boldsymbol{\lambda}_{r0} \\ \delta\boldsymbol{\lambda}_{v0} \end{bmatrix}. \tag{4.20}$$

In this approach the initial state is fixed, and the costates are zero on the nominal trajectory, therefore the following relations hold:

$$\mathbf{r}_0 = \mathbf{r}_m \longrightarrow \delta\mathbf{r}_0 = \mathbf{r}_0 - \mathbf{r}_m = \mathbf{0}, \tag{4.21}$$

$$\mathbf{v}_0 = \mathbf{v}_m \longrightarrow \delta\mathbf{v}_0 = \mathbf{v}_0 - \mathbf{v}_m = \mathbf{0}, \tag{4.22}$$

$$\boldsymbol{\lambda}_{rm} = \mathbf{0} \longrightarrow \delta\boldsymbol{\lambda}_{r0} = \boldsymbol{\lambda}_{r0}, \tag{4.23}$$

$$\boldsymbol{\lambda}_{vm} = \mathbf{0} \longrightarrow \delta\boldsymbol{\lambda}_{v0} = \boldsymbol{\lambda}_{v0}, \tag{4.24}$$

$$\delta\mathbf{r}_f = \mathbf{r}_f - \mathbf{r}_p, \tag{4.25}$$

$$\delta\mathbf{v}_f = \mathbf{v}_f - \mathbf{v}_p, \tag{4.26}$$

$$\boldsymbol{\lambda}_{rp} = \mathbf{0} \longrightarrow \delta\boldsymbol{\lambda}_{rf} = \boldsymbol{\lambda}_{rf}, \tag{4.27}$$

$$\boldsymbol{\lambda}_{vp} = \mathbf{0} \longrightarrow \delta\boldsymbol{\lambda}_{vf} = \boldsymbol{\lambda}_{vf}, \tag{4.28}$$

where $\mathbf{r}_m$, $\mathbf{v}_m$, $\boldsymbol{\lambda}_{rm}$, $\boldsymbol{\lambda}_{vm}$ are the state and costate at the initial manoeuvre point, that is at the initial time t_0; $\mathbf{r}_p$, $\mathbf{v}_p$, $\boldsymbol{\lambda}_{rp}$, $\boldsymbol{\lambda}_{vp}$ are the state and costate at the time of closest approach on the nominal trajectory, and $\mathbf{r}_f$, $\mathbf{r}_f$, $\boldsymbol{\lambda}_{rf}$, $\boldsymbol{\lambda}_{vm}$ are the state and costate at the moment of the encounter after the manoeuvre.

4.1.2 Analytical solution

The equations derived from the State Transition Matrix are now used to express the initial costates $\boldsymbol{\lambda}_{r0}$, $\boldsymbol{\lambda}_{v0}$ as a functions of the final position $\mathbf{r}_f$.
Since the final velocity is free, the associated costate is zero: $\delta\boldsymbol{\lambda}_{vf} = \boldsymbol{\lambda}_{vf} = \mathbf{0}$. Thus, from the fourth row of Eq. 4.20, it can be derived:

$$\mathbf{0} = \boldsymbol{\Phi}_{43}\delta\boldsymbol{\lambda}_{r0} + \boldsymbol{\Phi}_{44}\delta\boldsymbol{\lambda}_{v0} \tag{4.29}$$

and from the third row of Eq. 4.20:

$$\begin{aligned}\delta\boldsymbol{\lambda}_{rf} &= \boldsymbol{\Phi}_{33}\delta\boldsymbol{\lambda}_{r0} + \boldsymbol{\Phi}_{34}\delta\boldsymbol{\lambda}_{v0} \\ &= (\boldsymbol{\Phi}_{33} - \boldsymbol{\Phi}_{34}\boldsymbol{\Phi}_{44}^{-1}\boldsymbol{\Phi}_{43})\delta\boldsymbol{\lambda}_{r0} \\ &= \mathbf{B}\delta\boldsymbol{\lambda}_{r0} \\ &\longrightarrow \boldsymbol{\lambda}_{r0} = \mathbf{B}^{-1}\delta\boldsymbol{\lambda}_{rf}.\end{aligned} \tag{4.30}$$

Considering now the first row of Eq. 4.20:

$$\begin{aligned}\delta\mathbf{r}_f &= \boldsymbol{\Phi}_{13}\delta\boldsymbol{\lambda}_{r0} + \boldsymbol{\Phi}_{14}\delta\boldsymbol{\lambda}_{v0} \\ &= (\boldsymbol{\Phi}_{13} - \boldsymbol{\Phi}_{14}\boldsymbol{\Phi}_{44}^{-1}\boldsymbol{\Phi}_{43})\delta\boldsymbol{\lambda}_{r0} \\ &= \mathbf{D}\delta\boldsymbol{\lambda}_{r0} \\ &= \mathbf{D}\mathbf{B}^{-1}\delta\boldsymbol{\lambda}_{rf}\end{aligned} \tag{4.31}$$

$$\mathbf{B} = \boldsymbol{\Phi}_{33} - \boldsymbol{\Phi}_{34}\boldsymbol{\Phi}_{44}^{-1}\boldsymbol{\Phi}_{43} \tag{4.32}$$

$$\mathbf{D} = \boldsymbol{\Phi}_{13} - \boldsymbol{\Phi}_{14}\boldsymbol{\Phi}_{44}^{-1}\boldsymbol{\Phi}_{43}. \tag{4.33}$$

Recalling now that $\delta\boldsymbol{\lambda}_{rf} = \boldsymbol{\lambda}_{rf}$ (Eq. 4.27):

$$\delta\mathbf{r}_f = \mathbf{D}\mathbf{B}^{-1}\boldsymbol{\lambda}_{rf} = \mathbf{D}\mathbf{B}^{-1}\nu\frac{\partial \mathrm{SMD}(\mathbf{r}_f)}{\partial \mathbf{r}_f} \tag{4.34}$$

Hence the variation of the position vector can be written as the product of the multiplier ν and a function $\mathbf{g}$ of the final position $\mathbf{r_f}$:

$$\delta\mathbf{r}_f = \nu\mathbf{g}(\mathbf{r}_f) \tag{4.35}$$

where, computing the derivation of the squared Mahalanobis distance from Eq. 4.7:

$$\mathbf{g}(\mathbf{r}_f) = 2\mathbf{D}\mathbf{B}^{-1}\mathbf{R}_{2\mathrm{D}}^{\top}\mathbf{C}^{-1}\mathbf{R}_{2\mathrm{D}}(\mathbf{r}_f - \mathbf{r}_s). \tag{4.36}$$

A non-linear system in $\mathbf{r}_f$ and ν is obtained form Eq. 4.35 and Eq. 4.13:

$$\begin{cases} \delta\mathbf{r}_f = \mathbf{r}_f - \mathbf{r}_p = \nu\mathbf{g}(\mathbf{r}_f) \\ \mathrm{SMD}(\mathbf{r}_f) = \overline{\mathrm{SMD}}. \end{cases} \tag{4.37}$$

A. Schiavo in [Sch20] solved the system in Eq. 4.37 numerically for ν and $\mathbf{r}_f$, using Levenberg-Marquardt algorithm, implemented in MATLAB® built-in function `fsolve`; in this thesis it is handled analytically, and the steps are here described.

By means of Eq. 4.7, Eq. 4.25 and Eq. 4.36, the non-linear system in Eq. 4.37 can be rewritten as:

$$\begin{cases} \mathbf{r}_f - \mathbf{r}_p = 2\nu\mathbf{D}\mathbf{B}^{-1}\mathbf{R}_{2\mathrm{D}}^{\top}\mathbf{C}^{-1}\mathbf{R}_{2\mathrm{D}}(\mathbf{r}_f - \mathbf{r}_s) \\ (\mathbf{r}_f - \mathbf{r}_s)^{\top}\mathbf{R}_{2\mathrm{D}}^{\top}\mathbf{C}^{-1}\mathbf{R}_{2\mathrm{D}}(\mathbf{r}_f - \mathbf{r}_s) = \overline{\mathrm{SMD}}, \end{cases} \tag{4.38}$$

recalling that $\mathbf{r}_p, \mathbf{r}_s$ are respectively the position of the primary and the secondary object at the Time of Closest Approach (TCA), $\mathbf{C}$ is the 2D combined covariance matrix in BP coordinates and $\mathbf{R}_{2\mathrm{D}}$ is the rotation matrix from ECI r.f. to BP r.f. The first equation of Eq. 4.38 is premultiplied (multiplied to the left) by $\mathbf{R}_{2\mathrm{D}}$ and the second one is rewritten in terms of final position $\mathbf{b}_f$ in B-plane (see Eq. 2.79):

$$\begin{cases} \mathbf{R}_{2\mathrm{D}}(\mathbf{r}_f - \mathbf{r}_p) = 2\nu\mathbf{R}_{2\mathrm{D}}\mathbf{D}\mathbf{B}^{-1}\mathbf{R}_{2\mathrm{D}}^{\top}\mathbf{C}^{-1}\mathbf{R}_{2\mathrm{D}}(\mathbf{r}_f - \mathbf{r}_s) \\ \mathbf{b}_f^{\top}\mathbf{C}^{-1}\mathbf{b}_f = \overline{\mathrm{SMD}}. \end{cases} \tag{4.39}$$

Focusing on the first equation of Eq. 4.39, recalling that a generic position $\mathbf{b}$ in BP coordinates can be written as $\mathbf{b} = \mathbf{R}_{2\mathrm{D}}(\mathbf{r} - \mathbf{r}_s)$:

$$\mathbf{R}_{2\mathrm{D}}(\mathbf{r}_f - \mathbf{r}_s - \mathbf{r}_p + \mathbf{r}_s) = 2\nu\mathbf{R}_{2\mathrm{D}}\mathbf{D}\mathbf{B}^{-1}\mathbf{R}_{2\mathrm{D}}^{\top}\mathbf{C}^{-1}\mathbf{R}_{2\mathrm{D}}(\mathbf{r}_f - \mathbf{r}_s) \tag{4.40}$$

$$\mathbf{b}_f - \mathbf{b}_p = 2\nu\mathbf{R}_{2\mathrm{D}}\mathbf{D}\mathbf{B}^{-1}\mathbf{R}_{2\mathrm{D}}^{\top}\mathbf{C}^{-1}\mathbf{b}_f. \tag{4.41}$$

Let us define the matrix $\mathbf{E} = 2\mathbf{R}_{2D}\mathbf{D}\mathbf{B}^{-1}\mathbf{R}_{2D}^{\top}\mathbf{C}^{-1}$. Eq. 4.41 becomes:

$$\mathbf{b}_f = (\mathbb{I}_{2\times 2} - \nu\mathbf{E})^{-1}\mathbf{b}_p. \tag{4.42}$$

By substituting Eq. 4.42 into the second equation of Eq. 4.39, the latter can be written as a scalar equation with unknown ν. Setting the matrix $\mathbf{Q} = \mathbf{C}^{-1}$, it reads:

$$[(\mathbb{I}_{2\times 2} - \nu\mathbf{E})^{-1}\mathbf{b}_p]^{\top}\mathbf{Q}(\mathbb{I}_{2\times 2} - \nu\mathbf{E})^{-1}\mathbf{b}_p = \overline{\mathrm{SMD}}. \tag{4.43}$$

Since:

$$(\mathbb{I} - \nu\mathbf{E})^{-1} = \frac{1}{\det(\mathbb{I} - \nu\mathbf{E})}[\mathbb{I} - \nu\det\mathbf{E}\cdot(\mathbf{E})^{-1}] \tag{4.44}$$

Equation 4.43 becomes:

$$\frac{1}{\det^2(\mathbb{I} - \nu\mathbf{E})}[(\mathbb{I} - \nu\det\mathbf{E}\cdot\mathbf{E}^{-1})\mathbf{b}_p]^{\top}\mathbf{Q}(\mathbb{I} - \nu\det\mathbf{E}\cdot\mathbf{E}^{-1})\mathbf{b}_p = \overline{\mathrm{SMD}}. \tag{4.45}$$

Let us introduce also the matrix $\widetilde{\mathbf{E}} = \det\mathbf{E}\cdot\mathbf{E}^{-1}$ in order to simplify the notation. Equation 4.45 through simple algebraic steps is written as:

$$[(\mathbb{I} - \nu\widetilde{\mathbf{E}})\mathbf{b}_p]^{\top}\mathbf{Q}(\mathbb{I} - \nu\widetilde{\mathbf{E}})\mathbf{b}_p = \overline{\mathrm{SMD}}\det^2(\mathbb{I} - \nu\mathbf{E}) \tag{4.46}$$

$$[\mathbf{b}_p^{\top} - \nu(\widetilde{\mathbf{E}}\mathbf{b}_p)^{\top}]\mathbf{Q}[\mathbf{b}_p - \nu\widetilde{\mathbf{E}}\mathbf{b}_p] = \overline{\mathrm{SMD}}\det^2(\mathbb{I} - \nu\mathbf{E}) \tag{4.47}$$

$$\mathbf{b}_p^{\top}\mathbf{Q}\mathbf{b}_p - \nu\mathbf{b}_p^{\top}\mathbf{Q}\widetilde{\mathbf{E}}\mathbf{b}_p - \nu(\widetilde{\mathbf{E}}\mathbf{b}_p)^{\top}\mathbf{Q}\mathbf{b}_p + \nu^2(\widetilde{\mathbf{E}}\mathbf{b}_p)^{\top}\mathbf{Q}(\widetilde{\mathbf{E}}\mathbf{b}_p) = \overline{\mathrm{SMD}}\det^2(\mathbb{I} - \nu\mathbf{E}). \tag{4.48}$$

The analytical equation is finally written in the normal polynomial form and can be solved in a closed-form for ν:

$$\nu^2(\widetilde{\mathbf{E}}\mathbf{b}_p)^{\top}\mathbf{Q}(\widetilde{\mathbf{E}}\mathbf{b}_p) - \nu[\mathbf{b}_p^{\top}\mathbf{Q}\widetilde{\mathbf{E}}\mathbf{b}_p + (\widetilde{\mathbf{E}}\mathbf{b}_p)^{\top}\mathbf{Q}\mathbf{b}_p] = \overline{\mathrm{SMD}}\det^2(\mathbb{I} - \nu\mathbf{E}) - \mathbf{b}_p^{\top}\mathbf{Q}\mathbf{b}_p. \tag{4.49}$$

Equation 4.49 has four solutions, since the term with the quadratic determinant contains ν at the fourth degree. The solutions corresponds to the two local minima and two local maxima in terms of equivalent Δv (as it is shown in the results section, Figure 4.8).

The variation of the position reached after the manoeuvre $\delta\mathbf{r}_f$ can be found by

plugging the solution ν into Eq. 4.35. Once $\delta\mathbf{r}_f$ is known, it is finally possible to compute the initial costates $\boldsymbol{\lambda}_{v0}$ and $\boldsymbol{\lambda}_{v0}$ from Eqs. 4.29 and 4.31:

$$\boldsymbol{\lambda}_{r0} = \mathbf{D}^{-1}\delta\mathbf{r}_f, \tag{4.50}$$

$$\boldsymbol{\lambda}_{v0} = -\boldsymbol{\Phi}_{44}^{-1}\boldsymbol{\Phi}_{43}\delta\mathbf{r}_0. \tag{4.51}$$

The IVP in Eq. 4.14, given all the initial conditions, can now be integrated. The whole method presented so far is summarised in Algorithm 2.

Algorithm 2 EOP-ECI

Input: CDM, $\overline{\text{SMD}}$, $\Delta\theta$_range
Output (for each $\Delta\theta$): $\mathbf{r}_f$, SMD, PoC, $\mathbf{a}_c$, $\Delta\mathbf{v}$, Δm
for i = 1 : *size*($\Delta\theta$_range) **do**
    $\Delta\theta = \Delta\theta\_\text{range}(i)$
    $\theta_m = \theta_{\text{TCA}} - \Delta\theta$
    T interval of time corresponding to $\Delta\theta$
    tspan_backward = [T 0]
    tspan_forward = [0 T]
    backard propagation:
    $[\mathbf{r}_0, \mathbf{v}_0] = \textit{keplerian\_propagator}([\mathbf{r}_{\text{TCA}}, \mathbf{v}_{\text{TCA}}]$, tspan_backward)
    compute STM:
    starting from $\mathbf{x}_0$ and propagating for tspan_forward
    solve the non-linear system: (Eq. 4.37) for $\mathbf{r}_{f,es}$ and ν
    compute $\boldsymbol{\lambda}_{r0}, \boldsymbol{\lambda}_{v0}$ using $\mathbf{r}_{f,es}$ and Φ (Eqs. 4.50, 4.51)
    controlled forward propagation:
    $[\mathbf{r}_f, \mathbf{v}_f, \boldsymbol{\lambda}_{rf}, \boldsymbol{\lambda}_{vf}, m_f] = \textit{control\_propagator}([\mathbf{r}_0, \mathbf{v}_0, \boldsymbol{\lambda}_{r0}, \boldsymbol{\lambda}_{v0}, m_0]$, tspan_forward)
    $\Delta\mathbf{r} = \mathbf{r}_f - \mathbf{r}_s$
    SMD = *squared_mahalanobis_distance*($\Delta\mathbf{r}$, CDM)
    PoC = *poc_chan*($\Delta\mathbf{r}$, CDM)
    $\Delta m = m_f - m_0$
end for

Miss distance constraint

The EOP can be reformulated by constraining the final Miss Distance (MD) instead of the final PoC/SMD. Remember that the miss distance d can be written as: $d = \sqrt{\xi_e^2 + \zeta_e^2} = \|\mathbf{b}_f\| = \|\mathbf{R}_{2\text{D}}(\mathbf{r}_f - \mathbf{r}_s)\|$.

The non-linear system in Eq. 4.37 becomes:

$$\begin{cases} \delta \mathbf{r}_f = 2\nu \mathbf{D}\mathbf{B}^{-1}\mathbf{R}_{2\mathrm{D}}^{\top}\mathbf{C}^{-1}\mathbf{R}_{2\mathrm{D}}(\mathbf{r}_f - \mathbf{r}_s) \\ d(\mathbf{r}_f) = \overline{d}, \end{cases} \tag{4.52}$$

$$\begin{cases} \mathbf{R}_{2\mathrm{D}}(\mathbf{r}_f - \mathbf{r}_p) = 2\nu \mathbf{R}_{2\mathrm{D}}\mathbf{D}\mathbf{B}^{-1}\mathbf{R}_{2\mathrm{D}}^{\top}\mathbf{C}^{-1}\mathbf{R}_{2\mathrm{D}}(\mathbf{r}_f - \mathbf{r}_s) \\ \|\mathbf{R}_{2\mathrm{D}}(\mathbf{r}_f - \mathbf{r}_s)\| = \overline{d}. \end{cases} \tag{4.53}$$

One can apply the same procedure of the previous paragraph (Eqs. 4.40 - 4.42), and the first equation of Eq. 4.53 reads:

$$\mathbf{b}_f = (\mathbb{I}_{2\times 2} - \nu\mathbf{E})^{-1}\mathbf{b}_p. \tag{4.54}$$

The second equation of Eq. 4.53 becomes:

$$\left\|(\mathbb{I} - \nu\mathbf{E})^{-1}\mathbf{b}_p\right\| = \overline{d}, \tag{4.55}$$

and similarly to Eqs. 4.44 - 4.46:

$$\left\|\frac{1}{\det(\mathbb{I} - \nu\mathbf{E})}(\mathbb{I} - \nu\widetilde{\mathbf{E}})\mathbf{b}_p\right\| = \overline{d} \tag{4.56}$$

$$\nu^2(\widetilde{\mathbf{E}}\mathbf{b}_p)^{\top}(\widetilde{\mathbf{E}}\mathbf{b}_p) - \nu\mathbf{b}_p^{\top}(\widetilde{\mathbf{E}}\mathbf{b}_p) - \nu(\widetilde{\mathbf{E}}\mathbf{b}_p)^{\top}\mathbf{b}_p = \det(\mathbb{I} - \nu\mathbf{E})^2\overline{d}^2 - \mathbf{b}_p^{\top}\mathbf{b}_p. \tag{4.57}$$

In analogy to what has been explained for the squared Mahalanobis distance case, Eq. 4.56 is algebraically manipulated and analytically solved for ν and used to find the initial costates and integrate the Initial Value Problem.

4.1.3 Results

In order to illustrate the results of the proposed formulation and assess its accuracy, the same test case of Section 3.3 has been considered. The true anomaly ranges from 0 to 2 orbits before TCA, with 100 discretisation points: $\Delta\theta \in [0,\ 4\pi]$. The enforced value of squared Mahalanobis distance and the corresponding collision probability are:

$$\overline{\mathrm{SMD}} = 25\,\mathrm{km}^2 \quad \rightarrow \quad \overline{\mathrm{PoC}} = 2.4036 \cdot 10^{-6}. \tag{4.58}$$

The method described in Algorithm 2 has been applied, and after the control application the final position for each $\Delta\theta$ is reported in BP r.f. in Figure 4.2.

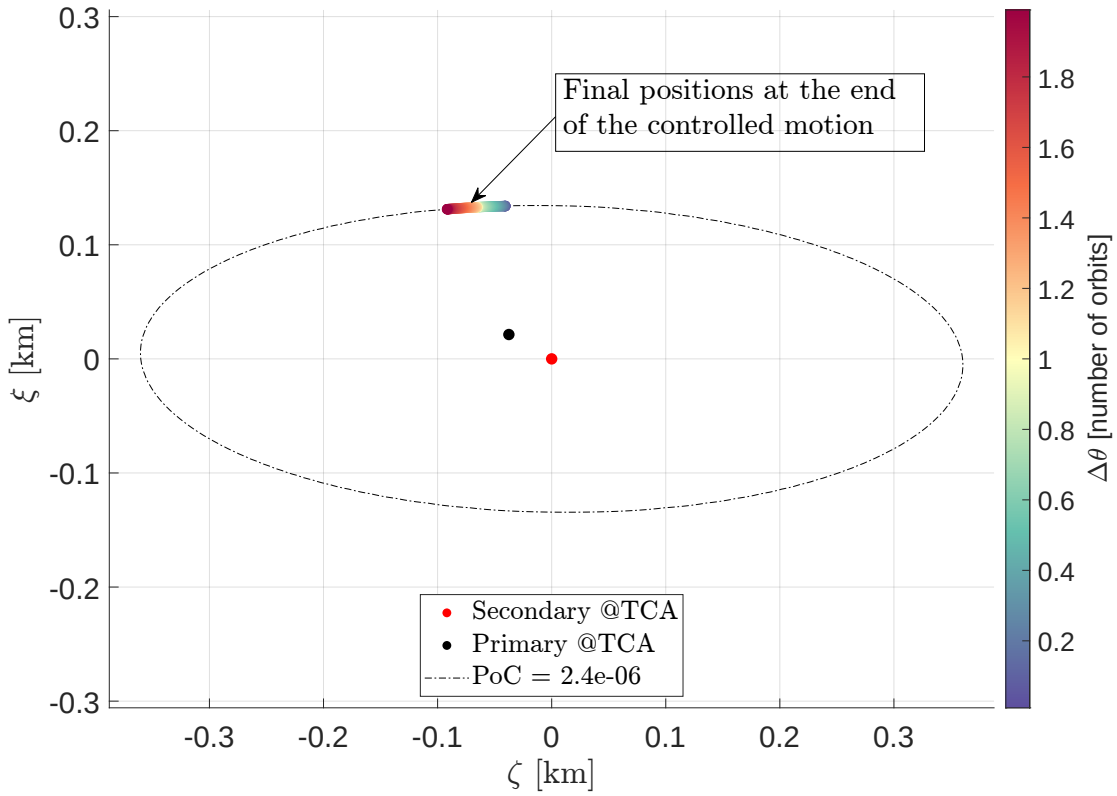

Figure 4.2: Final position in B-plane r.f. reached after the optimal manoeuvre, for 100 initial manoeuvring points from 2 orbits before TCA until the expected impact. EOP with ECI dynamics and constrained SMD.

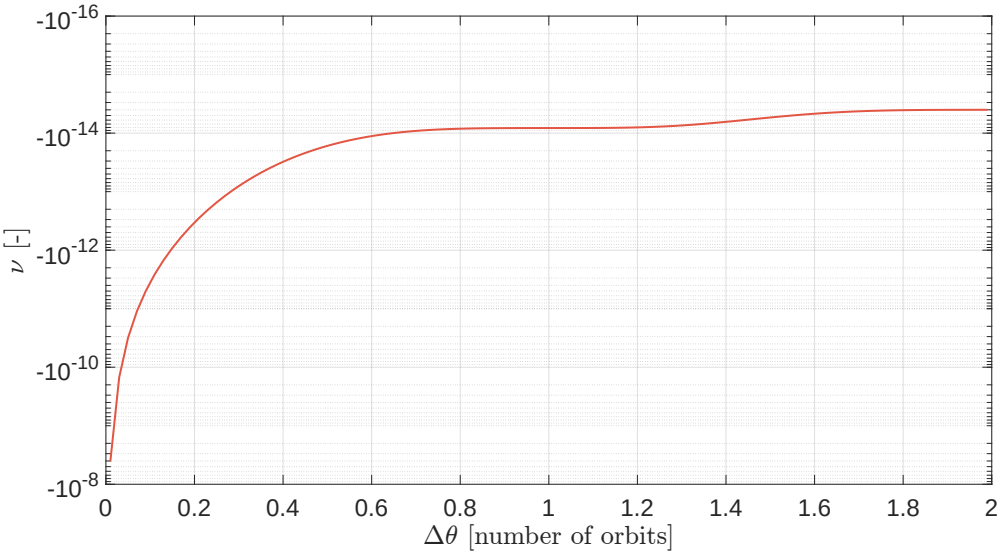

Figure 4.3: Multiplier ν of the EOP with ECI dynamics and constrained SMD.

For completeness the values of the coefficient ν depending on $\Delta\theta$ is shown in Figure 4.3.

Figure 4.4 reports both the "estimated" and "real" collision probability profiles: the former is computed directly after the resolution of the system in Eq. 4.37 with the value of $\mathbf{r}_f$ resulting by Eq. 4.35; the latter is the PoC calculated with the actual final position $\mathbf{r}_f$ obtained after the integration of the manoeuvred dynamics (Eq. 4.14). The estimated behaviour perfectly matches the enforced value, accounting for numerical errors, and the real profile remains close to the threshold without ever exceeding it. The result is absolutely acceptable since at 2 orbits before the CA the maximum deviation is $1.1729 \cdot 10^{-8}$, two orders of magnitude lower than the constraint value.

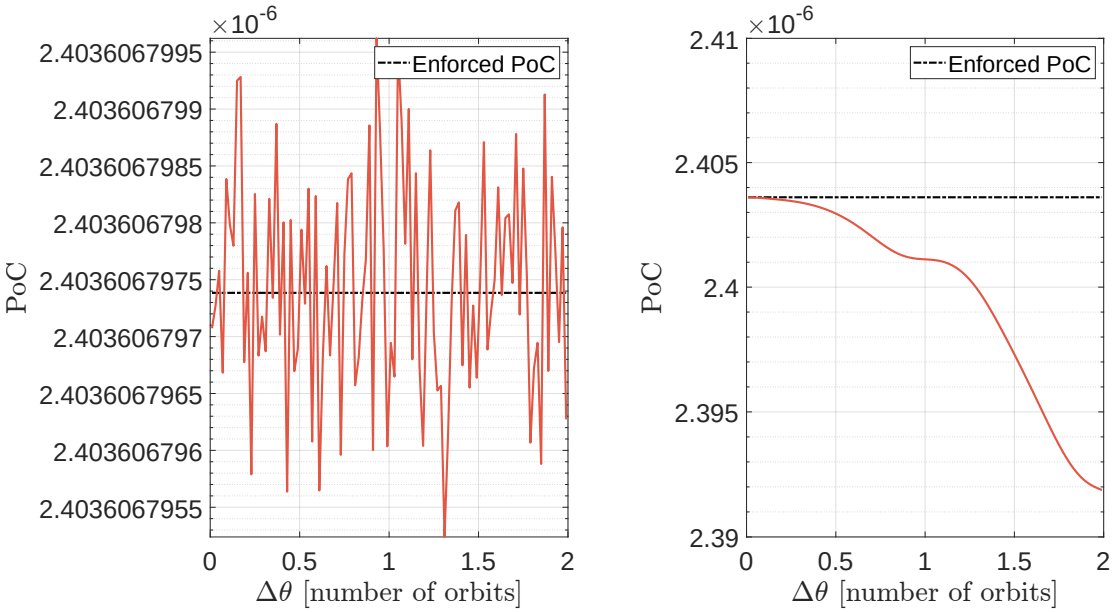

Figure 4.4: Collision probability: estimated value (left) and real profile after the dynamics propagation (right). EOP with ECI dynamics and constrained SMD.

After the resolution of the dynamics of the manoeuvre, the control acceleration profile is found. For each $\Delta\theta$ the equivalent cost in terms of Δv has been calculated by integrating the acceleration profile and the resulting values are reported at the top of Figure 4.5. It can be noticed that the equivalent Δv increases consistently when the manoeuvre is performed close to the expected collision. The plot at the bottom of the same figure displays the development of the maximum control acceleration required, with components in LVLH r.f.. Starting from the furthest

points from the TCA, the transverse component in the most significative, but below a certain value of $\Delta\theta$ close to CA the radial component becomes the largest: it is necessary to manoeuvre the spacecraft as far as possible from the predicted angle of collision.

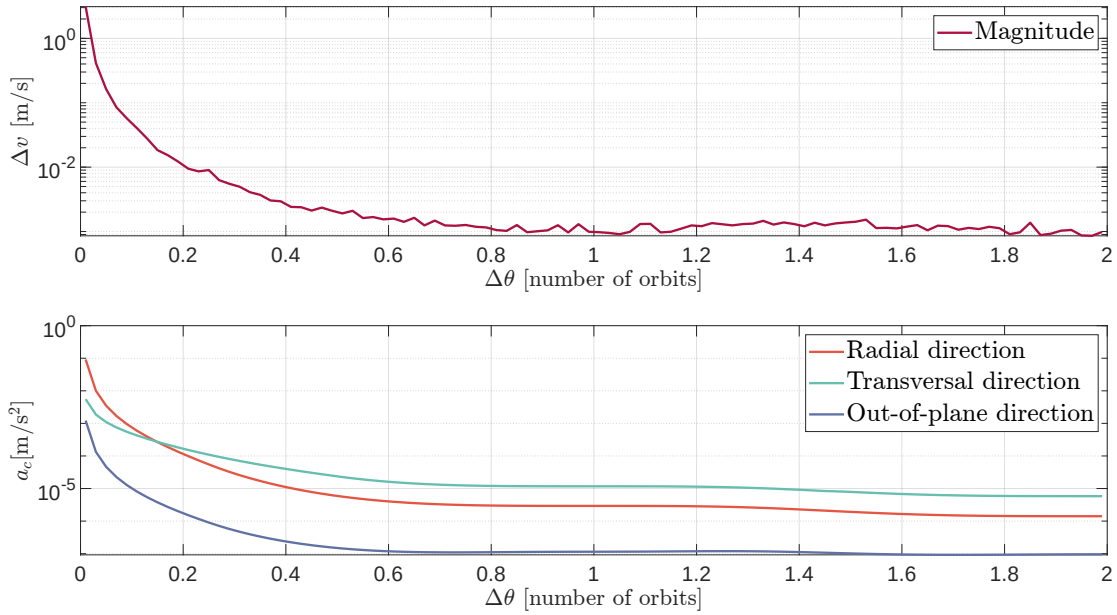

Figure 4.5: Equivalent impulse Δv (top) and maximum control acceleration $\mathbf{a}_c$ (bottom) for each initial manoeuvring point. EOP with ECI dynamics and constrained SMD.

The profile of the control acceleration highly depends on which point is taken to start the manoeuvre (value of $\Delta\theta$). The results considering a manoeuvre starting 1.99 orbits before TCA are shown in Figure 4.6. The manoeuvre is mostly performed in the transverse direction.

The maximum thrust required by the spacecraft and the necessary fuel mass can be seen in Figure 4.7. The initial mass of the satellite is set to $m_0 = 500\,\text{kg}$ and the specif impulse $I_{\text{sp}} = 220\,\text{s}$. As it can be noticed, the nearer to the collision point ($\Delta\theta = 0$) the highest the mass required to match the constraint imposed on the collision probability.

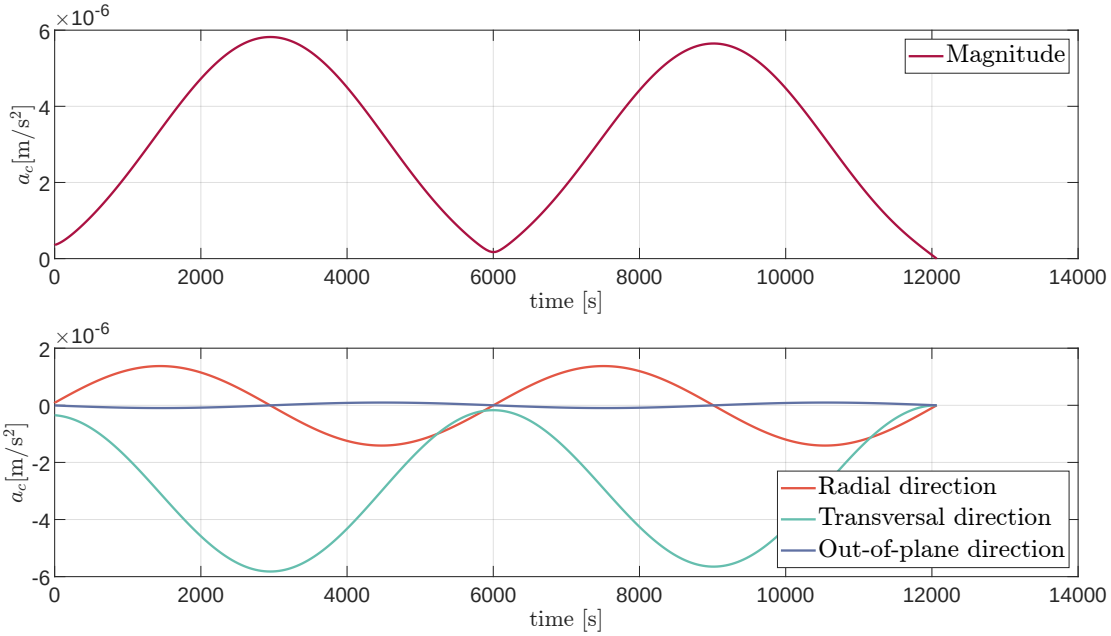

Figure 4.6: Control acceleration profile for a manoeuvre starting 1.99 orbits before TCA. EOP with ECI dynamics and constrained SMD.

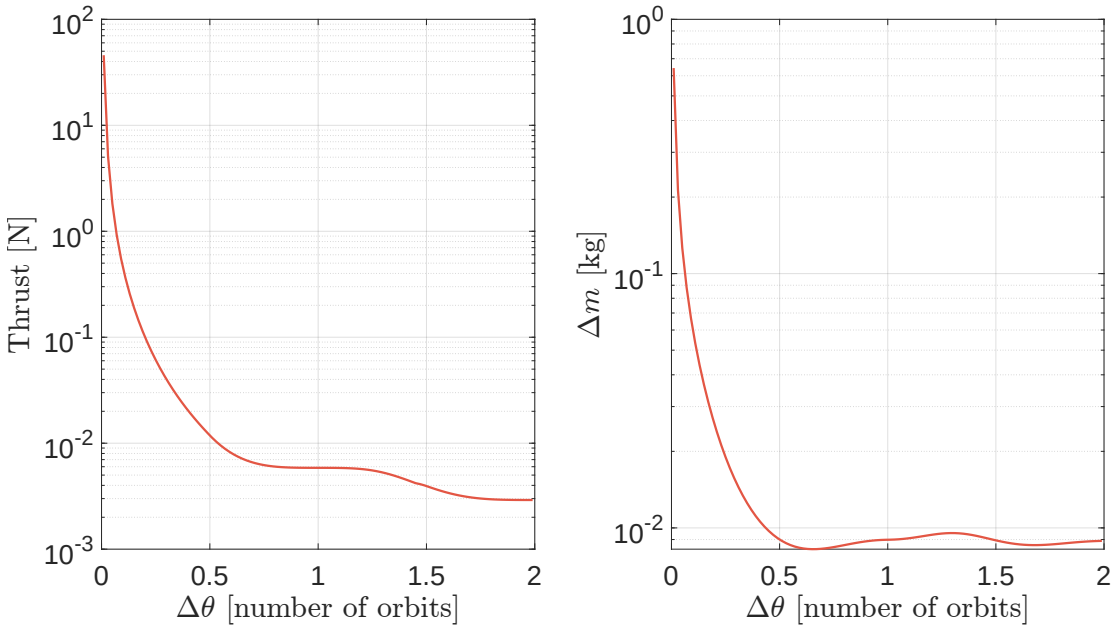

Figure 4.7: Maximum thrust (left) development and mass variation (right) depending on $\Delta\theta$ for EOP with ECI dynamics and constrained SMD.

As previously discussed, Eq. 4.49 has four solutions. A confirmation that those are two local maxima and two local minima in terms of total cost of the manoeuvre

is achieved by the analysis of the objective function's behaviour on each point of the elliptical boundary. This analysis is done by sampling the ellipse with 300 points and solving optimal control problems where the final position is constrained to each specific point. Figure 4.8 shows the results, where the stars indicates the four solutions of the equation. The examined cases have similar objective function structure, with the two minima located at the opposite side of the ellipse and corresponding to thrust mainly aligned with either the tangential or the anti-tangential direction.

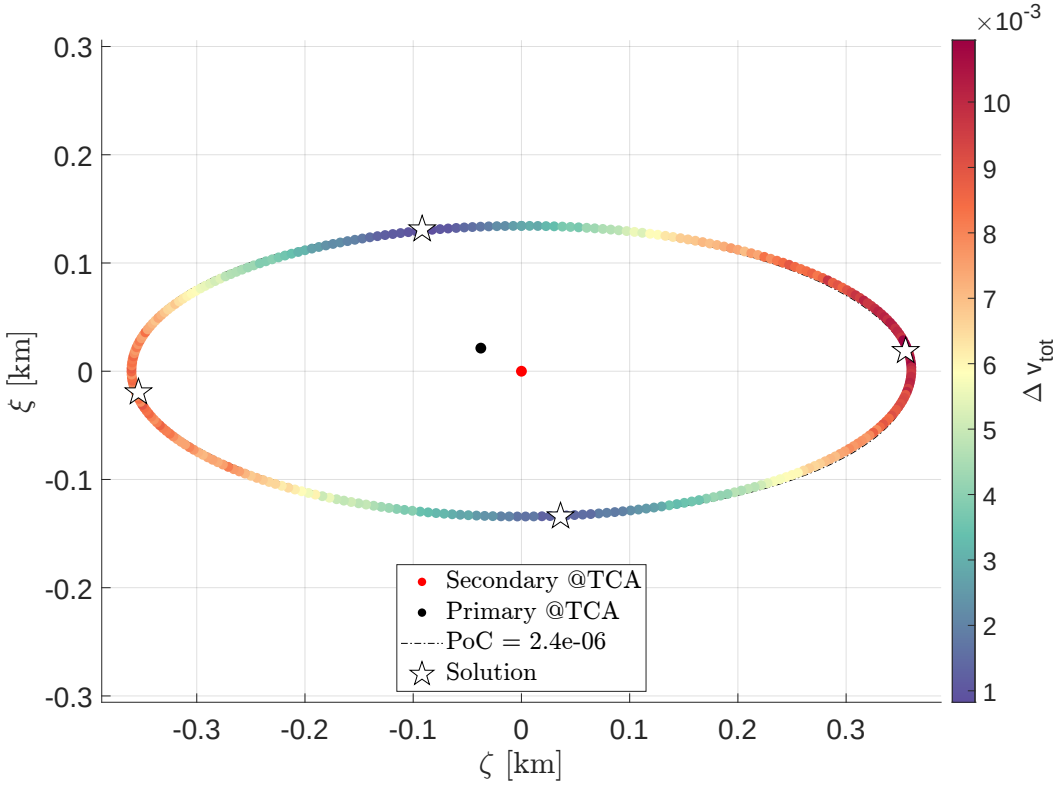

Figure 4.8: Solutions of EOP at 1.99 orbits before TCA compared with the Δv profile on the boundaries of the avoidance region.

Miss distance constraint

Considering miss distance constraint and setting $\overline{d} = 0.3$ km, the final positions in B-plane coordinates after the controlled propagation are reported in Figure 4.9. The miss distance trend, both for the "estimated" values and the "real" miss distance after the forward propagation, are displayed in Figure 4.10.

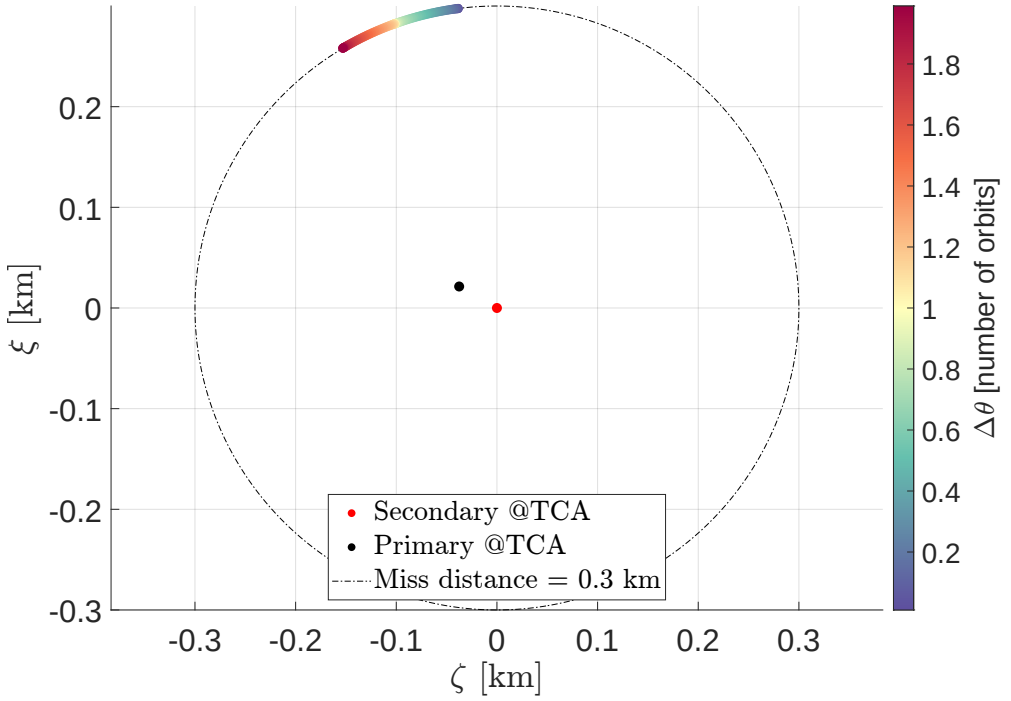

Figure 4.9: Final position in B-plane r.f. reached after the optimal manoeuvre, for 100 manoeuvring points from 2 orbits before TCA until the expected impact. EOP with ECI dynamics and constrained MD.

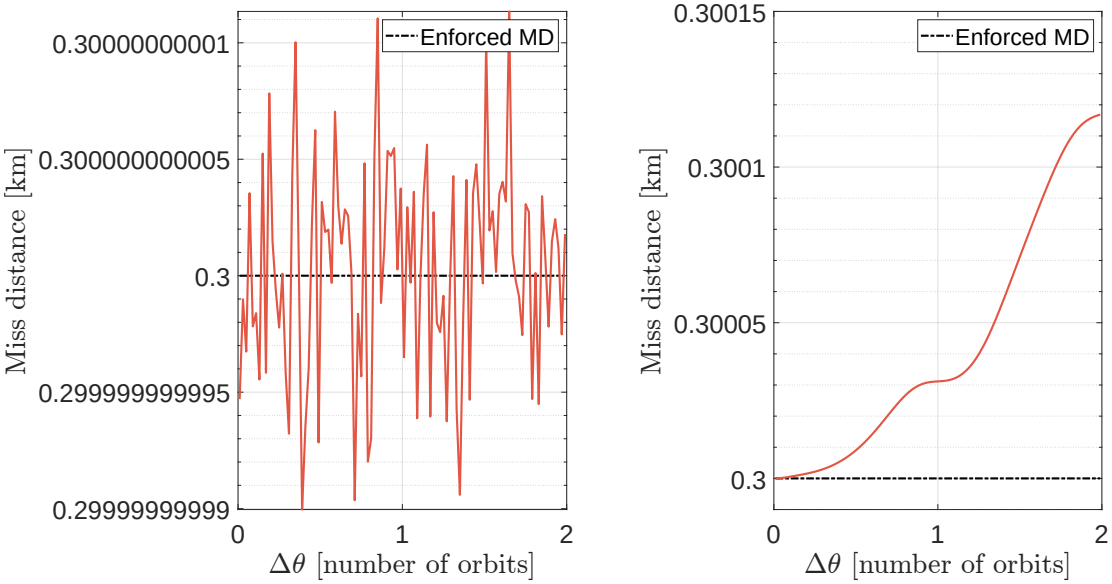

Figure 4.10: Miss distance: estimated value (left) and real profile after the dynamics propagation (right). EOP with ECI dynamics and constrained MD.

Similar to the results in terms of collision probability, the estimated miss distance perfectly matches the enforced value and the real one remains close to the threshold without ever exceeding it, with a maximum deviation of $1.1687 \cdot 10^{-4}$, three orders of magnitude lower than the constraint value.

4.2 Energy-optimal control problem in B-plane coordinates

The EOP formulation can be projected onto B-Plane and the resulting approach simplifies the problem by reducing the dimension of the dynamic system from six to two. The detailed derivation of the conjunction dynamics expressed in B-plane coordinated can be found in Section 2.4. The state vector in B-plane coordinates $\{\xi,\ \zeta\}$ is:

$$\mathbf{b} = \begin{bmatrix} b_\xi \\ b_\zeta \end{bmatrix}.$$

The control parameter is the acceleration, expressed in ECI r.f.:

$$\mathbf{a}_c = \begin{bmatrix} a_{c,x} \\ a_{c,y} \\ a_{c,z} \end{bmatrix}. \tag{4.59}$$

The dynamic system can be written as:

$$\begin{cases} \dot{\mathbf{b}} = \mathbf{M}\mathbf{a}_c \\ \text{IC} : \mathbf{b}(t_0) = \mathbf{b}_0. \end{cases} \tag{4.60}$$

recall the definition of the matrix $\mathbf{M}$ as the product of the three matrices that describe the rotation, kinematics and dynamics from ECI r.f. to the B-plane:

$$\mathbf{M}(t) = \mathbf{RKD}(t). \tag{4.61}$$

The performance index is:

$$L = \frac{1}{2}\mathbf{a}_c^\top \mathbf{a}_c, \tag{4.62}$$

and as in Cartesian coordinates, the terminal function can be written in terms of Squared Mahalanobis Distance (which includes also the Probability of Collision case) or Miss Distance.

Squared Mahalanobis distance constraint

The problem is constrained such that the final SMD value matches with an enforced value $\overline{\text{SMD}}$. Thus the terminal function can be written as:

$$\Psi(\mathbf{x}(t_f), t_f) = \mathbf{b}^\top(t_f)\mathbf{C}^{-1}\mathbf{b}(t_f) - \overline{\text{SMD}}. \tag{4.63}$$

The Hamiltonian is:

$$H = \frac{1}{2}\mathbf{a}_c^\top \mathbf{a}_c + \boldsymbol{\lambda}^\top \mathbf{M}\mathbf{a}_c \tag{4.64}$$

an the augmented cost function reads:

$$\begin{aligned}\overline{J} = \nu \left[\mathbf{b}^\top(t_f)\mathbf{C}^{-1}\mathbf{b}(t_f) - \overline{\text{SMD}}\right] + \\ + \int_{t_0}^{t_f} \left\{\frac{1}{2}\mathbf{a}_c^\top(t)\mathbf{a}_c(t) + \boldsymbol{\lambda}^\top(t)\left[\mathbf{M}(t)\mathbf{a}_c(t) - \dot{\mathbf{b}}(t)\right]\right\} \mathrm{d}t.\end{aligned} \tag{4.65}$$

The Hamiltonian system associated to the EOP results to be:

$$\begin{cases} \dot{\mathbf{b}} = \mathbf{M}\mathbf{a}_c \\ \dot{\boldsymbol{\lambda}} = \mathbf{0} \\ \mathbf{b}(t_0) = \mathbf{b}_0 \\ \boldsymbol{\lambda}(t_f) = \nu 2\mathbf{C}^{-1}\mathbf{b}(t_f) \\ \mathbf{a}_c = -\mathbf{M}^\top \boldsymbol{\lambda}. \end{cases} \tag{4.66}$$

By substituting the resulting definition of the control acceleration $\mathbf{a}_c$ as function of the costate $\boldsymbol{\lambda}$ into the dynamics, the Two-Point Boundary Value Problem can be written as:

$$\begin{cases} \dot{\mathbf{b}} = -\mathbf{M}(t)\mathbf{M}^\top(t)\boldsymbol{\lambda} \\ \dot{\boldsymbol{\lambda}} = \mathbf{0} \end{cases} \qquad \text{BCs} : \begin{cases} \mathbf{b}(t_0) = \mathbf{b}_0 \\ \boldsymbol{\lambda}(t_f) = \nu 2\mathbf{C}^{-1}\mathbf{b}(t_f) \end{cases} \tag{4.67}$$

with the constraint on the final squared Mahalanobis distance

$$\mathbf{b}^\top(t_f)\mathbf{C}^{-1}\mathbf{b}(t_f) - \overline{\text{SMD}} = 0. \tag{4.68}$$

Since the Hamiltonian does not explicitly depend on the $\mathbf{b}$ vector coordinates, $\boldsymbol{\lambda}$ remains constant in time:

$$\boldsymbol{\lambda}(t_0) = \boldsymbol{\lambda}(t) = \nu 2\mathbf{C}^{-1}\mathbf{b}(t_f), \quad \forall t \in (t_0, t_f) \tag{4.69}$$

As explained in Section 4.1, relative to the Cartesian formulation of the problem, also in this case the TPBVP can be translated into a IVP after $\boldsymbol{\lambda}_0$ is known. Equation 4.69 already links $\boldsymbol{\lambda}$ to the final position $\mathbf{b}_f$, thus $\mathbf{b}_f$ needs to be estimated using the STM and the constraint in Eq. 4.68 in order to formulate the initial conditions for an Initial Value Problem:

$$\begin{cases} \dot{\mathbf{b}} = -\mathbf{M}(t)\mathbf{M}^\top(t)\boldsymbol{\lambda} \\ \dot{\boldsymbol{\lambda}} = \mathbf{0} \end{cases} \qquad \text{ICs} : \begin{cases} \mathbf{b}(t_0) = \mathbf{b}_0 \\ \boldsymbol{\lambda}(t) = \boldsymbol{\lambda}_0. \end{cases} \tag{4.70}$$

4.2.1 State Transition Matrix

The natural motion of the satellite around the Earth expressed in B-plane dynamics is expressed by means of Eq. 2.67:

$$\begin{cases} \dot{\mathbf{b}}_n = -\mathbf{M}\mathbf{M}^\top\boldsymbol{\lambda}_n \\ \dot{\boldsymbol{\lambda}}_n = \mathbf{0}. \end{cases} \tag{4.71}$$

The State Transition Matrix is computed by integrating:

$$\dot{\boldsymbol{\Phi}}(t, t_0) = \mathbf{A}(t)\boldsymbol{\Phi}(t_0, t_0), \qquad \boldsymbol{\Phi}(t_0, t_0) = \mathbb{I}_{4\times 4} \tag{4.72}$$

where $\mathbf{A}(t)$ is the state matrix of the linear system

$$\dot{\mathbf{x}}(t) = \mathbf{A}(t)\mathbf{x}(t). \tag{4.73}$$

For this formulation of the problem it can be written as:

$$\mathbf{A} = \begin{bmatrix} \mathbf{0}_{2\times 2} & -\mathbf{M}\mathbf{M}^\top \\ \mathbf{0}_{2\times 2} & \mathbf{0}_{2\times 2} \end{bmatrix}, \quad \text{such that:} \quad \begin{bmatrix} \dot{\mathbf{b}} \\ \dot{\boldsymbol{\lambda}} \end{bmatrix} = \mathbf{A} \begin{bmatrix} \mathbf{b} \\ \boldsymbol{\lambda} \end{bmatrix}. \tag{4.74}$$

Hence the STM turns out to be:

$$\begin{bmatrix} \delta\mathbf{b}_f \\ \delta\boldsymbol{\lambda}_f \end{bmatrix} = \begin{bmatrix} \boldsymbol{\Phi}_{11} & \boldsymbol{\Phi}_{12} \\ \boldsymbol{\Phi}_{21} & \boldsymbol{\Phi}_{22} \end{bmatrix} \begin{bmatrix} \delta\mathbf{b}_0 \\ \delta\boldsymbol{\lambda}_0 \end{bmatrix}. \tag{4.75}$$

Rewriting Eqs. 4.21 - 4.28 and considering that in BP r.f. $\mathbf{b}_m = \mathbf{b}_p = \mathbf{b}_e$, the following conditions can be derived:

$$\mathbf{b}_0 = \mathbf{b}_e \longrightarrow \delta\mathbf{b}_0 = \mathbf{b}_0 - \mathbf{b}_e = \mathbf{0}, \tag{4.76}$$

$$\boldsymbol{\lambda}_e = \mathbf{0} \longrightarrow \delta\boldsymbol{\lambda}_0 = \boldsymbol{\lambda}_0, \tag{4.77}$$

$$\delta\mathbf{b}_f = \mathbf{b}_f - \mathbf{b}_e, \tag{4.78}$$

$$\boldsymbol{\lambda}_e = \mathbf{0} \longrightarrow \delta\boldsymbol{\lambda}_f = \boldsymbol{\lambda}_f. \tag{4.79}$$

4.2.2 Analytical solution

The equations derived from the State Transition Matrix are now used to find another expression to link the initial costate $\boldsymbol{\lambda}_0$ to the final position $\mathbf{b}_f$. From the first row of Eq. 4.75, it can be derived:

$$\delta\mathbf{b}_f = \boldsymbol{\Phi}_{12}\delta\boldsymbol{\lambda}_0 = \boldsymbol{\Phi}_{12}\boldsymbol{\lambda}_0 \tag{4.80}$$

and from Eq. 4.69:

$$\boldsymbol{\lambda}_0 = \nu 2\mathbf{C}^{-1}\mathbf{b}_f \tag{4.81}$$

Hence Eq. 4.80 can be rewritten as:

$$\delta\mathbf{b}_f = \nu\boldsymbol{\Phi}_{12}2\mathbf{C}^{-1}\mathbf{b}_f, \tag{4.82}$$

and exploiting the constraint on the squared Mahalanobis distance value (Eq. 4.68), the non-linear system in ν and $\mathbf{r}_f$ is obtained:

$$\begin{cases} \delta\mathbf{b}_f = \nu\boldsymbol{\Phi}_{12}2\mathbf{C}^{-1}\mathbf{b}_f \\ \mathrm{SMD}(\mathbf{b}_f) = \overline{\mathrm{SMD}} \end{cases} \qquad \begin{cases} \mathbf{b}_f - \mathbf{b}_p = \nu\boldsymbol{\Phi}_{12}2\mathbf{C}^{-1}\mathbf{b}_f \\ \mathbf{b}_f^\top\mathbf{C}^{-1}\mathbf{b}_f = \overline{\mathrm{SMD}}. \end{cases} \tag{4.83}$$

Manipulating the first equation of Eq. 4.83

$$\mathbf{b}_f(\mathbb{I}_{2\times 2} - \nu\boldsymbol{\Phi}_{12}2\mathbf{C}^{-1}) = \mathbf{b}_p, \tag{4.84}$$

and plugging the expression for $\mathbf{b}_f$ into the second equation, one obtains:

$$\begin{cases} \mathbf{b}_f = (\mathbb{I} - \nu\boldsymbol{\Phi}_{12}2\mathbf{C}^{-1})^{-1}\mathbf{b}_p \\ [(\mathbb{I} - \nu\boldsymbol{\Phi}_{12}2\mathbf{C}^{-1})^{-1}\mathbf{b}_p]^\top\mathbf{C}^{-1}(\mathbb{I} - \nu\boldsymbol{\Phi}_{12}2\mathbf{C}^{-1})^{-1}\mathbf{b}_p = \overline{\mathrm{SMD}}. \end{cases} \tag{4.85}$$

Let us define $\mathbf{F} = 2\mathbf{\Phi}_{12}\mathbf{C}^{-1}$ in order to simplify the notation and recall the matrix $\mathbf{Q} = \mathbf{C}^{-1}$. The second equation of Eq. 4.85 becomes a scalar equation that can be solved for ν:

$$[(\mathbb{I} - \nu\mathbf{F})^{-1}\mathbf{b}_p]^\top \mathbf{Q}(\mathbb{I} - \nu\mathbf{F})^{-1}\mathbf{b}_p = \overline{\text{SMD}}. \tag{4.86}$$

Since:

$$(\mathbb{I} - \nu\mathbf{F})^{-1} = \frac{1}{\det(\mathbb{I} - \nu\mathbf{F})}[\mathbb{I} - \nu\det\mathbf{F} \cdot (\mathbf{F})^{-1}] \quad \rightarrow \tag{4.87}$$

$$\frac{1}{\det^2(\mathbb{I} - \nu\mathbf{F})}[(\mathbb{I} - \nu\det\mathbf{F} \cdot \mathbf{F}^{-1})\mathbf{b}_p]^\top \mathbf{Q}(\mathbb{I} - \nu\det\mathbf{F} \cdot \mathbf{F}^{-1})\mathbf{b}_p = \overline{\text{SMD}}. \tag{4.88}$$

Introducing also $\widetilde{\mathbf{F}} = \det\mathbf{F} \cdot \mathbf{F}^{-1}$, and manipulating the equation through simple algebraic steps:

$$[(\mathbb{I} - \nu\widetilde{\mathbf{F}})\mathbf{b}_p]^\top \mathbf{Q}(\mathbb{I} - \nu\widetilde{\mathbf{F}})\mathbf{b}_p = \overline{\text{SMD}}\det^2(\mathbb{I} - \nu\mathbf{F}) \tag{4.89}$$

$$[\mathbf{b}_p^\top - \nu(\widetilde{\mathbf{F}}\mathbf{b}_p)^\top]\mathbf{Q}[\mathbf{b}_p - \nu\widetilde{\mathbf{F}}\mathbf{b}_p] = \overline{\text{SMD}}\det^2(\mathbb{I} - \nu\mathbf{F}) \tag{4.90}$$

$$\mathbf{b}_p^\top\mathbf{Q}\mathbf{b}_p - \nu\mathbf{b}_p^\top\mathbf{Q}\widetilde{\mathbf{F}}\mathbf{b}_p - \nu(\widetilde{\mathbf{F}}\mathbf{b}_p)^\top\mathbf{Q}\mathbf{b}_p + \nu^2(\widetilde{\mathbf{F}}\mathbf{b}_p)^\top\mathbf{Q}(\widetilde{\mathbf{F}}\mathbf{b}_p) = \overline{\text{SMD}}\det^2(\mathbb{I} - \nu\mathbf{F}) \tag{4.91}$$

The analytical equation is finally written in the normal polynomial form and can be solved in a closed-form for ν:

$$\nu^2(\widetilde{\mathbf{F}}\mathbf{b}_p)^\top\mathbf{Q}(\widetilde{\mathbf{F}}\mathbf{b}_p) - \nu[\mathbf{b}_p^\top\mathbf{Q}\widetilde{\mathbf{F}}\mathbf{b}_p + (\widetilde{\mathbf{F}}\mathbf{b}_p)^\top\mathbf{Q}\mathbf{b}_p] = \overline{\text{SMD}}\det^2(\mathbb{I} - \nu\mathbf{F}) - \mathbf{b}_p^\top\mathbf{Q}\mathbf{b}_p. \tag{4.92}$$

In analogy of the final formula obtained with Cartesian dynamics, Eq. 4.92 has four solutions corresponding to the two local minima and two local maxima in terms of equivalent Δv.

The variation of the position reached after the manoeuvre in BP r.f. $\mathbf{b}_f$ is found by plugging the solution ν into the first equation of Eq. 4.85. Once $\mathbf{b}_f$ is known, it is possible to compute $\boldsymbol{\lambda}_0$ from Eq. 4.81 and the IVP in Eq. 4.70, given all the initial conditions, can be integrated. The solution method for the EOP exploiting B-plane dynamics is summarised in Algorithm 3.

Algorithm 3 EOP-BP

Input: CDM, $\overline{\text{SMD}}$, $\Delta\theta$_range
Output (for each $\Delta\theta$): $\mathbf{b}_f$, SMD, PoC, $\mathbf{a}_c$, $\Delta\mathbf{v}$, Δm
for i = 1 : *size*($\Delta\theta$_range) **do**
    $\Delta\theta = \Delta\theta$_range($i$)
    $\theta_m = \theta_{\text{TCA}} - \Delta\theta$
    T interval of time corresponding to $\Delta\theta$
    tspan_backward = [T 0]
    tspan_forward = [0 T]
    compute B-plane quantities for dynamics from CDM
    $\mathbf{b}_0 = keplerian\_propagator([\mathbf{b}_{\text{TCA}}$ tspan_backward)
    compute STM:
    starting from $\mathbf{b}_0$ and propagating for tspan_forward
    solve the non-linear system: (Eq. 4.37) for $\mathbf{b}_{f,es}$ and ν
    compute $\boldsymbol{\lambda}_0$ using $\mathbf{b}_{f,es}$ and Φ (Eqs. 4.50, 4.51)
    controlled forward propagation:
    $[\mathbf{b}_f, \boldsymbol{\lambda}_f, m_f] = control\_propagator([\mathbf{b}_0, \boldsymbol{\lambda}_0, m_0]$, tspan_forward)
    SMD = $squared\_mahalanobis\_distance(\mathbf{b}_f, \text{CDM})$
    PoC = $poc\_chan(\Delta\mathbf{r}, \text{CDM})$
    $\Delta m = m_f - m_0$
end for

Miss distance constraint

The EOP in B-plane coordinates can be reformulated by constraining the final Miss Distance (MD) instead of the final PoC/SMD. Recalling the definition of miss distance in BP coordinates $d = \sqrt{\xi_e^2 + \zeta_e^2} = \|\mathbf{b}_f\|$, the non-linear system in Eq. 4.83 becomes:

$$\begin{cases} \delta\mathbf{b}_f = \nu\boldsymbol{\Phi}_{12} 2\mathbf{C}^{-1}\mathbf{b}_f \\ d(\mathbf{b}_f) = \overline{d} \end{cases} \quad \begin{cases} \mathbf{b}_f - \mathbf{b}_p = \nu\boldsymbol{\Phi}_{12} 2\mathbf{C}^{-1}\mathbf{b}_f \\ \|\mathbf{b}_f\| = \overline{d} \end{cases} \tag{4.93}$$

Manipulating the first equation of Eq. 4.93 and plugging $\mathbf{b}_f$ into the second one:

$$\begin{cases} \mathbf{b}_f = (\mathbb{I}_{2\times 2} - \nu\boldsymbol{\Phi}_{12} 2\mathbf{C}^{-1})^{-1}\mathbf{b}_p \\ \|(\mathbb{I}_{2\times 2} - \nu\boldsymbol{\Phi}_{12} 2\mathbf{C}^{-1})^{-1}\mathbf{b}_p\| = \overline{d}. \end{cases} \tag{4.94}$$

and similarly to Eqs. 4.87 - 4.89:

$$\left\| \frac{1}{\det(\mathbb{I} - \nu\mathbf{F})} (\mathbb{I} - \nu\widetilde{\mathbf{F}})\mathbf{b}_p \right\| = \overline{d}. \tag{4.95}$$

In analogy to what has been explained for the squared Mahalanobis distance case, Eq. 4.95 is algebraically manipulated and analytically solved for ν and used to find the initial costate and integrate the Initial Value Problem in Eq. 4.70.

4.2.3 Results

The results relative to the EOP formulation in BP dynamics are here reported. The same test case and the same constraint values of Section 4.1.3 have been considered.

The method described in Algorithm 3 has been applied, and after the control application the final position for each $\Delta\theta \in [0,\ 4\pi]$ is reported in BP r.f. in Figure 4.11. As expected, the results are almost indistinguishable from the ones reached exploiting ECI dynamics (see Figure 4.2). The two solutions with ECI and BP dynamics are shown together on the same enlarged area of the B-plane in Figure 4.12 and a better understanding can be achieved from the comparison of the trends of the final collision probability.

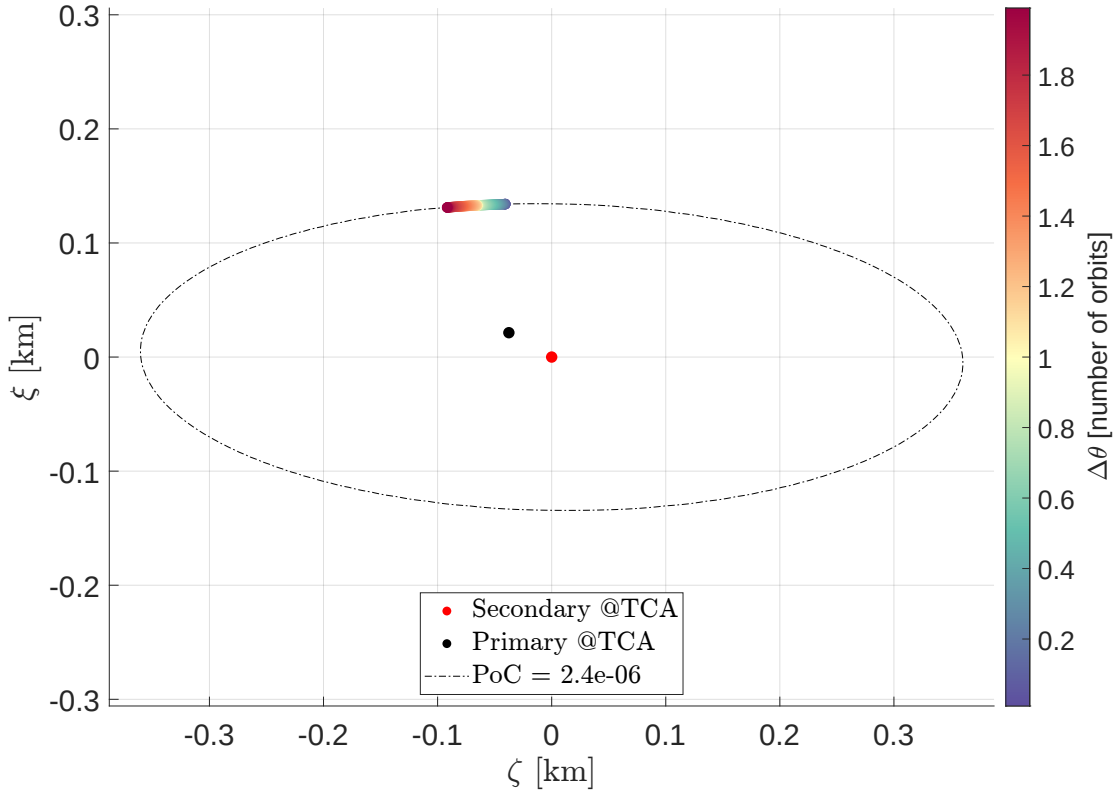

Figure 4.11: Final position in B-plane r.f. reached after the optimal manoeuvre, for 100 initial manoeuvring points from 2 orbits before TCA until the expected impact. EOP with BP dynamics and constrained SMD.

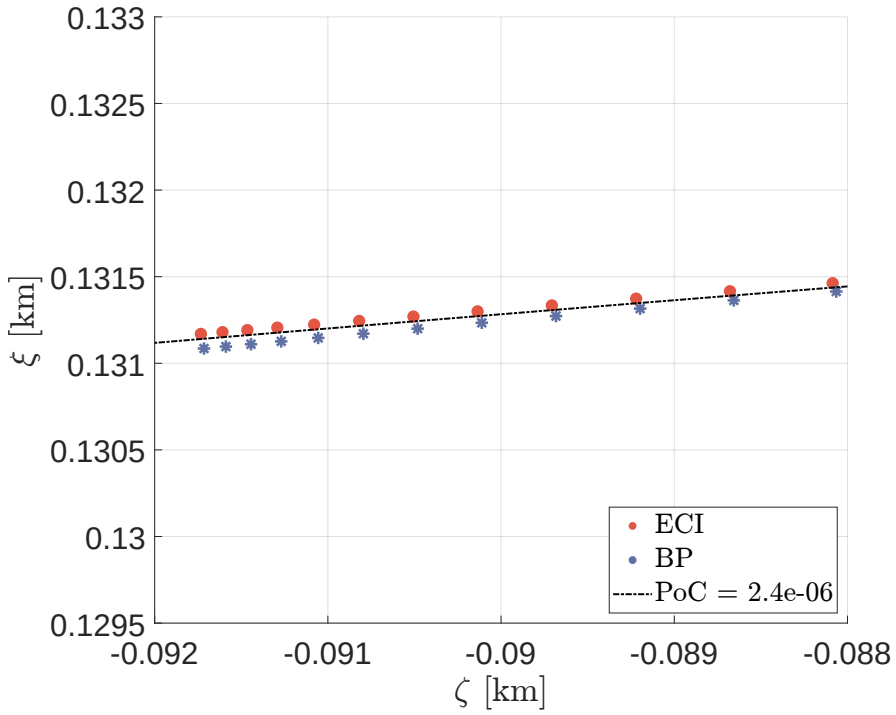

Figure 4.12: Final position in B-plane r.f. reached after the optimal manoeuvre: comparison between EOP in ECI and BP coordinates, constrained SMD (detail of Figure 4.2 and Figure 4.11).

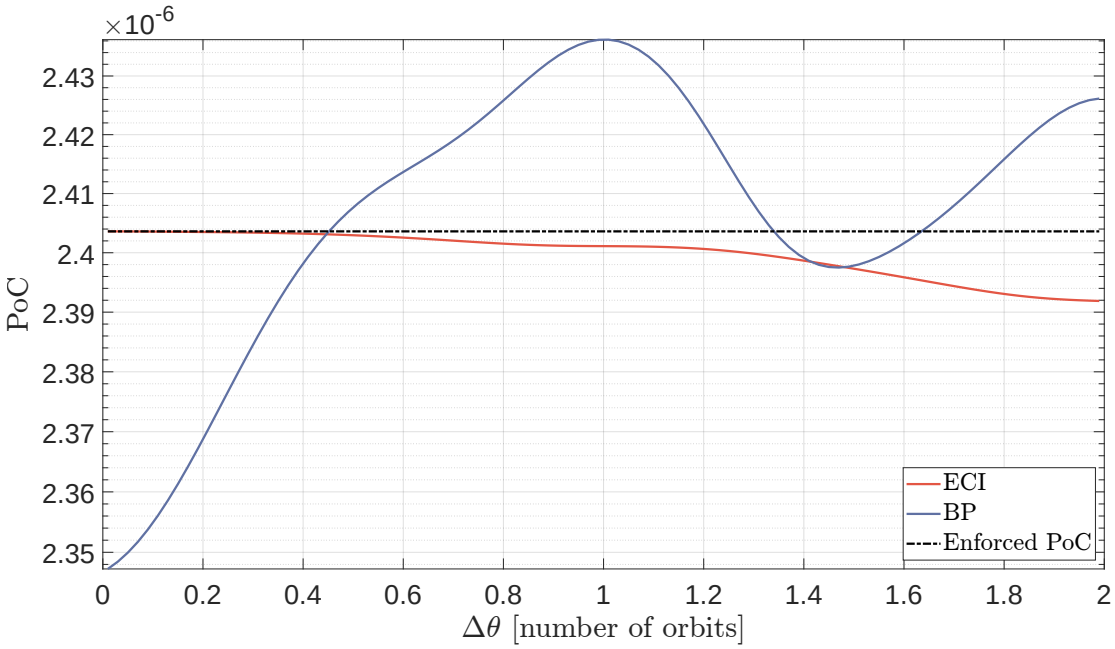

Figure 4.13: Collision probability profile after the dynamics propagation: comparison between EOP in ECI and BP coordinates, constrained SMD.

Figure 4.13 shows the differences between ECI and BP dynamics in terms of final collision probability profile for each true anomaly of the initial manoeuvre point, calculated with the actual final position $\mathbf{r}_f/\mathbf{b}_f$ obtained after the integration of the manoeuvred dynamics. Even though the ECI algorithm is more accurate and it never exceeds the threshold, both of them are close to the enforced value: for the B-plane algorithm the maximum deviation is $5.6354 \cdot 10^{-8}$, still in the same order of magnitude of the error with ECI coordinates, two order lower than the boundary.

Miss distance constraint

The results of the EOP formulation with terminal function expressed in terms of miss distance are shown hereafter. As for the PoC/SMD case, the final position is nearly indistinguishable from the achieved with ECI dynamics formulation, and a portion of B-plane (detail of Figure 4.9) is reported in Figure 4.14.

Figure 4.15 shows the final miss distance trend, computed through ECI and BP

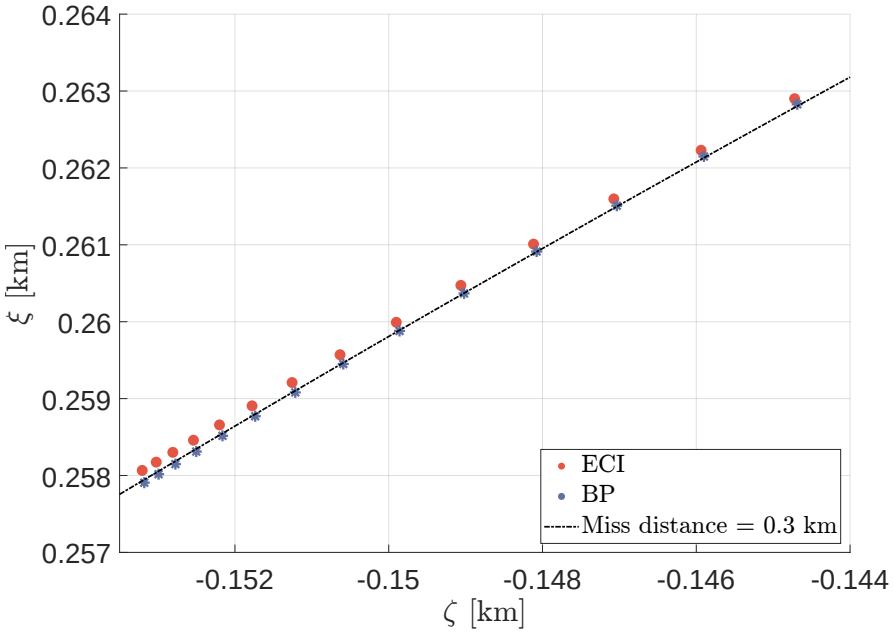

Figure 4.14: Final position in B-plane r.f. reached after the optimal manoeuvre: comparison between EOP in ECI and BP coordinates, constrained MD (detail of Figure 4.9).

algorithm. The maximum deviation in the BP behaviour, $3.3818 \cdot 10^{-4}$ km, is absolutely acceptable compared to the one in ECI r.f. of $1.1687 \cdot 10^{-4}$ km, three order of magnitude lower the imposed value $\overline{d} = 0.3$ km.

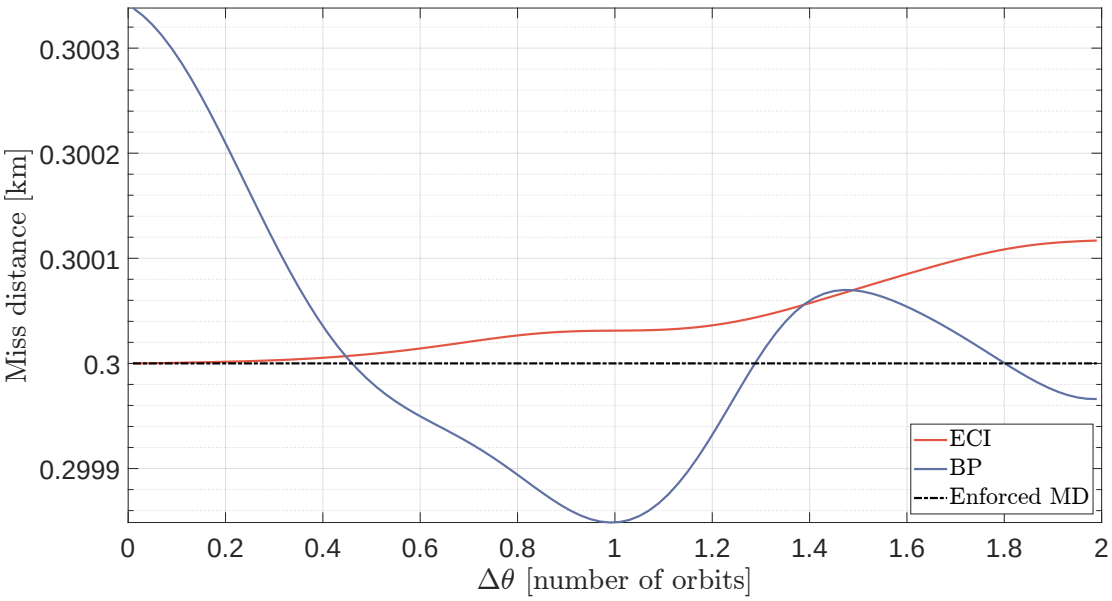

Figure 4.15: Miss distance profile after the dynamics propagation: comparison between EOP in ECI and BP coordinates, constrained MD.

4.3 Scaled control acceleration

It is useful to rewrite the EOP considering a maximum affordable acceleration value for the satellite thrusters. Within such an approach, the values of the velocity costate $\boldsymbol{\lambda}_v$ represent exactly the fraction of $a_{\max}$ that must be applied to perform the manoeuvre.
Let us define the scaled control acceleration with respect to the maximum acceleration, such that:

$$\mathbf{a}_c = a_{\max}\mathbf{a}_{c,s}, \tag{4.96}$$

where $\mathbf{a}_{c,s}$ is the scaled control acceleration vector. Following the optimal control theory described in Section 2.7, the performance index and Hamiltonian read:

$$L = \frac{1}{2}a_{\max}\mathbf{a}_{c,s}^{\top}\mathbf{a}_{c,s}, \tag{4.97}$$

$$H = \frac{1}{2}a_{\max}\mathbf{a}_{c,s}^{\top}\mathbf{a}_{c,s} + \boldsymbol{\lambda}_r^{\top}\mathbf{v} + \boldsymbol{\lambda}_v^{\top}(-\frac{\mu}{r^3}\mathbf{r} + a_{\max}\mathbf{a}_{c,s}), \tag{4.98}$$

The control law, found through the Pontryagin's minimum principle which states that the optimal control is the one that minimise the Hamiltonian, is:

$$\frac{\partial H}{\partial \mathbf{a}_{c,s}} = 0 \quad \rightarrow \quad a_{\max}\mathbf{a}_{c,s} + a_{\max}\boldsymbol{\lambda}_v = 0 \tag{4.99}$$

$$\rightarrow \quad \mathbf{a}_{c,s} = -\boldsymbol{\lambda}_v \tag{4.100}$$

$$\mathbf{a}_c = -a_{\max}\boldsymbol{\lambda}_v. \tag{4.101}$$

Having the modulus of λ_v related to the percentage of thrust with respect to its maximum value (see Eq. 4.101) facilitates the transformation of the continuous profile into the so called "bang-bang" profile that will be introduced in Section 4.4. The Euler-Lagrange equations that describes the problem are:

$$\begin{cases} \dot{\mathbf{r}} = \mathbf{v} \\ \dot{\mathbf{v}} = -\dfrac{\mu}{r^3}\mathbf{r} - a_{\max}\boldsymbol{\lambda}_v \\ \dot{\boldsymbol{\lambda}}_r = \dfrac{\mu}{r^3}\boldsymbol{\lambda}_v - \dfrac{3\mu\mathbf{r}\cdot\boldsymbol{\lambda}_v}{r^5}\mathbf{r} \\ \dot{\boldsymbol{\lambda}}_v = -\boldsymbol{\lambda}_v \end{cases} \qquad \text{BCs}: \begin{cases} \mathbf{r}(t_0) = \mathbf{r}_0 \\ \mathbf{v}(t_0) = \mathbf{v}_0 \\ \boldsymbol{\lambda}_r(t_f) = \nu 2\mathbf{R}_{2\text{D}}^{\top}\mathbf{C}^{-1}\mathbf{R}_{2\text{D}}(\mathbf{r}_f - \mathbf{r}_s) \\ \boldsymbol{\lambda}_v(t_f) = \mathbf{0} \end{cases} \tag{4.102}$$

with a constraint on the final squared Mahalanobis distance or miss distance:

$$\text{SMD}(\mathbf{r}_f) - \overline{\text{SMD}} = 0 \quad \text{or} \quad \text{d}(\mathbf{r}_f) - \overline{\text{d}} = 0 \tag{4.103}$$

The State transition matrix can be computed solving Eq. 2.98, with the following state matrix $\mathbf{A}$:

$$\mathbf{A} = \begin{bmatrix} \mathbf{0}_{3\times3} & \mathbb{I}_{3\times3} & \mathbf{0}_{3\times3} & \mathbf{0}_{3\times3} \\ -\mathbf{A}_{34} & \mathbf{0}_{3\times3} & \mathbf{0}_{3\times3} & -a_{\max}\mathbb{I}_{3\times3} \\ \mathbf{0}_{3\times3} & \mathbf{0}_{3\times3} & \mathbf{0}_{3\times3} & \mathbf{A}_{34} \\ \mathbf{0}_{3\times3} & \mathbf{0}_{3\times3} & -\mathbb{I}_{3\times3} & \mathbf{0}_{3\times3} \end{bmatrix} \tag{4.104}$$

where $\mathbf{A}_{34}$ is defined in Eq. 4.18. Then the procedure is analogous to the one described in Algorithm. 2.

B-plane dynamics

The EOP with scaled control acceleration is proposed exploiting BP dynamics as well. In this case the Hamiltonian is written as:

$$H = \frac{1}{2} a_{\max} \mathbf{a}_{c,s}^{\top} \mathbf{a}_{c,s} + a_{\max} \boldsymbol{\lambda}^{\top} \mathbf{N} \mathbf{a}_{c,s}. \tag{4.105}$$

The Hamiltonian's stationary point that defines the control law is:

$$\frac{\partial H}{\partial \mathbf{a}_{c,s}} = 0 \quad \rightarrow \quad a_{\max} \mathbf{a}_{c,s} + a_{\max} \mathbf{M}^{\top} \boldsymbol{\lambda} = 0 \tag{4.106}$$

$$\rightarrow \quad \mathbf{a}_{c,s} = -\mathbf{M}^{\top} \boldsymbol{\lambda}, \tag{4.107}$$

$$\mathbf{a}_c = -a_{\max} \mathbf{M}^{\top} \boldsymbol{\lambda}, \tag{4.108}$$

By substituting the resulting definition of the control acceleration $\mathbf{a}_c$ as function of the costate $\boldsymbol{\lambda}$ into the dynamics, the TPBVP can be written as:

$$\begin{cases} \dot{\mathbf{b}} = -a_{\max} \mathbf{M}(t) \mathbf{M}^{\top}(t) \boldsymbol{\lambda} \\ \dot{\boldsymbol{\lambda}} = \mathbf{0} \end{cases} \qquad \text{BCs} : \begin{cases} \mathbf{b}(t_0) = \mathbf{b}_0 \\ \boldsymbol{\lambda}(t) = \nu 2 \mathbf{C}^{-1} \mathbf{b}(t_f) \end{cases} \tag{4.109}$$

with the constraint on the final squared Mahalanobis distance or miss distance:

$$\mathbf{b}^{\top}(t_f) \mathbf{C}^{-1} \mathbf{b}(t_f) - \overline{\text{SMD}} = 0 \quad \text{or} \quad \|\mathbf{b}(t_f)\| - \overline{\text{d}} = 0. \tag{4.110}$$

The state matrix $\mathbf{A}$ reads:

$$\mathbf{A} = \begin{bmatrix} \mathbf{0}_{2\times 2} & -a_{\max} \mathbf{M} \mathbf{M}^{\top} \\ \mathbf{0}_{2\times 2} & \mathbf{0}_{2\times 2} \end{bmatrix}. \tag{4.111}$$

Then the procedure is analogous to the one described in Algorithm. 3.

4.3.1 Results

Considering the test case, the maximum acceleration available by the propulsion system has been set to $a_{\max} = 8 \cdot 10^{-6}$ m/s^2 for a manoeuvre starting 1.99 orbits before TCA. By applying the EOP with scaled control, the velocity costate profile represents the percentage of acceleration required compared to the maximum available, and it is reported in Figure 4.16.

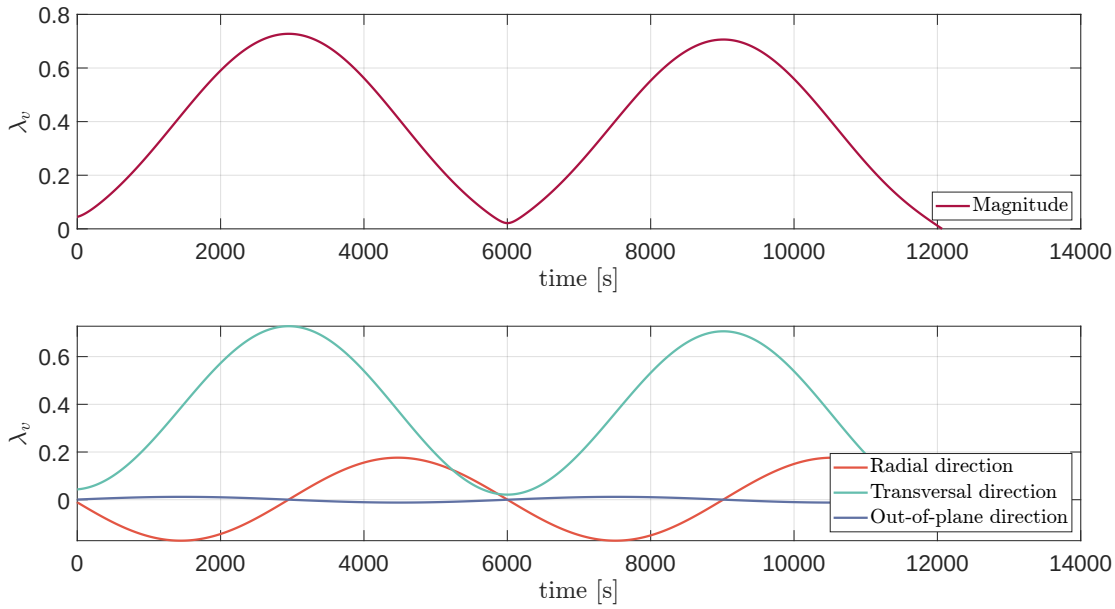

Figure 4.16: Velocity costate λ_v scaled on a_{max} = 8.0e-06 m/s^2 at 1.99 orbits before TCA.

4.4 Bang-Bang profile transformation

The control profile resulting from the solution of EOP consists in a continuous unbounded acceleration profile, which can be difficult to implement by the propulsion system and is non-optimal from the propellant consumption standpoint. To mitigate these issues, the continuous acceleration profile is turned into a bang-bang one by a smoothing approach based on the adoption of a hyperbolic tangential function. The resulting algorithm ensures more efficient manoeuvres than the continuous minimum-energy solutions [Mar21]. The main drawback of bang-bang solutions is that they introduce discontinuities in the motion equations. These discontinuities usually lead to convergence problems for Newton type algorithms. To remove this obstacle, a smooth representation of the bang-bang by an hyperbolic tangential is used [Tah18].
The modified control acceleration $\mathbf{a}_c$ vector is:

$$\mathbf{a}_c = -a_{\max} p \boldsymbol{\lambda}_v. \tag{4.112}$$

with p defined as:

$$p = \frac{a_{\min}}{\lambda_v + \epsilon} p_1 + p_2 p_3 + \frac{a_{\max}}{\lambda_v + \epsilon} p_4, \tag{4.113}$$

$$\begin{cases} p_1 = \frac{1}{2}(1 - \tanh \frac{\lambda_v - a_{\text{th,min}}}{\rho}) \\ p_2 = \frac{1}{2}(1 - \tanh \frac{\lambda_v - a_{\text{th,max}}}{\rho}) \\ p_3 = \frac{1}{2}(1 - \tanh \frac{a_{\text{th,min}} - \lambda_v}{\rho}) \\ p_4 = \frac{1}{2}(1 - \tanh \frac{a_{\text{th,max}} - \lambda_v}{\rho}) \end{cases} \tag{4.114}$$

$$\lambda_v = \|\boldsymbol{\lambda}_v\|\,, \tag{4.115}$$

Where:

- a_{min} and a_{max} are the minimum and maximum values of the acceleration, to be set according to the engine.
- $a_{\text{th,min}}$ and $a_{\text{th,max}}$ are the minimum and the maximum threshold acceleration.
- ρ and ϵ are respectively the smoothing parameter and a coefficient in order to have non-zero denominators ($\rho, \epsilon \ll 1$).

In order to obtain a pure bang-bang solution, the maximum and the minimum threshold accelerations must have the same value, $a_{\text{th,min}} = a_{\text{th,max}} = a_{\text{th}}$. The selection of a_{th} is a key element for ensuring the convergence for the EOP with constrained bang-bang structure. The value of a_{th} is selected with the following procedure:

1. set ρ and ϵ;
2. calculate the total impulse of the manoeuvre Δv_{tot} by integration of the acceleration profile;
3. compute an estimation of the burning time by $t^*_{ON} = \frac{\Delta v_{\text{tot}}}{a_{\text{max}}}$;
4. calculate a_{th} as the value with which the burning time obtained by capping the continuous profile solution is equal to t^*_{ON} (achieved with MATLAB® built-in function `fzero`).

The resulting problem consists in a TPBVP characterize by the same dynamics of Eq. 4.102 and the following Boundary Conditions:

$$\begin{cases} \boldsymbol{\lambda}_{rf} = \boldsymbol{\lambda}_{r\text{TCA}} \\ \boldsymbol{\lambda}_{vf} = \boldsymbol{\lambda}_{v\text{TCA}} \\ \text{SMD}(\mathbf{r}_f) = \overline{\text{SMD}}. \end{cases} \tag{4.116}$$

Solving this problem consists in finding the values of the 6 unknowns, $\boldsymbol{\lambda}_r(t_0)$ and $\boldsymbol{\lambda}_v(t_0)$, that propagated until t_f satisfy Eq. 4.116. The *Levenberg-Marquardt* method implemented in MATLAB® built-in function `fsolve` is used with initial guesses for $\boldsymbol{\lambda}_{r0}$ and $\boldsymbol{\lambda}_{v0}$ provided by the solution of the EOP Algorithm with the continuous profile. The resulting algorithm is summarised in Algorithm 4.

Algorithm 4 EOP-BangBang

Input: CDM, $\overline{\text{SMD}}$, $\Delta\theta$_range, EOP solution, $a_{\max}, \rho, \epsilon$
Output (for each $\Delta\theta$): $\mathbf{r}_f$, SMD, PoC, $\mathbf{a}_c$, $\Delta\mathbf{v}$, Δm
for i = 1 : *size*($\Delta\theta$_range) **do**
    given Δv_{tot} from EOP unbounded solution, compute $t^*_{ON} = \Delta v_{\text{tot}}/a_{\max}$
    calculate a_{th} which provides t^*_{ON} for the bang-bang manoeuvre with MATLAB® built-in function `fzero`
    Select $\boldsymbol{\lambda}_{r0}, \boldsymbol{\lambda}_{v0}$ and ν_0 from EOP solution as initial guesses
    Solve Eq. 4.116 for $\boldsymbol{\lambda}_{r0}, \boldsymbol{\lambda}_{v0}$ with the control acceleration in Eqs. 4.112, 4.113 and 4.114 with MATLAB® built-in function `fsolve`
    controlled forward propagation:
    $[\mathbf{r}_f, \mathbf{v}_f, \boldsymbol{\lambda}_{rf}, \boldsymbol{\lambda}_{vf}, m_f] = control\_propagator([\mathbf{r}_0, \mathbf{v}_0, \boldsymbol{\lambda}_{r0}, \boldsymbol{\lambda}_{v0}, m_0],$ tspan_forward)
    $\Delta\mathbf{r} = \mathbf{r}_f - \mathbf{r}_s$
    SMD = $squared\_mahalanobis\_distance(\Delta\mathbf{r}, \text{CDM})$
    PoC = $poc\_chan(\Delta\mathbf{r}, \text{CDM})$
    $\Delta m = m_f - m_0$
end for

B-plane dynamics

As with the resolution of the unbounded EOP, the problem formulation in B-plane coordinates is investigated also in the case of a bang-bang acceleration structure. The modified control acceleration $\mathbf{a}_c$ vector is:

$$\mathbf{a}_c = -a_{\max} p \mathbf{u}, \quad \mathbf{u} = \mathbf{M}^\top \boldsymbol{\lambda} \tag{4.117}$$

with p defined as:

$$p = \frac{a_{\min}}{u + \epsilon} p_1 + p_2 p_3 + \frac{a_{\max}}{u + \epsilon} p_4, \tag{4.118}$$

$$\begin{cases} p_1 = \frac{1}{2}(1 - \tanh \frac{u - a_{\text{th,min}}}{\rho}) \\ p_2 = \frac{1}{2}(1 - \tanh \frac{u - a_{\text{th,max}}}{\rho}) \\ p_3 = \frac{1}{2}(1 - \tanh \frac{a_{\text{th,min}} - u}{\rho}) \\ p_4 = \frac{1}{2}(1 - \tanh \frac{a_{\text{th,max}} - u}{\rho}) \end{cases} \tag{4.119}$$

$$u = \|\mathbf{u}\| \tag{4.120}$$

The problem is then solved in an equivalent manner tot hat described in Algorithm 4, referring to TPBVP with dynamics in B-plane r.f. in Eq. 4.109.

4.4.1 Results

The EOP algorithm with bang-bang acceleration structure is applied to the test case, for a manoeuvre starting $\Delta\theta = 1.99$ orbits before TCA. The maximum acceleration affordable by the thrusters is set $a_{\max} = 8 \cdot 10^{-6}$ m/s^2. The selected smoothing coefficients are: $\rho = 10^{-11}$, $\epsilon = 10^{-20}$, and the corresponding acceleration threshold is $a_{\text{th,max}} = 4.9956 \cdot 10^{-6}$ m/s^2. The bang-bang transformation of the control acceleration, both in magnitude and in LVLH components, is shown in Figure 4.17.

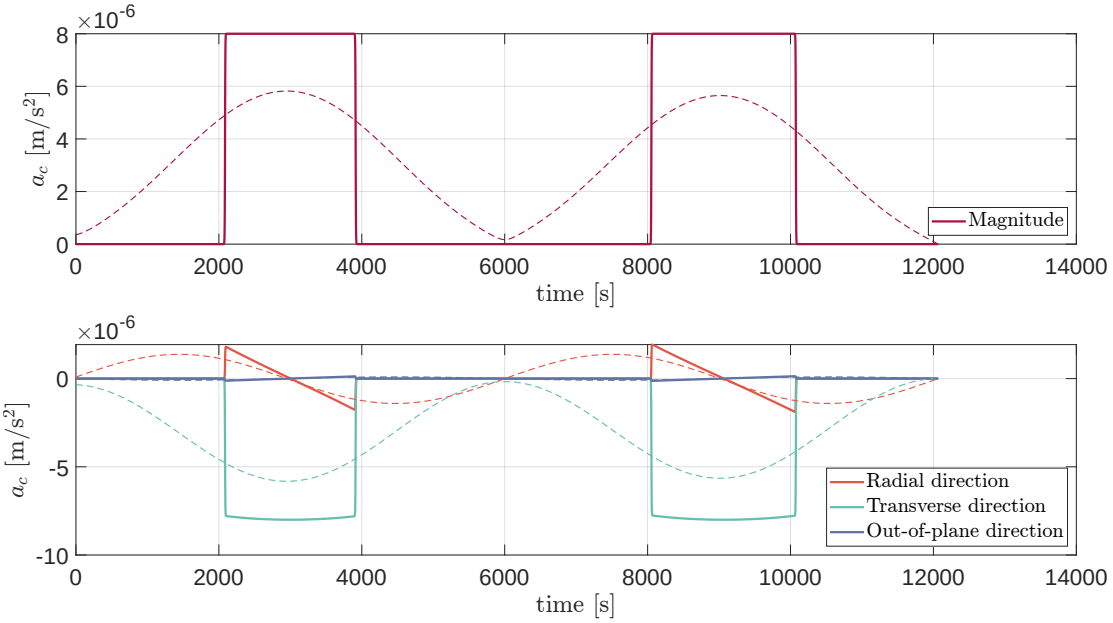

Figure 4.17: Control acceleration profile as fraction of a_{max} for unbounded solution (dashed line) and after bang-bang transformation (continuous line) at 1.99 orbits before TCA. Smoothing coefficient: $\rho = 10^{-11}$.

Figure 4.18 is reported with the intention of showing the effect of the variation of the smoothing coefficient ρ: choosing a larger value (in this case $\rho = 10^{-9}$) the profile is much smoother then with $\rho = 10^{-11}$ and tends towards unbounded profile.

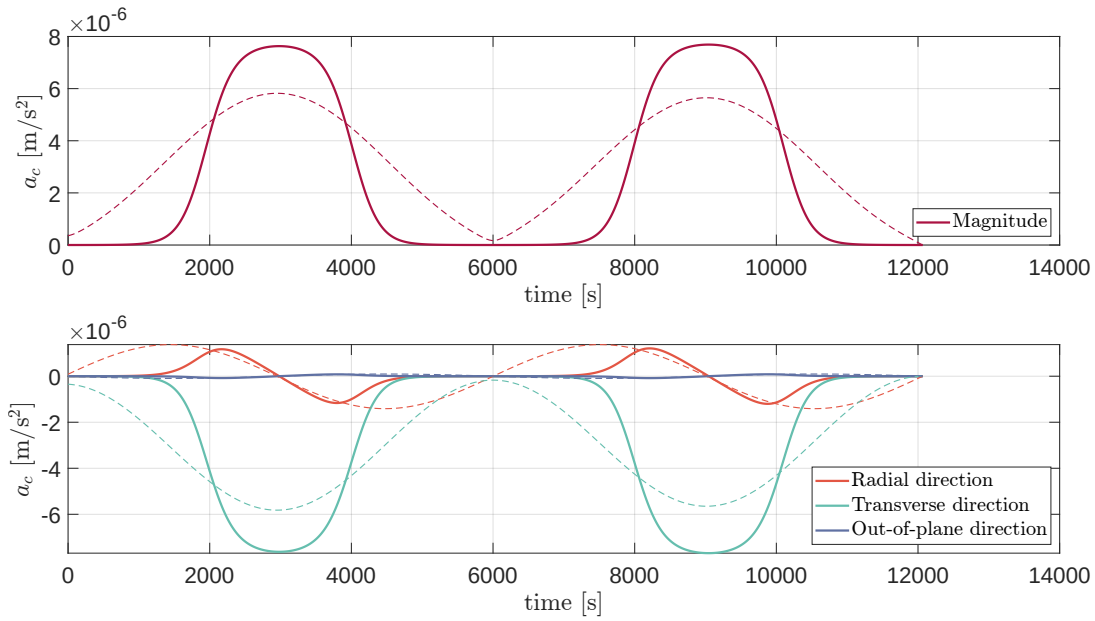

Figure 4.18: Control acceleration profile as fraction of a_{max} for unbounded solution (dashed line) and after bang-bang transformation (continuous line) at 1.99 orbits before TCA. Smoothing coefficient: $\rho = 10^{-9}$.

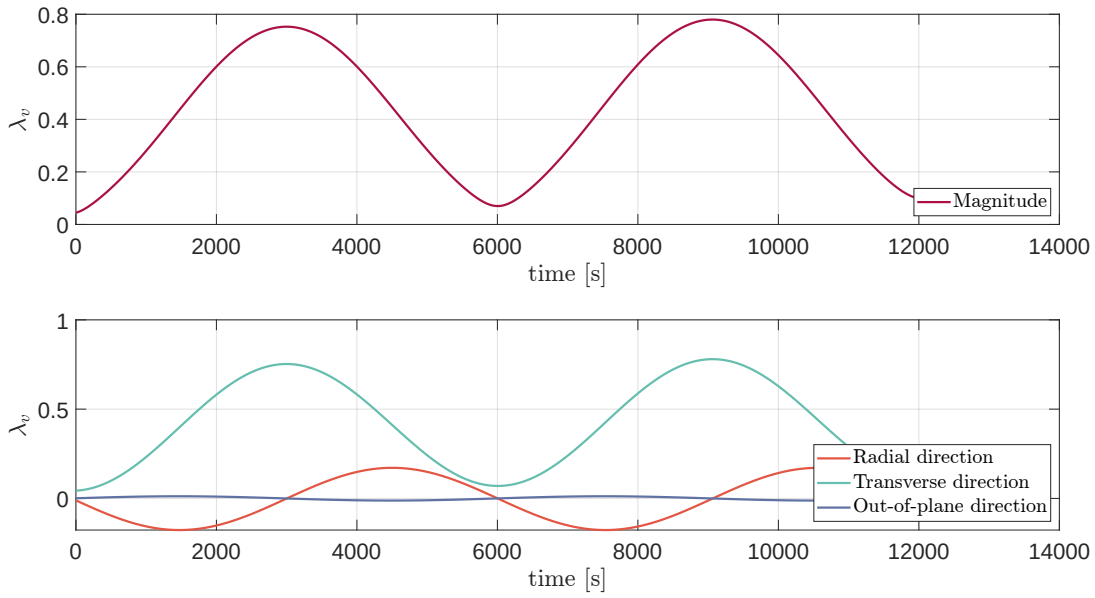

Figure 4.19: Velocity costate scaled on a_{max} for bang-bang transformation.

The velocity costate obtained represents the fraction of the unbounded $\mathbf{a}_c$ with respect to $a_{\max}$. The trend of $\boldsymbol{\lambda}_v$ vs. the true anomaly is reported in Fig 4.19. In order to analyse the behaviour of the solution when the maximum acceleration increases, the profiles obtained for different values of $a_{\max}$, with $\rho = 10^{-11}$, are reported in Figure 4.20 and the number of iterations required for convergence is shown in Table 4.1.

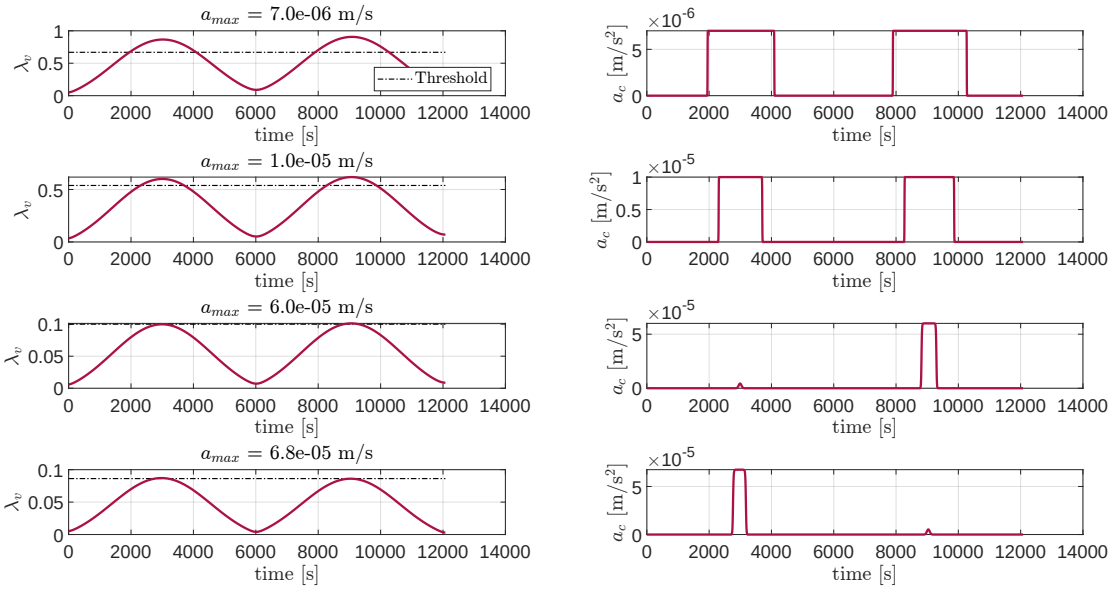

Figure 4.20: Velocity costate and control acceleration profiles obtained for different values of $a_{\max}$, with $\rho = 10^{-11}$ at $\Delta\theta = 1.99$ orbits before TCA.

Table 4.1: Number of iterations required for convergence increasing $a_{\max}$ value.

$\boldsymbol{a_{\max}}$ [m/s^2]	7e-06	1e-05	6e-05	6.75e-05
Number of iterations	7	8	12	33

Table 4.1 shows the growth of the number of iterations as $a_{\max}$ increases: this means that achieving convergence becomes more difficult. This result is expected since enlarging the maximum acceleration implies that the low-thrust manoeuvre tends towards an impulsive manoeuvre. For this particular initial manoeuvring point, the equivalent costs of the manoeuvre respectively solving the unbounded EOP and imposing a bang-bang structure, result to be:

- unbounded solution: $\Delta v_{eq} = 9.8278 \cdot 10^{-4}$ m/s.
- bang-bang structure: $\Delta v_{eq} = 2.1497 \cdot 10^{-4}$ m/s.

The gain in terms of Δv_{eq} provided by the bang-bang algorithm is confirmed by plotting the behaviour of the equivalent cost is reported for 50 initial manoeuvring point in Fig 4.21.

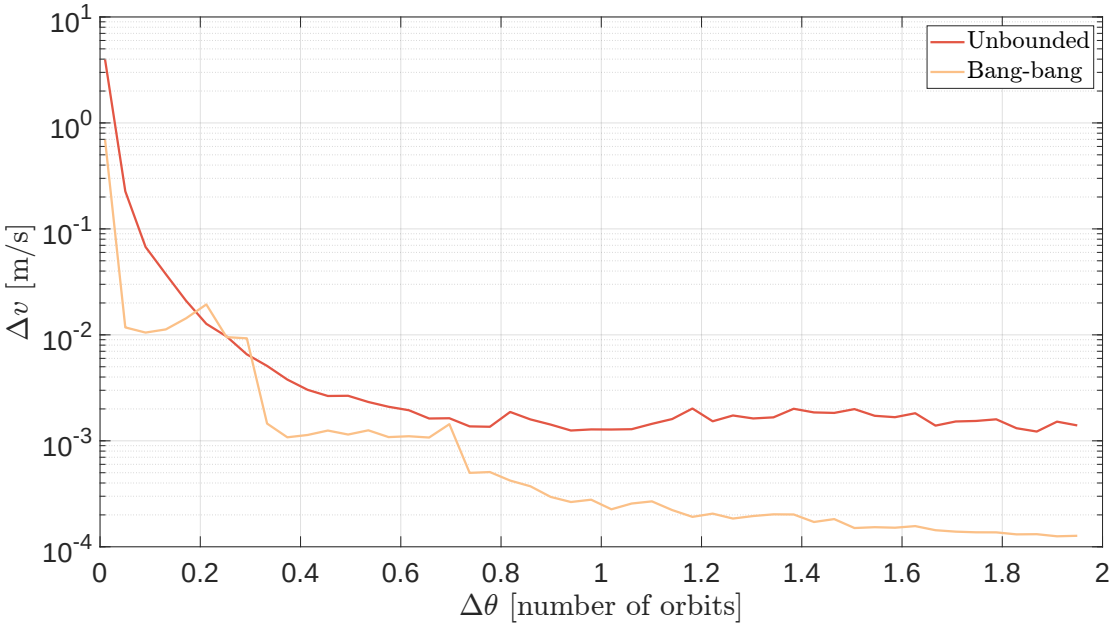

Figure 4.21: Equivalent Δv: comparison between the unbounded control problem and the enforced bang-bang profile.

4.5 Energy optimal with tangential control

In some operational scenarios it may be preferable to implement a purely tangential sub-optimal manoeuvre. The purpose of this section is to derive the procedure by analysing this application case. The control acceleration is written as fraction ε of the maximum acceleration affordable for the satellite thrusters $a_{\max}$, constrained to have only tangential components, by means of the unit vector $\mathbf{t}$ in the velocity direction:

$$\mathbf{a}_c = a_{\max}\varepsilon\mathbf{t}, \quad \text{where} \quad \mathbf{t} = \frac{\mathbf{v}}{v}. \tag{4.121}$$

The dynamic system, assuming a restricted two-body problem, can be written as:

$$\begin{cases} \dot{\mathbf{r}} = \mathbf{v} \\ \dot{\mathbf{v}} = -\dfrac{\mu}{r^3}\mathbf{r} + a_{\max}\varepsilon\mathbf{t}. \end{cases} \tag{4.122}$$

The performance index L of the optimal control problem is:

$$L = \frac{1}{2} a_{\max} (\varepsilon \mathbf{t})^\top (\varepsilon \mathbf{t}) \tag{4.123}$$

and the Hamiltonian reads:

$$H = \frac{1}{2} a_{\max} \varepsilon^2 + \boldsymbol{\lambda}_r^\top \mathbf{v} + \boldsymbol{\lambda}_v^\top (-\frac{\mu}{r^3} \mathbf{r} + a_{\max} \varepsilon \mathbf{t}). \tag{4.124}$$

The control law is obtained by means of the Pontryagin's minimum principle, finding the value of the control parameter ε that minimises the Hamiltonian:

$$\frac{\partial H}{\partial \varepsilon} = 0 \quad \rightarrow \quad a_{\max} \varepsilon + a_{\max} \boldsymbol{\lambda}_v \cdot \mathbf{t} = 0, \tag{4.125}$$

$$\rightarrow \quad \varepsilon = -\boldsymbol{\lambda}_v \cdot \mathbf{t} = -\boldsymbol{\lambda}_v \cdot \frac{\mathbf{v}}{v}. \tag{4.126}$$

The Euler-Lagrange equations are obtained by substituting the specific problem quantities into Eq. 2.93:

$$\begin{cases} \dot{\mathbf{r}} = \mathbf{v} \\ \dot{\mathbf{v}} = -\dfrac{\mu}{r^3} \mathbf{r} - a_{\max} \left(\boldsymbol{\lambda}_v \cdot \dfrac{\mathbf{v}}{v} \right) \mathbf{t} \\ \dot{\boldsymbol{\lambda}}_r = \dfrac{\mu}{r^3} \boldsymbol{\lambda}_v - \dfrac{3\mu \mathbf{r} \cdot \boldsymbol{\lambda}_v}{r^5} \mathbf{r} \\ \dot{\boldsymbol{\lambda}}_v = -\boldsymbol{\lambda}_v \end{cases} \tag{4.127}$$

and the control law is defined as:

$$\mathbf{a}_c = -a_{\max} \left(\boldsymbol{\lambda}_v \cdot \frac{\mathbf{v}}{v} \right) \mathbf{t}. \tag{4.128}$$

The STM can be computed from the state matrix $\mathbf{A}$:

$$\mathbf{A} = \begin{bmatrix} \mathbf{0}_{3\times3} & \mathbb{I}_{3\times3} & \mathbf{0}_{3\times3} & \mathbf{0}_{3\times3} \\ -\mathbf{A}_{34} & \mathbf{0}_{3\times3} & \mathbf{0}_{3\times3} & \mathbf{A}_{24} \\ \mathbf{0}_{3\times3} & \mathbf{0}_{3\times3} & \mathbf{0}_{3\times3} & \mathbf{A}_{34} \\ \mathbf{0}_{3\times3} & \mathbf{0}_{3\times3} & -\mathbb{I}_{3\times3} & \mathbf{0}_{3\times3} \end{bmatrix} \tag{4.129}$$

where in particular:

$$\mathbf{A}_{24} = -a_{\max} \left[\frac{\mathbf{v}}{v} \left(\frac{\mathbf{v}}{v} \right)^\top \right]. \tag{4.130}$$

and $\mathbf{A}_{34}$ is defined in Eq. 4.18. Then the procedure is analogous to the one described in Algorithm. 2.

B-plane dynamics

The energy-optimal CAM in purely tangential direction can be also found by projecting the problem onto B-plane. The dynamics of the tangential low-thrust manoeuvre exploiting B-plane dynamics is:

$$\dot{\mathbf{b}} = a_{\max}\varepsilon\mathbf{M}\mathbf{t} \tag{4.131}$$

where $\mathbf{t}$ is the unit vector $\mathbf{t}$ in the velocity direction $\mathbf{t} = \mathbf{v}/v$, and in LVLH r.f. $\mathbf{t} = [0; 1; 0]^\top$. The Hamiltonian of the problem is:

$$H = \frac{1}{2}a_{\max}\varepsilon^2 + a_{\max}\varepsilon\boldsymbol{\lambda}^\top\mathbf{M}\mathbf{t}. \tag{4.132}$$

The Hamiltonian's stationary points are found in order to apply the Pontryagin's minimum principle and obtain the control law:

$$\frac{\partial H}{\partial \varepsilon} = 0 \quad \rightarrow \quad a_{\max}\varepsilon + a_{\max}\boldsymbol{\lambda}\cdot\mathbf{M}\mathbf{t} = 0, \tag{4.133}$$

$$\rightarrow \quad \varepsilon = -\boldsymbol{\lambda}\cdot\mathbf{M}\mathbf{t} = -\boldsymbol{\lambda}\cdot\mathbf{M}\mathbf{t}. \tag{4.134}$$

Thus the Euler-Lagrange equations are obtained:

$$\begin{cases} \dot{\mathbf{b}} = -a_{\max}\left(\boldsymbol{\lambda}\cdot\mathbf{M}\mathbf{t}\right)\mathbf{M}\mathbf{t} \\ \dot{\boldsymbol{\lambda}} = \mathbf{0} \end{cases} \tag{4.135}$$

with the control law:

$$\mathbf{a}_c = -a_{\max}\left(\boldsymbol{\lambda}\cdot\mathbf{M}\mathbf{t}\right)\mathbf{t} \tag{4.136}$$

The STM can be computed by integrating the state matrix $\mathbf{A}$, following Eq. 2.98:

$$\mathbf{A} = \begin{bmatrix} \mathbf{0}_{2\times2} & \mathbf{A}_{12} \\ \mathbf{0}_{2\times2} & \mathbf{0}_{2\times2} \end{bmatrix} \tag{4.137}$$

$$\mathbf{A}_{12} = -a_{\max}\left[\mathbf{M}\frac{\mathbf{v}}{v}\left(\mathbf{M}\frac{\mathbf{v}}{v}\right)^\top\right]. \tag{4.138}$$

Then the procedure is analogous to the one described in Algorithm. 3.

4.5.1 Results

The results of the purely tangential manoeuvre considering the ECI dynamics are presented in this section; the graphs relative to the formulation in B-plane coordinates are not reported since they are very similar as for the manoeuvre without directional limits. Similarly, the approach could also be applied to a final constraint on the miss distance and the same considerations would still be valid. For each initial manoeuvring point with $\Delta\theta \in [0, 4\pi]$ the algorithm has been applied and the final position achieved after the control application, projected onto B-plane, can be found in Figure 4.22.

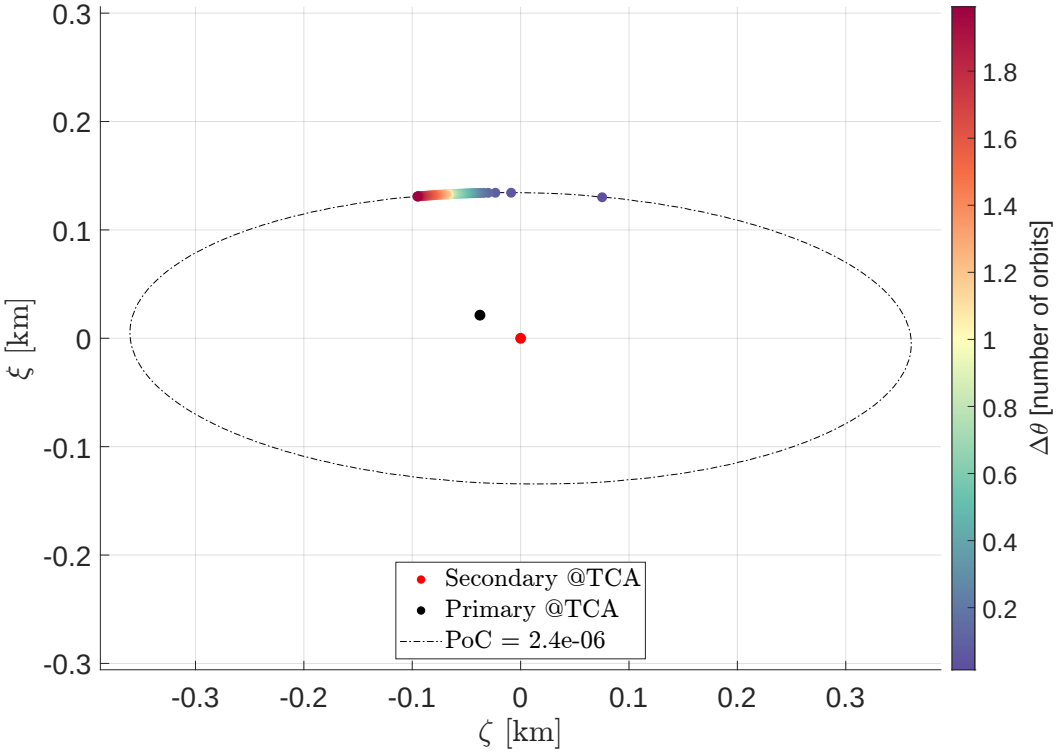

Figure 4.22: Final position in B-plane r.f. reached after the optimal manoeuvre, manoeuvres starting from 2 orbits before TCA until the expected impact. Tangential EOP with ECI dynamics and constrained SMD.

Figure 4.23 reports both the "estimated" and "real" collision probability profile: the former is computed directly after the resolution of the system in with the value of $\mathbf{r}_f$ estimated through the STM and the SMD constraint equation; the latter is the PoC calculated with the actual final position $\mathbf{r}_f$ obtained after the integration of the manoeuvred dynamics. The estimated behaviour perfectly matches the

enforced value, accounting for numerical errors and the real profile remains close to the threshold without ever exceeding it. The result is absolutely acceptable since 2 orbits before the CA the maximum deviation is $2.5068 \cdot 10^{-8}$, two orders of magnitude lower than the constraint.

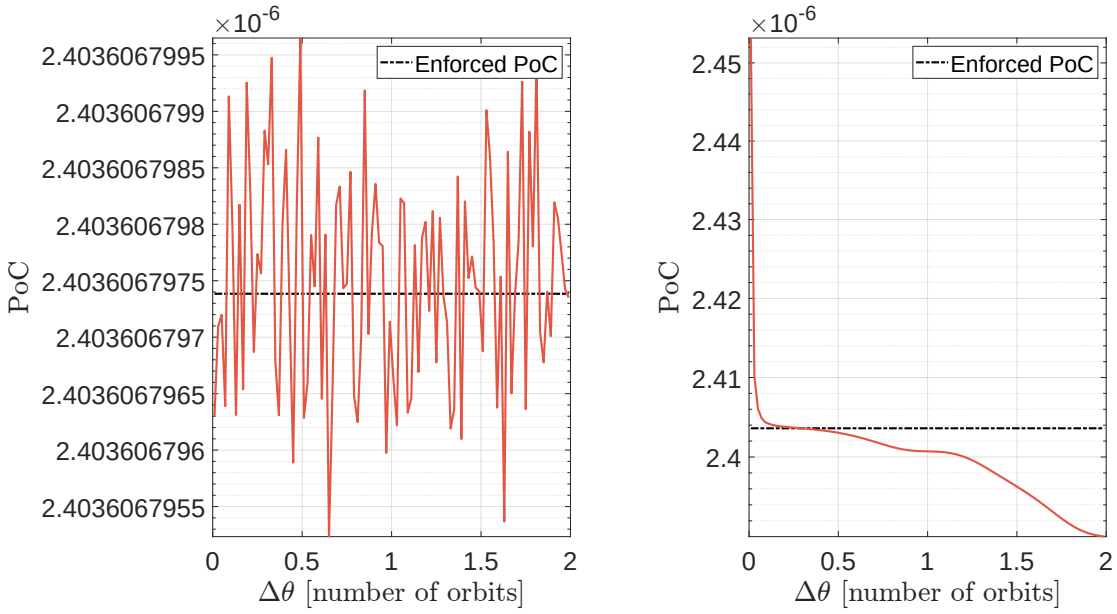

Figure 4.23: Collision probability: estimated value (left) and real profile after the dynamics propagation (right). Tangential EOP with ECI dynamics and constrained SMD.

After the resolution of the dynamics of the manoeuvre, the control acceleration profile is found. For each $\Delta\theta$ the equivalent cost in terms of Δv has been calculated and the resulting values are reported at the top of Figure 4.24. The equivalent Δv increases consistently when the manoeuvre is performed close to the expected collision. At the bottom of the same figure the development of the maximum control acceleration required can be found, with components in LVLH r.f.. Starting from the furthest points from the TCA, the out-of-plane component is practically null, and the transverse one is several orders of magnitude larger than the radial component: the tangential constraint has been successfully satisfied.

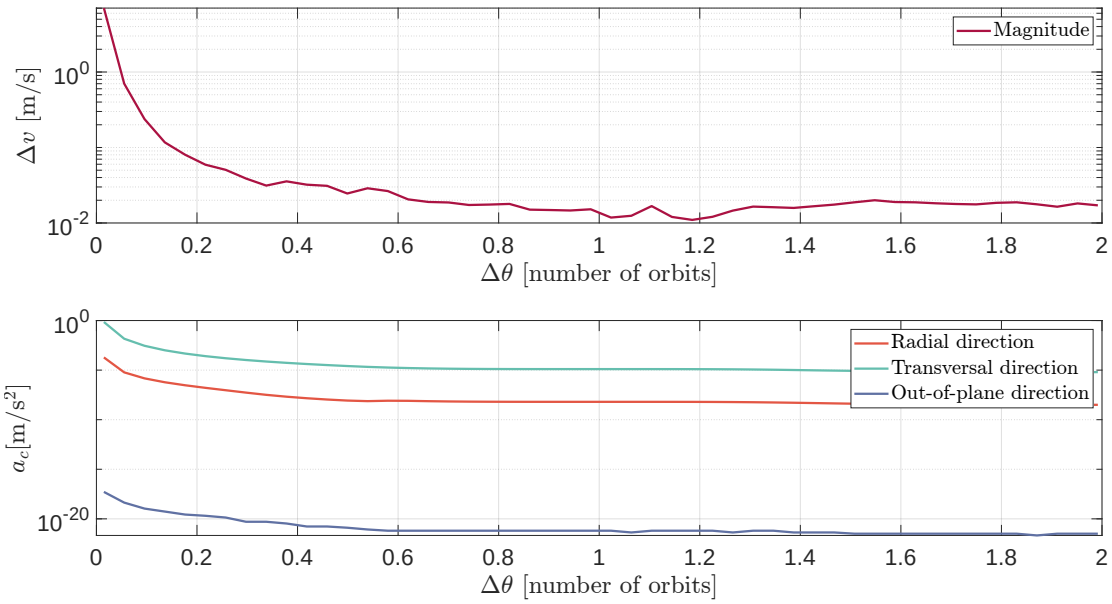

Figure 4.24: Equivalent impulse Δv (top) and maximum control acceleration $\mathbf{a}_c$ (bottom) for each initial manoeuvring point. Tangential EOP with ECI dynamics and constrained SMD.

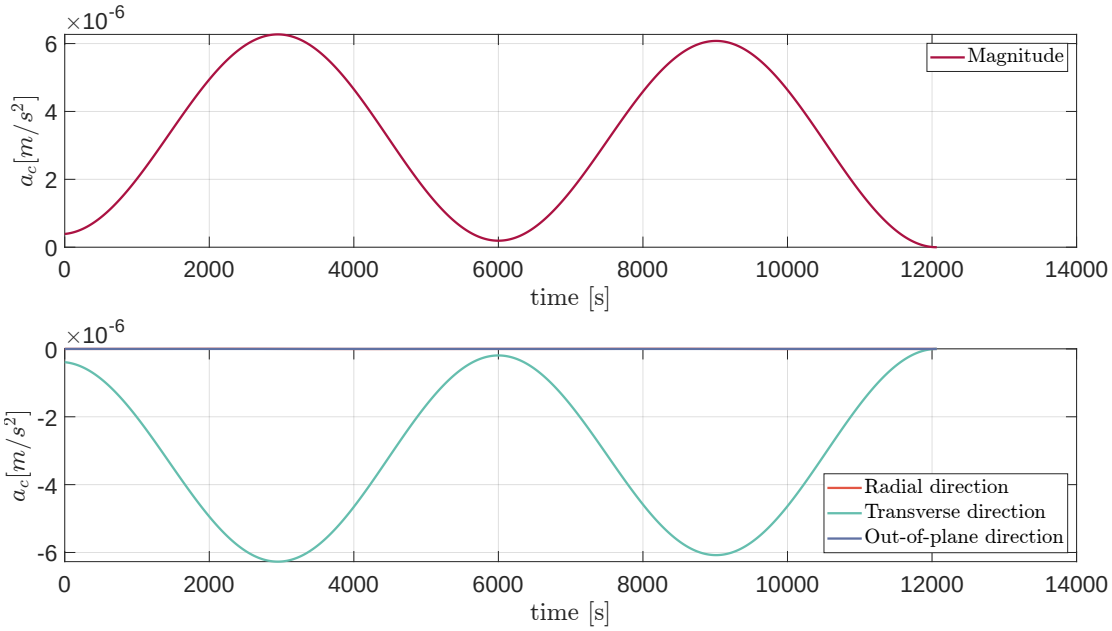

Figure 4.25: Control acceleration profile for a manoeuvre starting 1.99 orbits before TCA. Tangential EOP with ECI dynamics and constrained SMD.

The profile of the control acceleration highly depends on which point is taken to start the manoeuvre. The results considering an initial manoeuvre point with

$\Delta\theta = 1.99$ orbits before TCA are shown in Figure 4.25.It confirms that the manoeuvre is performed in the direction of the satellite's velocity.
The maximum thrust required by the spacecraft and the variation of mass are plotted for each manoeuvre point and presented in Figure 4.26. Approaching the small $\Delta\theta$ the thrust increases until values that are not compatible with low-thrust systems (order of 10^3 N).

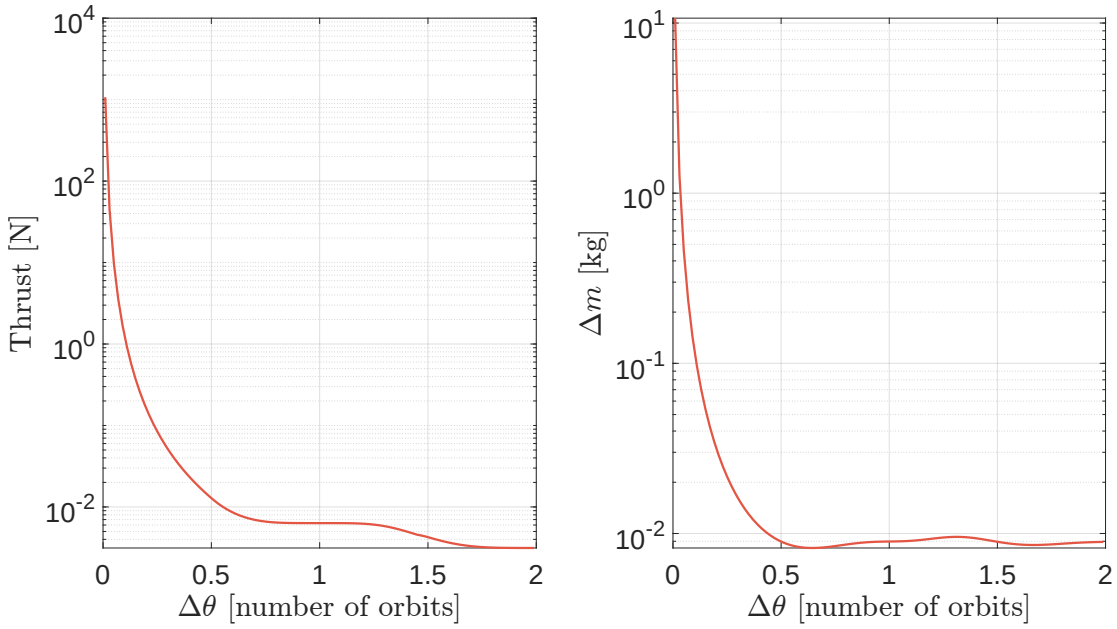

Figure 4.26: Tangential low-thrust manoeuvre with ECI dynamics with SMD constraint: thrust and mass variations.

Figure 4.27 shows the differences between the tangential manoeuvre formulated in ECI and BP r.f. in terms of final collision probability. The PoC profile for each true anomaly of the initial manoeuvre point, calculated with the actual final position $\mathbf{r}_f/\mathbf{b}_f$ is obtained after the integration of the manoeuvred dynamics. Even though the ECI algorithm is more accurate and it never exceeds the threshold, both of them are close to the enforced value: for the B-plane algorithm the maximum deviation is $8.3907 \cdot 10^{-8}$, still in the same order of magnitude of the error in ECI coordinates, $4.9582 \cdot 10^{-8}$.

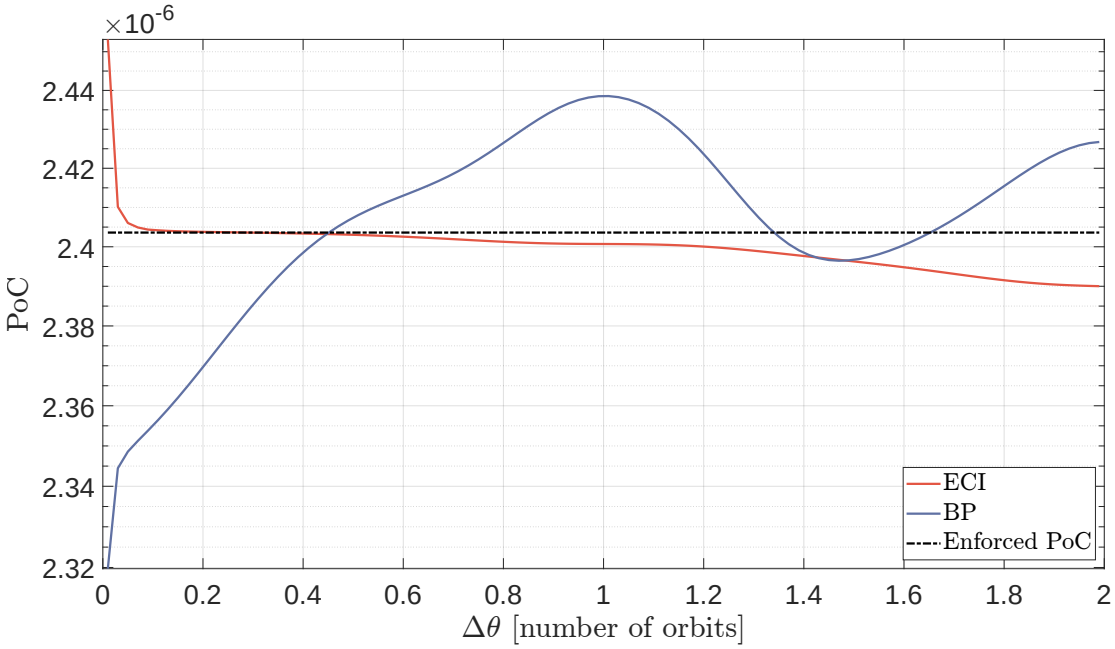

Figure 4.27: Collision probability profile after the dynamics propagation: comparison between Tangential EOP in ECI and BP coordinates, constrained SMD.

CHAPTER 5

Statistical analyses

In this chapter the algorithms presented in Chapter 3 and Chapter 4 are applied to a large database of test cases derived from the ESA Collision Avoidance Challenge [ESAd], then processed and collected in [Arm] by Roberto Armellin and available for download. For the competition, ESA provided the teams with real conjunction data extracted from 162,634 CDMs, corresponding to 13,154 unique events. These data were filtered to consider conjunctions with $d < 2\,\text{km}$ and $\text{PoC} < 10^{-6}$ resulting in a new data file with 2,170 conjunctions. All the conjunctions are relative to objects in LEO with 90% of cases with relative conjunction speed $\in [1.80;\ 14.98]$ km/s. Further information about the database can be found in [Arm21].
In addition, a validation of the methods proposed in the previous chapter in a dynamical framework including perturbations (drag and Earth's gravitational

harmonics) is provided. A comparison among all the different methods proposed in terms of computational time is presented at the end of the chapter.

5.1 Statistical analysis on optimal impulsive manoeuvre

In this section, a statistical analysis on the optimal impulsive manoeuvre introduced in Section 3.1 is performed, using a database of 2,170 collisions published for the ESA Collision Avoidance Challenge.
The maximum and minimum values in magnitude of Δv required for the optimal impulsive manoeuvre are identified for each possible true anomaly $\Delta\theta$ of the manoeuvring point, with $\Delta\theta \in [0, 4\pi]$. The minimum and maximum lines are shown together with the percentile values in Figure 5.1. The percentiles are computed at each value $val = [10\%,\ 20\%,\ ...,\ 90\%]$.

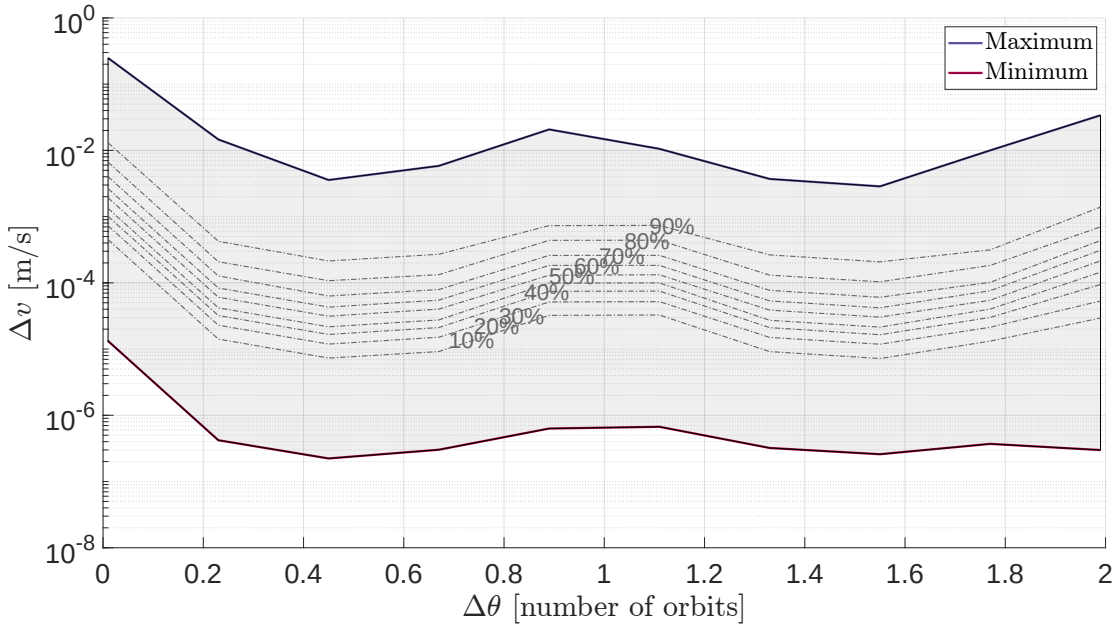

Figure 5.1: Magnitude of $\Delta\mathbf{v}$ for impulsive manoeuvres using ESA Challenge database.

It can be noticed that, focusing on 90% of the collisions, Δv does not exceed the order of magnitude of mm/s until very small values of $\Delta\theta$ (close to the time of the expected impact), and even for the smallest value of true anomaly considered, the maximum is $1.3 \cdot 10^{-2}$ m/s.
The three components of the $\Delta\mathbf{v}$ vector in LVLH r.f. are reported together in

Figure 5.2 and then in separate plots with their percentiles in Figure 5.3.

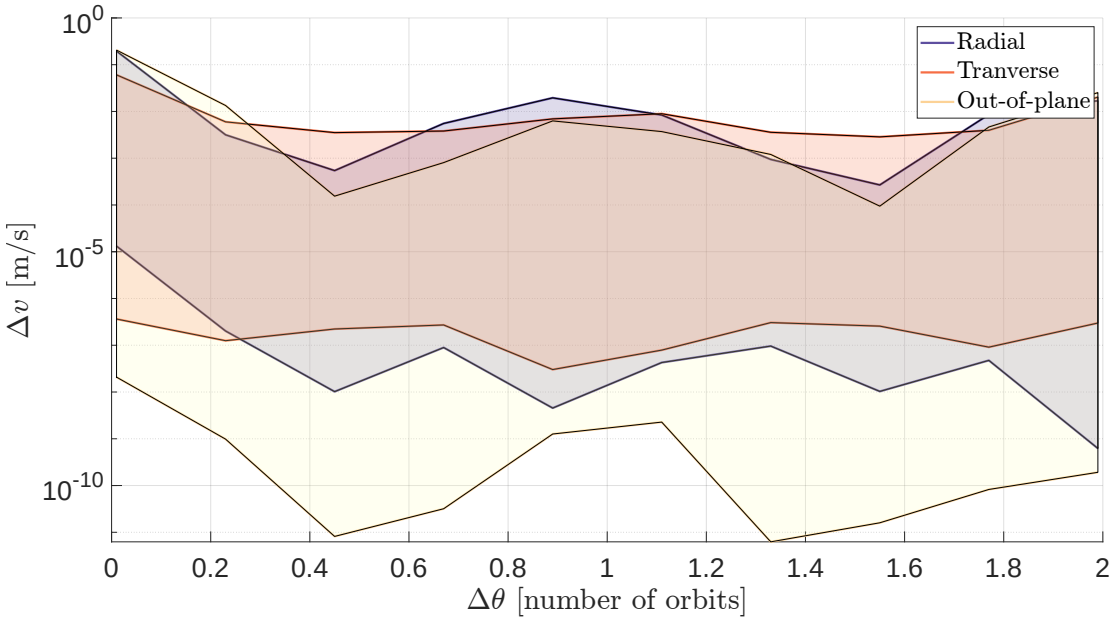

Figure 5.2: Components of the impulse Δv for impulsive manoeuvres, ESA Challenge database.

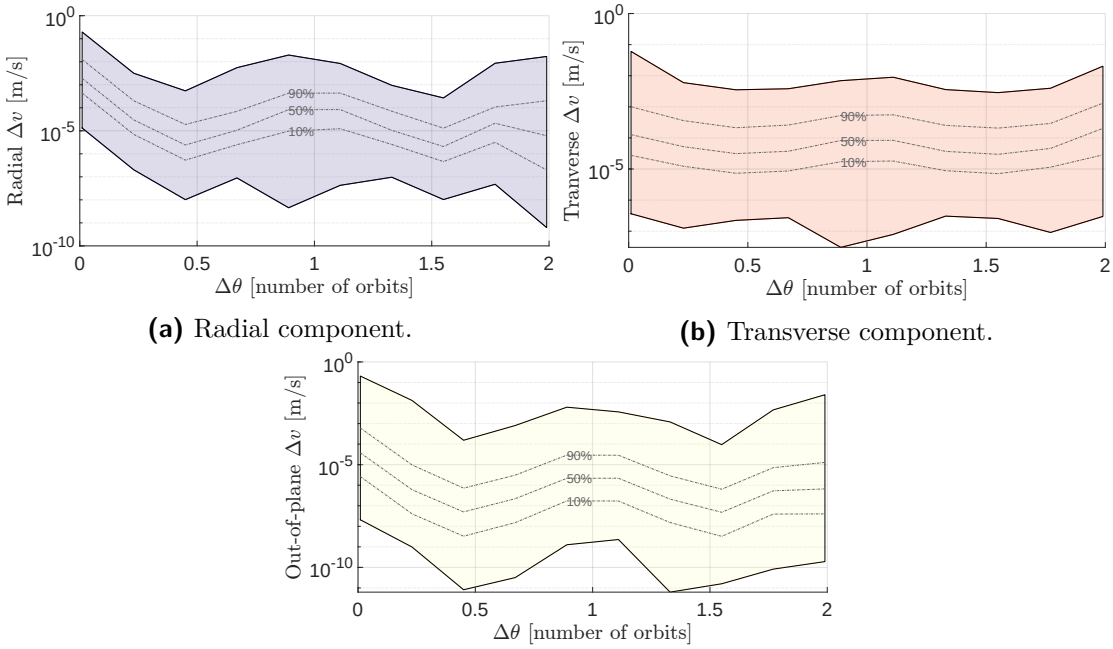

(a) Radial component.

(b) Transverse component.

(c) Out-of-plane component.

Figure 5.3: $\Delta \mathbf{v}$ components with percentiles for impulsive manoeuvres.

Some observations can be made regarding the behaviour of the three components of the impulse:

- the radial component, in 90% of the cases analysed, oscillates between 10^{-4} and 10^{-3} m/s with a maximum of ~ 0.2 m/s;
- the transverse component is, in general, the largest and the most regular one, with the 90% of cases around 10^{-3} m/s and a maximum of ~ 0.06 m/s;
- the out-of-plane component is the most fluctuating, and in general the smallest one, with minima at $\Delta\theta = (2k+1)\pi$ and maxima at $\Delta\theta = 2k\pi$, with $k = 0, 1, 2, ..., n$. The 90% of cases analysed shows a $\Delta\mathbf{v}$ that varies between 10^{-5} and 10^{-3} m/s with a maximum of ~ 0.2 m/s.

5.2 Statistical analysis on optimal low-thrust manoeuvre

This section presents the results of the statistical analysis performed over the 2,170 collisions published for the ESA Collision Avoidance Challenge, applying the energy-optimal algorithm for low-thrust manoeuvre derived in Section 4.1. For each true anomaly $\Delta\theta$ of the possibles initial manoeuvring point, the equivalent Δv has been computed by integrating the control acceleration profile and the minimum and maximum values over the collision database are shown in Figure 5.4 with the relative percentile values.

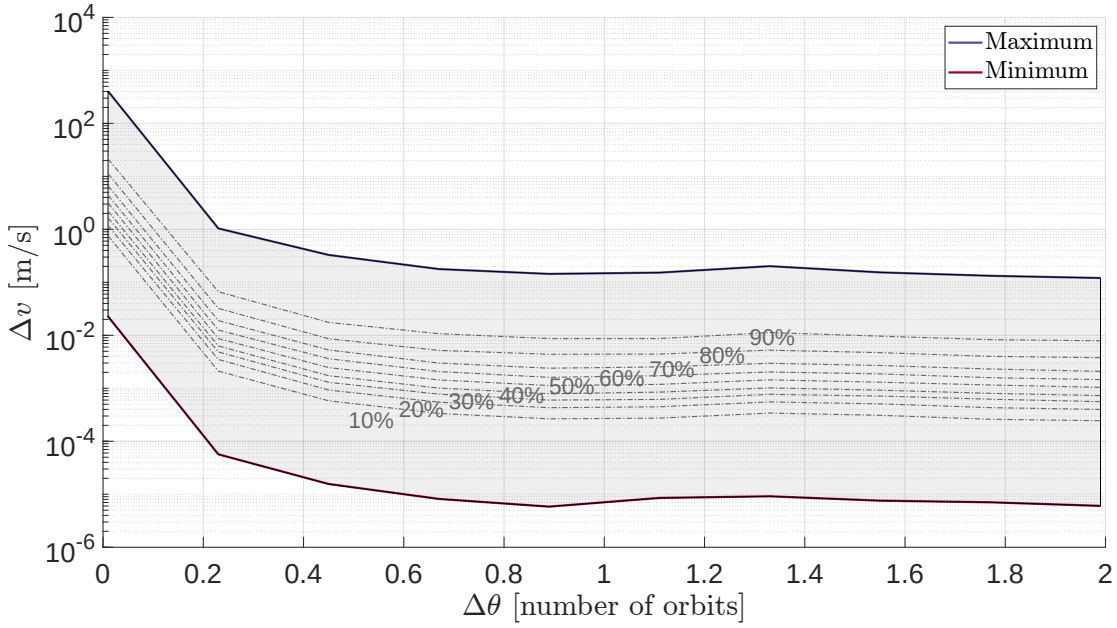

Figure 5.4: Magnitude of $\Delta\mathbf{v}$ for EOP algorithm, using ESA Challenge database.

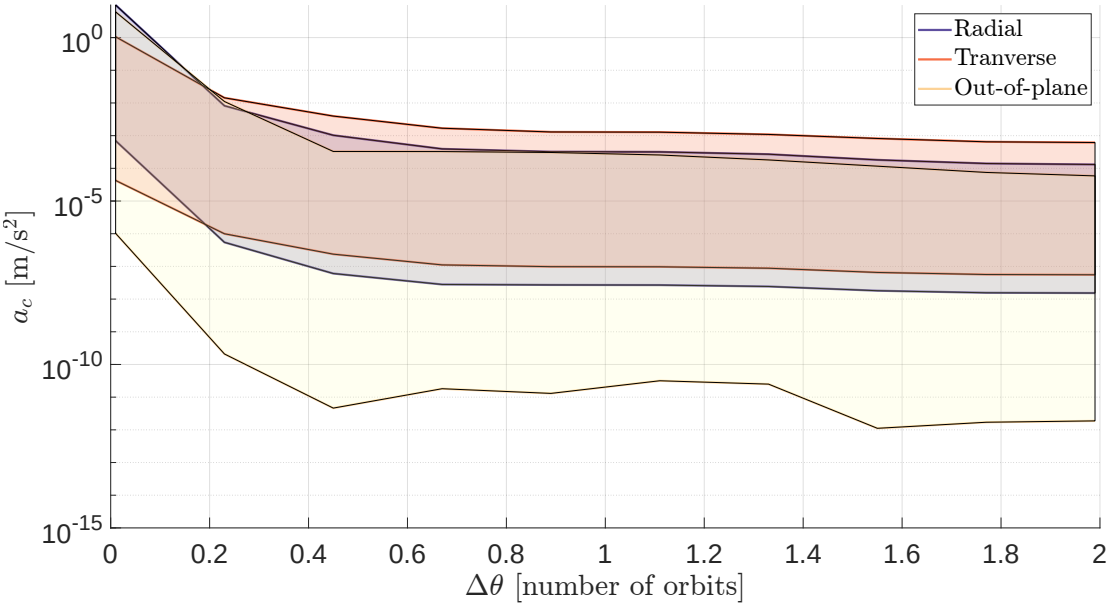

Figure 5.5: Control acceleration components for EOP algorithm, ESA Challenge database.

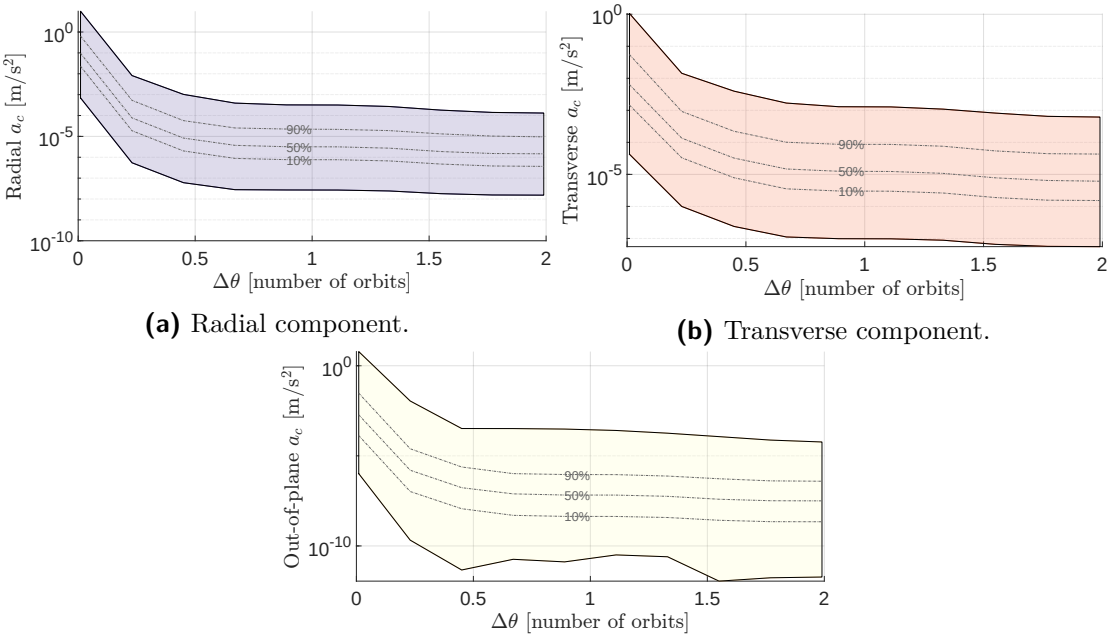

(a) Radial component.

(b) Transverse component.

(c) Out-of-plane component.

Figure 5.6: Components of the control acceleration in the three directions (LVLH r.f.) with percentiles.

The 90% of cases remain in the order of 10^{-2} m/s with a maximum of ~ 20 m/s at the instant of time closest to the expected impact. The maximum value of the

three components of the acceleration vector $\mathbf{a}_c$ are reported together in Figure 5.5 and then in separate plots with their relative percentiles in Figure 5.6.
As already stated in Section 4.1.3, from Figure 5.5 it is proved that, except for last-minute manoeuvres, the transverse component is indeed the dominant one and the manoeuvre is mostly performed in tangential direction. Below a certain true anomaly ($\Delta\theta \simeq 0.2$ orbits) thrust with a substantial radial component is necessary in order to avoid the collision. The out-of-plane component is confirmed to be the smallest one, several orders of magnitude lower than the others.

5.3 Statistical analysis on low-thrust bang-bang solution

A statistical analysis on the collisions database has been performed also for the bang-bang transformation profile algorithm and the convergence has been studied for ten different values of the maximum control acceleration, ten values of the true anomaly of the initial manoeuvring point and two values of the smoothing coefficient:

- ten logarithmically equally spaced points between 10^{-6} and 10^{-2} m/s^2 for $a_{\max}$;
- ten linearly equally spaced points between 0.01 and 1.96 orbits before TCA for $\Delta\theta$;
- $\rho = 10^{-11}$ and $\rho = 10^{-9}$.

The maximum number of iterations for the algorithm convergence has been set to 400. For each $a_{\max}$, and at each $\Delta\theta$ the percentage of convergence successes considering $\rho = 10^{-11}$, hence a sharp bang-bang profile, is reported in Table 5.1. Only for convergent cases, the maximum number of iterations required to reach convergence is reported in Figure 5.7.
Setting $\rho = 10^{-9}$ the acceleration profile is much more smooth and tends to the unbounded solution (see Figure 4.18). For this case, the percentage of convergent cases and the maximum number of iterations needed are respectively shown in Table 5.2 and Figure 5.8.

Table 5.1: Convergence percentage rate of bang-bang algorithm with smoothing coefficient $\rho = 10^{-11}$.

$\Delta\boldsymbol{\theta}$ [orbits] \ $a_{\max}$ $[m/s^2]$	1e-06	2.78e-06	7.74e-06	2.15e-05	5.99e-05	1.67e-04	4.64e-04	1.29e-03	3.59e-03	1e-02
0.0100	0	0	0	0	0	0	0	0	0	2
0.2267	0	0	0	4	29	71	73	47	37	16
0.4433	0	0	14	59	78	68	46	35	19	14
0.6600	0	5	35	81	68	47	41	20	10	3
0.8767	0	14	58	68	55	30	22	9	2	1
1.0933	0	15	58	63	29	28	16	3	1	0
1.3100	0	17	58	52	38	31	19	4	3	1
1.5267	2	19	68	56	32	27	19	10	4	3
1.7433	4	28	86	77	55	57	50	27	1	0
1.9600	5	29	84	76	53	44	34	10	4	1

Table 5.2: Convergence percentage rate of bang-bang algorithm with smoothing coefficient $\rho = 10^{-9}$.

$\Delta\theta$ [orbits] \ a_{max} $[m/s^2]$	1e-06	2.78e-06	7.74e-06	2.15e-05	5.99e-05	1.67e-04	4.64e-04	1.29e-03	3.59e-03	1e-02
0.0100	0	0	0	0	0	0	0	0	0	0
0.2267	0	0	0	0	5	23	60	81	76	66
0.4433	0	0	4	22	62	90	93	87	84	72
0.6600	0	3	19	61	90	100	98	94	93	87
0.8767	0	5	26	64	92	100	98	97	94	91
1.0933	0	6	26	65	92	100	100	89	94	96
1.3100	0	10	28	67	92	100	95	96	95	94
1.5267	2	17	56	87	100	99	97	92	82	70
1.7433	4	21	63	91	100	100	100	95	89	58
1.9600	5	24	64	92	100	100	98	92	84	64

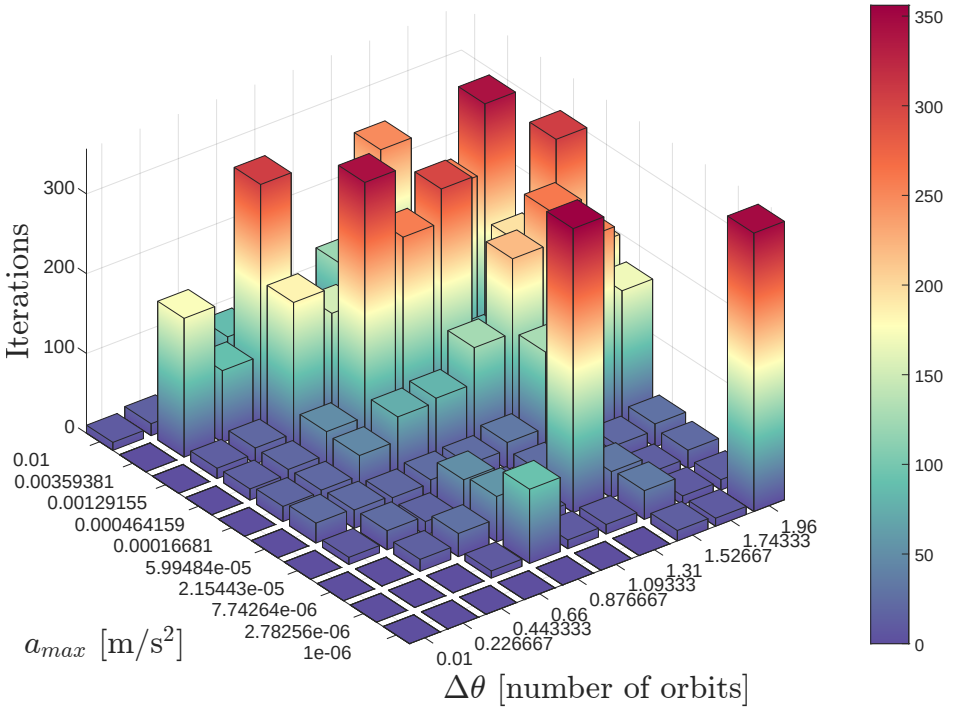

Figure 5.7: Number of iterations for convergent cases with smoothing coefficient $\rho = 10^{-11}$.

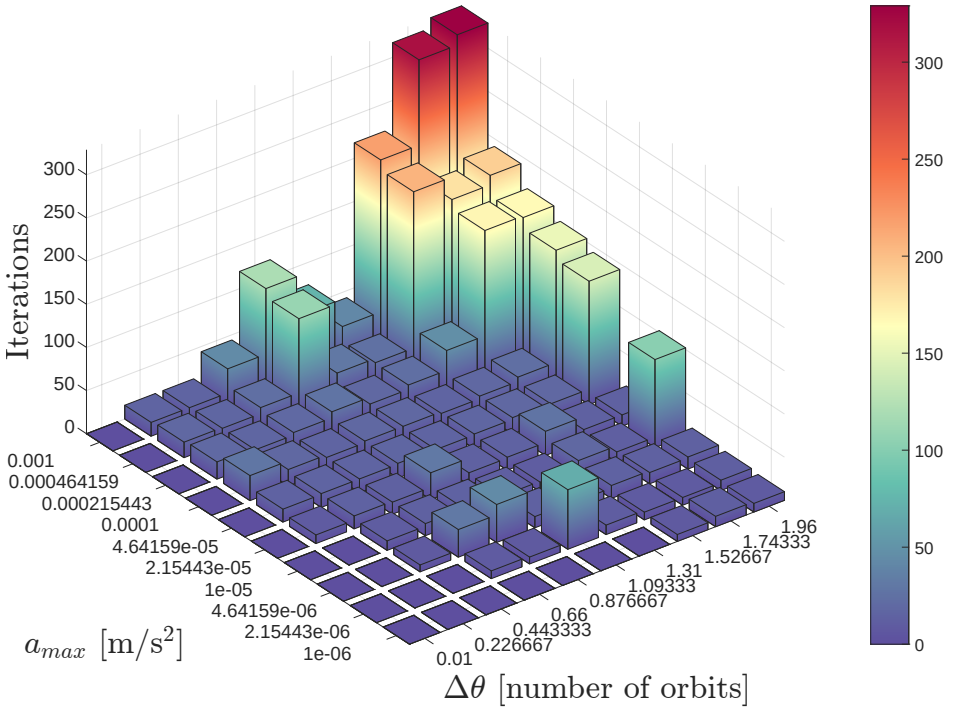

Figure 5.8: Number of iterations for convergent cases with smoothing coefficient $\rho = 10^{-9}$.

Table 5.3: $\Delta\theta$ limit below which the bang-bang solution does not converge (numeric) and minimum $\Delta\theta$ for low-thrust CAM, computed analytically by comparing the burning time and the time to collision (analytic). Smoothing coefficient $\rho = 10^{-11}$.

$a_{\max}$ $[m/s^2]$	Numeric $\Delta\theta_{\min}$ [orbits]	Analytic $\Delta\theta_{\min}$ [orbits]
1.00e-06	1.31	0.23
2.78e-06	0.44	0.23
7.74e-06	0.23	0.01
2.15e-05	0.23	0.01
5.99e-05	0.01	0.01
1.67e-04	0.01	0.01
4.64e-04	0.01	0.01
1.29e-03	0.01	0.01
3.49e-03	0.01	0.01
1.00e-02	0.01	0.01

It can be noticed that with $\rho = 10^{-9}$ the convergence is achieved much easier, both in terms of percentage of success cases and of number of iterations considering only the convergent cases. It is also interesting to observe that, considering a low-thrust manoeuvre starting just 0.01 orbits before the expected collision, the algorithm is never converging, neither for $\rho = 10^{-11}$ nor for a smoothed profile. This is a consequence of the fact that, given a certain $a_{\max}$ affordable for the thrusters, the bang-bang solution would not converge below a certain $\Delta\theta$ limit: the problem cannot be solved with low-thrust propulsion, since the satellite would be so close to the expected impact that even thrusting at the maximum possible thrust continuously for the whole time to collision, the constraints would not be satisfied.

It is also possible to relate $\Delta\theta_{\min}$ to the equivalent total impulse Δv_{tot} calculated analytically: for each $\Delta\theta$, Δv_{tot} is computed by integrating the continuous acceleration profile.

$$\Delta v_{\text{tot}} = \int_{t_0}^{t_{CA}} \mathbf{a}_c \mathrm{d}t. \tag{5.1}$$

Supposing to thrust until the conjunction with a certain $a_{\max}$, the resulting burning time t_b necessary to reach Δv_{tot} is computed as:

$$t_b = \frac{\Delta v_{\text{tot}}}{a_{\max}}. \tag{5.2}$$

If the burning time t_b is higher than the time to collision t_{CA}, the algorithm is expected to fail: the convergence could be reached until $t_b \leq t_{CA}$.
The test case presented in Section 3.3 has been considered for this analysis and the minimum $\Delta\theta$ for each value of $a_{\max}$ is reported in Table 5.3, both considering the numeric convergence of the bang-bang transformation algorithm and the analytic results derived by comparing the burning time and the time to collision.
Even though the two values for $\Delta\theta_{\min}$ do not always match, they are close and it is confirmed that in both cases the minimum $\Delta\theta$ decreases as $a_{\max}$ increases. Please notice that 0.01 is the minimum value considered for $\Delta\theta$.

5.4 Orbital perturbations effect

In order to test the accuracy of the EOP methods presented in Section 4.1, a numerical propagation of the non-linear equations of motion is performed, using a more accurate dynamical model including environmental perturbations.
The same test case considered in Chapter 3 and Chapter 4 is adopted for the validation. Due to the fact that the collision occurs in LEO, the manoeuvre is validated accounting for the following orbital disturbances:

- aerodynamic drag, setting the coefficient $c_D = 2.2$ and considering an average value of area-to-mass ratio equal to 0.3;
- Earth's gravitational harmonics, accounting for the first 10 harmonics.

The algorithm presented in Section 4.1 is validated adjoining the perturbed dynamics: the problem in Eq. 4.14 is solved with the analytical solution, hence the control profile is retrieved with restricted two-body problem dynamics and then it is applied and validated with a propagation using the more complete model.
The final position reached after the propagation, for each initial point of the manoeuvre with $\Delta\theta \in [0,\ 4\pi]$, is reported in BP r.f. in Figure 5.9. The results are almost indistinguishable from the ones reached exploiting the two-body problem dynamics (see Figure 4.2).
The two solutions with Keplerian and perturbed dynamics are shown together on the same enlarged area of the B-plane in Figure 5.10 and a better understanding can be achieved from the comparison of the trends of the final collision probability.

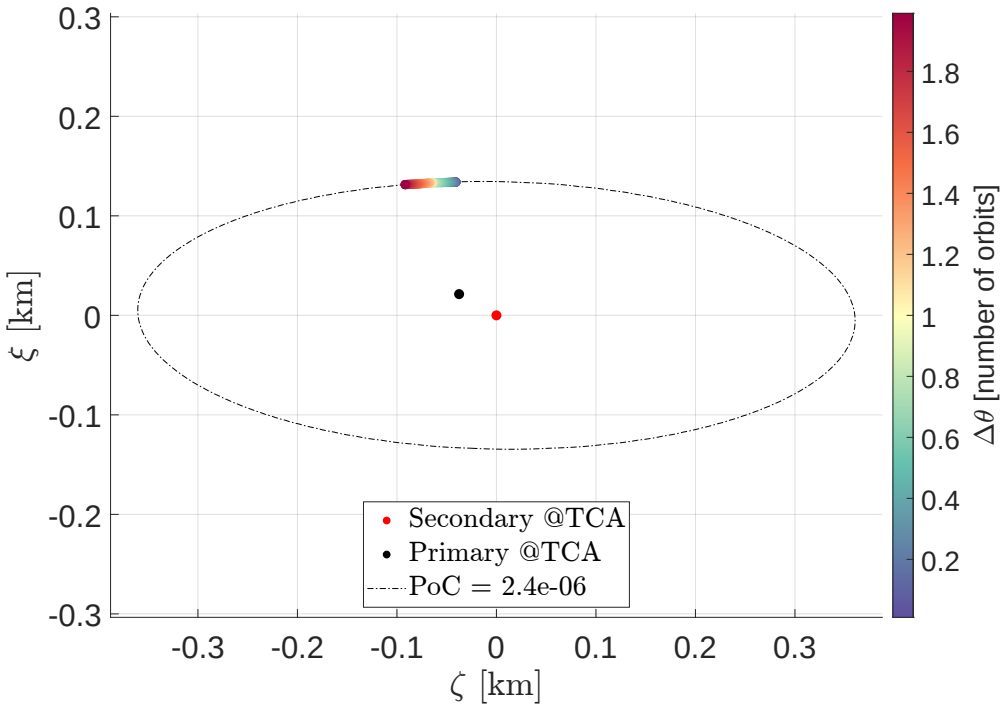

Figure 5.9: Final position in B-plane r.f. reached after the optimal manoeuvre propagated with high fidelity model accounting for environmental perturbations; EOP in ECI coordinates with constrained SMD.

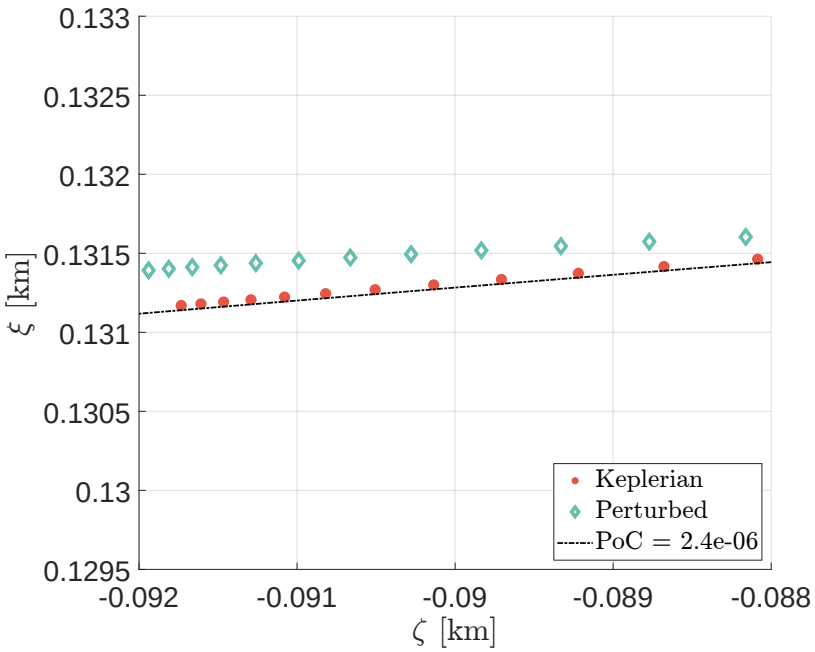

Figure 5.10: Final position in B-plane r.f. reached after the optimal manoeuvre: comparison between Keplerian and perturbed dynamic model; EOP in ECI coordinates with constrained SMD. (Detail of Figure 4.2 and Figure 5.9).

Figure 5.11 shows the differences between Keplerian and perturbed dynamics in terms of final collision probability profile for each true anomaly of the initial manoeuvre point, calculated with the actual final position $\mathbf{r}_f$ obtained after the integration of the respective dynamics.
Predictably, accounting for perturbations, the final collision probability deviates more from the enforced value with respect to Keplerian dynamics propagation, model in which the control is built. Nevertheless, the maximum deviation with disturbances is $1.0531 \cdot 10^{-7}$, a value that, compared to the two-body model error $1.1729 \cdot 10^{-8}$, is acceptable and still one order of magnitude lower than the threshold.

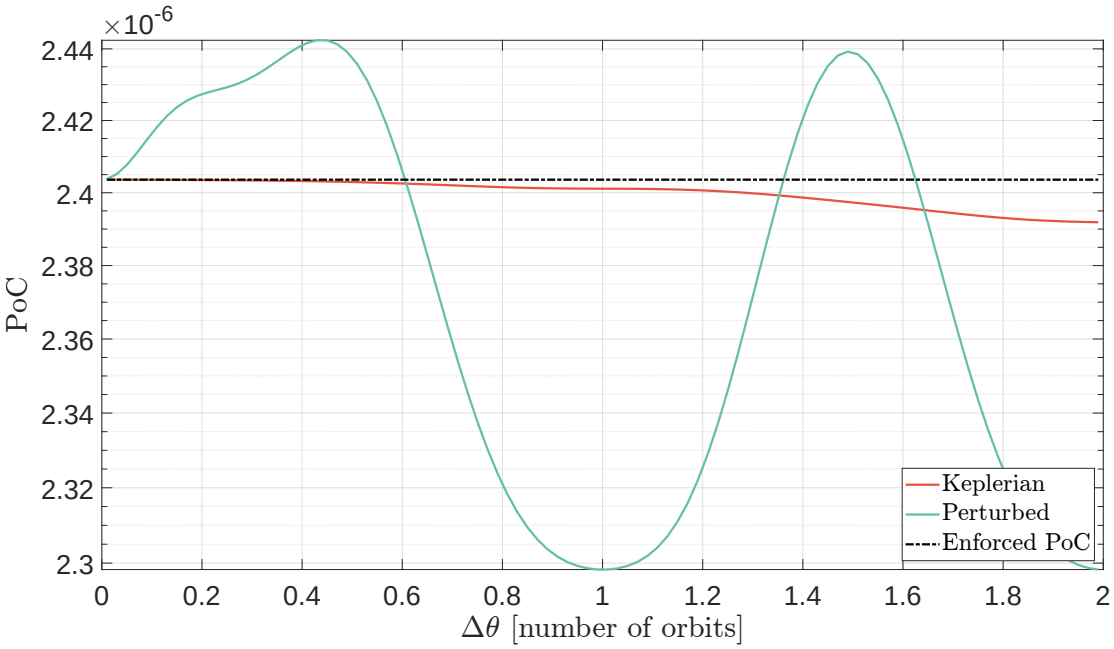

Figure 5.11: Collision probability development after the dynamics propagation: comparison between Keplerian and perturbed dynamic model, EOP in ECI coordinates with constrained SMD.

In conclusion, the variations introduced by atmospheric disturbances are minimal, thus they can be considered negligible for the optimal control problem presented, which turns out to be valid and accurate with the simple Keplerian orbit model.

5.5 Computational time

In this section, the approaches described in Chapter 3 and Chapter 4 are compared in terms of Computational Time (CT). The algorithms have been run on MATLAB® 2020a. Because the CT of the methods is of the order of fractions of second, in order to have results independent of the specific simulation conditions, every simulation is performed over 100 different collisions from ESA Challenge database and then averaged.
The computational time is plotted in Figure 5.12 CT for impulsive manoeuvre, both optimal and purely tangent, considering final constraint in terms of SMD (or PoC) and MD. Considering the different kind of constraints, the four categories of manoeuvre are represented with different colours:

- Optimal manoeuvre with squared Mahalanobis distance final constraint translated into the corresponding Probability of Collision value (Optimal-PoC)
- Optimal manoeuvre with constrained miss distance (Optimal-MD)
- Tangential manoeuvre with squared Mahalanobis distance/Probability of Collision constraint (Tangential-PoC)
- Tangential manoeuvre with constrained miss distance (Tangential-MD)

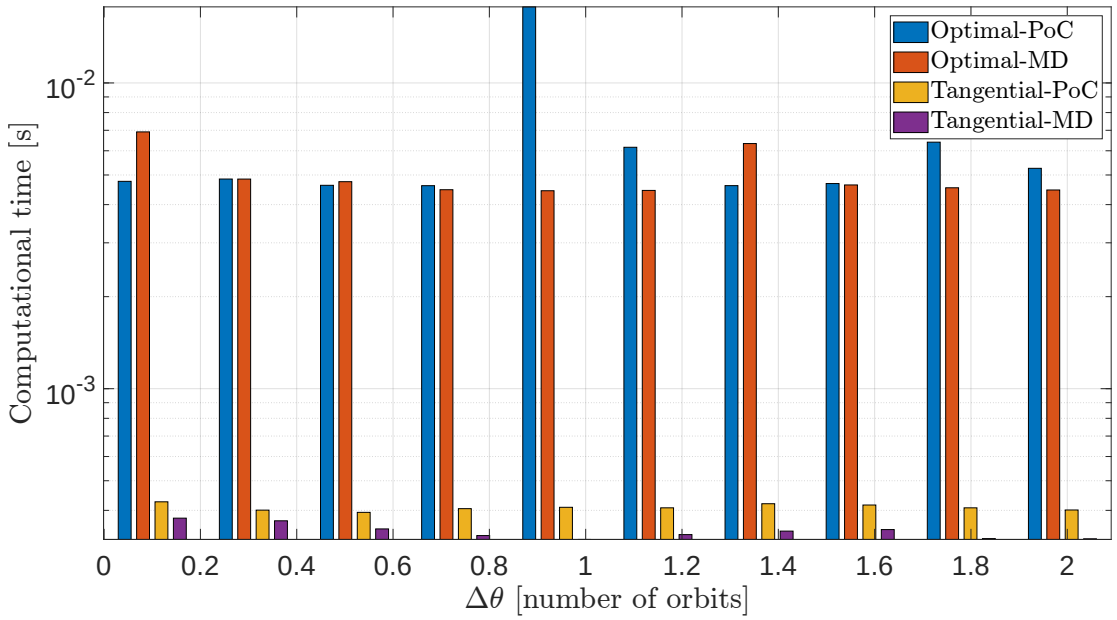

Figure 5.12: Computational time of optimal impulsive CAM methods.

As it can be expected, the manoeuvre with directional constraint is computationally more efficient than the unconstrained one, and the formulation in terms of miss distance in the majority of cases is slightly faster in both cases with respect to constrained collision probability. The trend of the computational time does not depend on the true anomaly of the manoeuvre point: since the CAM is impulsive, it is not affected by the longer orbital propagation times, required instead for low-thrust manoeuvres.

Figure 5.13 shows the comparison between EOP for low-thrust CAMs solved exploiting ECI or BP dynamics, with the two different types of constraint quantity, PoC or MD. Consistently with the reduced dimension of the optimal control problem (OCP in B-plane coordinates has dimension two instead of six), the method with BP coordinates tends to be faster than the algorithm with ECI dynamics.

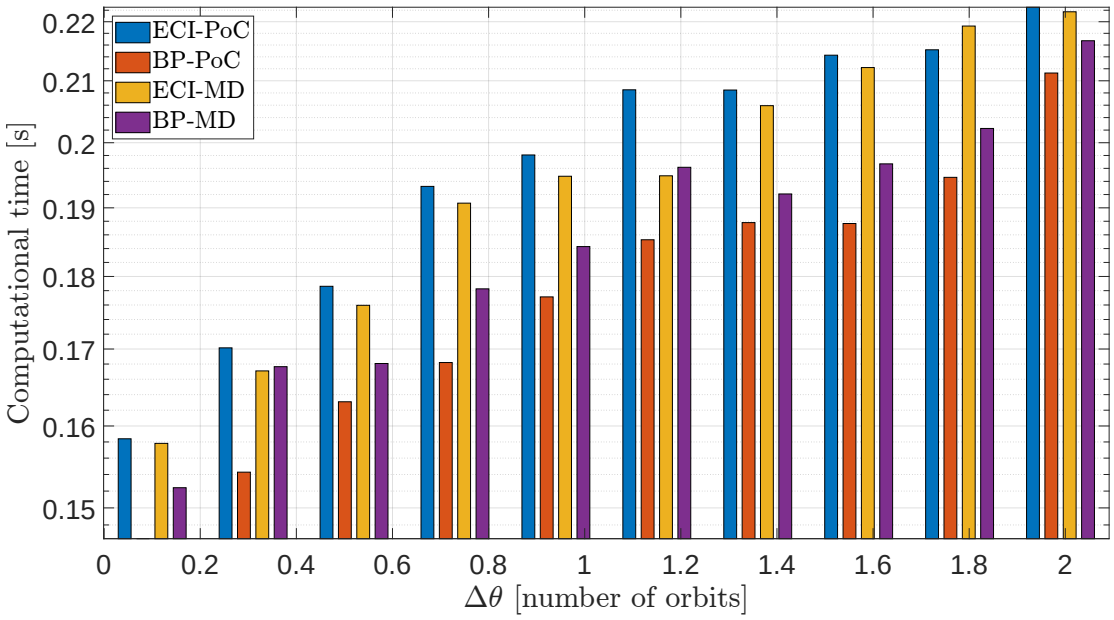

Figure 5.13: Computational time of optimal low-thrust CAM methods.

It can be noticed that the computational times obtained with MATLAB® are in the order of magnitude of $10^{-3}/10^{-4}$ seconds for impulsive manoeuvre and 10^{-1} seconds for low-thrust CAM: they promise good performances if implemented on-board.

CHAPTER 6

Conclusions and further developments

The results of the present work are summarised in this chapter and some recommendations for future research in this field are drawn.

6.1 Methods and comparisons

The main contribution of this thesis is the development of several approaches to design optimal collision avoidance manoeuvres, both for impulsive and low-thrust propulsion, adaptable to the different operational requirements of the satellites. The main conclusions are listed hereafter.

- Several impulsive and continuous-thrust manoeuvre designs have been proposed and validated, considering both constraints in terms of final Miss Distance and final Squared Mahalanobis Distance or Probability of Collision.

- The Energy-Optimal control Problem formulation projected into B-plane has been found to be accurate and computationally more efficient than the algorithm in Cartesian coordinates, consistently with the reduction dimension of the optimal control problem.
- In all cases investigated, the optimal manoeuvres proved to be not too far from purely tangential manoeuvres in direction of the satellite's velocity. In some operating conditions, it may be better to have a purely tangential manoeuvre than to optimise the energy and having radial and out-of-plane components. For this reason, solutions for optimal manoeuvres satisfying the constraint of a tangential thrust have been derived, showing that they are computationally more efficient.
- For continuous-thrust cases a bang-bang profile transformation has been performed and the convergence conditions have been studied, in order to provide other alternatives suitable for operational implementation.
- It has been verified that environmental perturbations in LEO negligibly affect the accuracy of the method, therefore the manoeuvre design using the approximation of Keplerian dynamics seems to be sufficiently accurate.
- Finally, the computational times obtained with MATLAB® promise the feasibility of on-board implementation or massive calculation of CAMs.

6.2 Future work

Few directions for future work are now provided; these could be useful steps in the road map to space-borne implementation of an autonomous collision avoidance system.

- One possible research activity could focus on deriving a more general PoC methodology, in order to account for non-Gaussian uncertainties.
- Further developments in the description of manoeuvre dynamics can be made considering more realistic models than the Keplerian one, for example, a three-body model in order to design CAM in a cislunar environment.
- The best manoeuvre does not depend only on the studied aspects, but also on mission constraints. To account for other requirements, multi-objective

optimisation and further considerations on operational constraints can be set up in future studies.

- In the minimum-energy formulation there is no bound on the mass consumption, therefore a natural improvement could be to add an automatic check-in to the algorithm. If the mass threshold is exceeded, another manoeuvre at higher PoC with adequate mass consumption could be computed.
- The research in the Collision Avoidance Manoeuvre design field will almost certainly benefit from artificial intelligence algorithms. In a supervised machine learning framework, a model could be trained to perform PoC computation and CAM design based on the mean state and covariance of the objects and considering the control capability of the satellites.

Bibliography

[Arm] Roberto Armellin. *Github,* ***https://github.com/arma1978/conjunction/***.

[Arm21] Roberto Armellin. «Collision Avoidance Maneuvers Optimization with a Multi-Impulse Convex Formulation». In: *arXiv preprint arXiv:2101.07403* (2021).

[Bom14a] Claudio Bombardelli. «Analytical formulation of impulsive collision avoidance dynamics». In: *Celestial Mechanics and Dynamical Astronomy* 118.2 (2014), pp. 99–114.

[Bom14b] Claudio Bombardelli, Javier Hernando-Ayuso, and Ricardo Garcìa-Pelayo. «Collision avoidance maneuver optimization». In: *Advances in the Astronautical Sciences* 152.7402 (2014), pp. 1857–1870.

[Bom15] Claudio Bombardelli and Javier Hernando-Ayuso. «Optimal impulsive collision avoidance in low earth orbit». In: *Journal of Guidance, Control, and Dynamics* 38.2 (2015), pp. 217–225. DOI: 10.2514/1.G000742.

[Bry75] Arthur Earl Bryson. *Applied optimal control: optimization, estimation and control*. CRC Press, 1975, pp. 47–55.

[Cha08] F Kenneth Chan et al. *Spacecraft collision probability*. Aerospace Press El Segundo, CA, 2008.

[ESAa] ESA. *ESA Website,* ***https://www.esa.int/***.

[ESAb] ESA. *Safety & Security, Automating collision avoidance* *https://www.esa.int/Safety_Security/Space_Debris/Automating_collision_avoidance*.

[ESAc] ESA. *Safety & Security, Space Debris* *https://www.esa.int/Safety_Security/Space_Debris/*.

[ESAd] Kelvins - ESA. *Collision Avoidance Challenge,* *https://kelvins.esa.int/collision-avoidance-challenge/data/*.

[ESA20] Space Debris Office ESA. «ESA's Annual Space Environment Report». In: (2020).

[Flo17] Tim Flohrer and Holger Krag. «Space surveillance and tracking in ESA's SSA programme». In: *Proceedings 7th European Conference on Space Debris, Darmstadt, Germany, https://conference. sdo. esoc. esa. int*. 2017.

[Gon19] JL Gonzalo Gomez, C Colombo, and P Di Lizia. «A semi-analytical approach to low-thrust collision avoidance manoeuvre design». In: *70th International Astronautical Congress (IAC 2019)*. 2019, pp. 1–9.

[Her21] Javier Hernando-Ayuso and Claudio Bombardelli. «Low-Thrust Collision Avoidance in Circular Orbits». In: *Journal of Guidance, Control, and Dynamics* (2021), pp. 1–13.

[Mar21] Álvaro Martínez Chamarro, Carlos Belmonte Hernandez, and Roberto Armellin. «Design of Collision Avoidance Maneuvers using Optimal Control Theory and Convex Optimization». In: *31st Space Flight Mechanics Meeting* (2021).

[Mer17] K Merz et al. «Current collision avoidance service by esa's space debris office». In: *7th European Conference on Space Debris, Darmstadt, Germany*. 2017, pp. 18–21.

[Mon19] Marco Felice Montaruli. «Collision risk assessment and collision avoidance maneuver planning». MA thesis. Italy: School of industrial, information engineering, Department of aerospace science, and technology, Politecnico di Milano, 2019.

[Mor14] Alessandro Morselli et al. «Collision avoidance maneuver design based on multi-objective optimization». In: *Advances in the Astronautical Sciences* 152.4 (2014), pp. 1819–1838.

[NAS] NASA. *NASA Website,* *https://www.nasa.gov/*.

[Pel07] Jesùs Pelàez, Josè Manuel Hedo, and Pedro Rodrìguez de Andrès. «A special perturbation method in orbital dynamics». In: *Celestial Mechanics and Dynamical Astronomy* 97.2 (2007), pp. 131–150.

[Pel20] R Peldszus and P Faucher. «European Union Space Surveillance & Tracking (EU SST)–State of Play and Perspectives». In: *71st International Astronautical Congress, Session E*. Vol. 3. 2020.

[Ras16] Mirco Rasotto, Roberto Armellin, and Pierluigi Di Lizia. «Multi-step optimization strategy for fuel-optimal orbital transfer of low-thrust spacecraft». In: *Engineering Optimization* 48.3 (2016), pp. 519–542.

[Rei18] Jason A Reiter and David B Spencer. «Solutions to rapid collision-avoidance maneuvers constrained by mission performance requirements». In: *Journal of Spacecraft and Rockets* 55.4 (2018), pp. 1040–1048.

[Sal20] Giuseppina Salemme, Pierluigi Di Lizia, and Roberto Armellin. «Continuous-thrust collision avoidance manoeuvres optimization». In: *AIAA Scitech 2020 Forum*. 2020. DOI: 10.2514/6.2020-0231.

[Sch20] Anna Schiavo. «Numerically efficient design of low-thrust collision avoidance manoeuvre». MA thesis. Italy: School of industrial, information engineering, Department of aerospace science, and technology, Politecnico di Milano, 2020.

[Spa13] Consultative Committee for Space Data System. «Conjunction Data Message». In: CCSDS 508.0-B-1, Blue Book (2013).

[Tah18] Ehsan Taheri and John L Junkins. «Generic smoothing for optimal bang-off-bang spacecraft maneuvers». In: *Journal of Guidance, Control, and Dynamics* 41.11 (2018), pp. 2470–2475.

[Uri20] Thomas Uriot et al. «Spacecraft Collision Avoidance Challenge: design and results of a machine learning competition». In: *arXiv preprint arXiv:2008.03069* (2020).

[Val03] Giovanni B Valsecchi et al. «Resonant returns to close approaches: Analytical theory». In: *Astronomy & Astrophysics* 408.3 (2003), pp. 1179–1196.

[Yam02] Koji Yamanaka and Finn Ankersen. «New state transition matrix for relative motion on an arbitrary elliptical orbit». In: *Journal of guidance, control, and dynamics* 25.1 (2002), pp. 60–66.

Colophon

This thesis was typeset with LaTeX and BibTeX, modifying a typographical look-and-feel created by Vincenzo Pesce and kindly provided to the author. The style was inspired by D.A. Dei Tos `PhD_Dis` and by J. Stevens, L. Fossati `phdthesis` styles.